Graduate School Form 30
(Updated 11/20/2014)

PURDUE UNIVERSITY
GRADUATE SCHOOL
Thesis/Dissertation Acceptance

This is to certify that the thesis/dissertation prepared

By Jamal Alsawalhi

Entitled
An Asymmetric Salient Permanent Magnet Synchronous Machine for Wide Constant Power Speed Range Applications

For the degree of Doctor of Philosophy

Is approved by the final examining committee:

SCOTT D. SUDHOFF

JOHN A. NYENHUIS

OLEG WASYNCZUK

STEVEN D. PEKAREK

To the best of my knowledge and as understood by the student in the Thesis/Dissertation Agreement, Publication Delay, and Certification/Disclaimer (Graduate School Form 32), this thesis/dissertation adheres to the provisions of Purdue University's "Policy on Integrity in Research" and the use of copyrighted material.

SCOTT D. SUDHOFF

Approved by Major Professor(s): _____

_____

Approved by: Michael R. Melloch 11/25/2014

Head of the Department Graduate Program Date

AN ASYMMETRIC SALIENT PERMANENT MAGNET SYNCHRONOUS MACHINE FOR WIDE CONSTANT POWER SPEED RANGE APPLICATIONS

A Dissertation

Submitted to the Faculty

of

Purdue University

by

Jamal Yousuf Alsawalhi

In Partial Fulfillment of the

Requirements for the Degree

of

Doctor of Philosophy

December 2014

Purdue University

West Lafayette, Indiana

This thesis is dedicated to my family, wife, country and my son, Nasser, who, thanks to God, started his journey on Wednesday the 26, 2014. During my PhD years, a lot of good innocent souls were lost in the Arabic world. I dedictace this thesis to their families.

ACKNOWLEDGMENTS

It is impossible to acknowledge everyone that has helped me accomplish this work. I owe a lot to many amazing colleagues and friends at Purdue University in West Lafayette, IN. Thank you all from deepest of my heart.

Howver, i would like to make specefic acknowledgments. First and foremost, all thanks to God, for his blessings and for guiding me to this achievement. Second, big thanks to my PhD advisors, Professors Scott Sudhoff, Steve Pekarek, Oleg Wasynczuk, and John Nyenhuis. Professor Scott Sudhoff, my main PhD advisor, was the biggest motivator and guide to me. I started doing research with him in 2009, and I learned a lot since then. Words cannot express my sincere gratitude to him for what I gained from this fruitful experience.

Although I left my family in 2005, I was fortunate to live amongst my second family. These are the owners of the Mediterranean restaurant Blue Nile, in West Lafayette, IN. I owe them so much and would never be able to thank them as deserved.

I would like to thank my sponsors, the Abu Dhabi National Oil Company, ADNOC. In particular, I thank the staff of ADNOC scholarship office, Mr. Rashed Al Zahmi, the former president of the office, and Mr. Faisal Al Ali, the current president, for supporting me for almost 10 years during my undergraduate and graduate studies.

I owe a lot to my country, the United Arab Emirates (UAE) and to my government, who encouraged education and created various scholarships to fund students like me to study abroad. I will work hard to pay back some of what I owe to my country using the knowledge I collected from Purdue university.

Finally, thanks to my family and wife, who stood by me in the good and bad moments and were always supportive and encouraging. Thank you all.

TABLE OF CONTENTS

Page

LIST OF TABLES

Table Page

LIST OF FIGURES

Figure Page

Figure Page

ABSTRACT

Alsawalhi, Jamal, Ph.D., Purdue University, December 2014. An Asymmetric Salient Permanent Magnet Synchronous Machine for Wide Constant Power Speed Range Applications. Major Professor: Scott Sudhoff.

This work introduces a novel permanent-magnet synchronous machine (PMSM) architecture that employs rotational asymmetry to increase the torque density output in constant power variable speed applications. A population based multi-objective design optimization algorithm is used to design and analyze the new machine topology. A number of design studies are presented to show that the proposed machine structure outperforms a conventional PMSM machine. Validation of the analytical machine design model using a three dimensional finite element analyses is performed and the results are presented. Finally, a case study in which a hybrid electric bus traction motor is designed is presented.

1. INTRODUCTION

This work focuses on enhancing the torque density of Permanent Magnet Synchronous Machines (PMSMs) in constant power speed range (CPSR) applications. A novel PMSM rotor structure is proposed to serve the stated goals. This stator utilizes a traditional distributed winding configuration. The new machine is referred to as an Asymmetrical Salient Permanent Magnet Synchronous Machine (AS-PMSM). The AS-PMSM is equipped with a rotationally asymmetric rotor as depicted in Fig 1.1, where a sample 4-pole surface mounted permanent magnet rotor is shown. Labeled therein is the rotor backiron, permanent magnets and rotor teeth. Rotor teeth are asymmetrically positioned in each magnetic pole, thus creating an asymmetrical saliency. More discussion on this topology will be presented in Chapter 3.

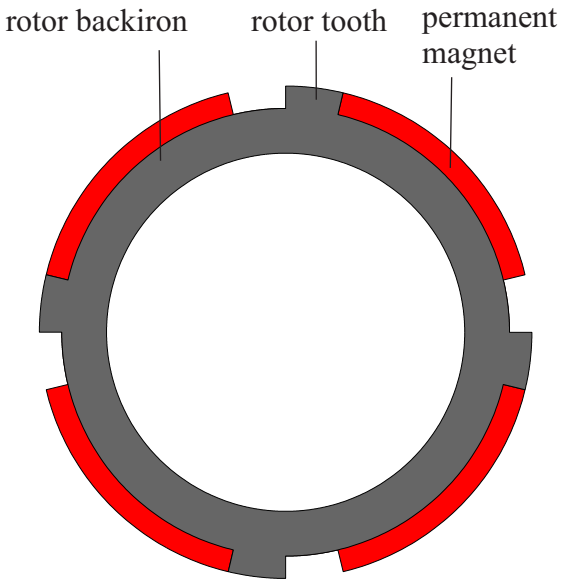

Fig. 1.1. Rotor lamination of a sample AS-PMSM 4 pole rotor

The electromagnetic performance of the AS-PMSM is analyzed using a rigorous population based multi-objective optimization procedure. It is shown that the AS-PMSM configuration yields a more favorable tradeoff between power loss and machine cost (or

mass) than the conventional Surface Mounted Permanent Magnet Synchronous Machine (SM-PMSM) in wide CPSR applications.

The first section in this chapter, Section 1.1, reviews relevant work and research that has been done to improve the torque density and CPSR of PMSMs. Then in Section 1.2, the organization of the preliminary thesis is presented.

1.1 Literature Review

PMSMs have historically been used in specialty applications of small ratings or in very high speed applications, in excess of 20,000 rpm [1]. Examples include spindle drives and flywheel energy storage machines. Advancements in the late 20^{th} century in high energy permanent magnets increased interest in PMSMs. For example, [2] showed that the utilization of PMSMs in full and hybrid electric vehicles drastically increased in the last six years, where it accounted for 65% of electric machines topologies used. Reasons for this increase are some drawbacks that other machine topologies suffer from. Direct Current (DC) machines, although capable of providing high stall torque, suffers from degradation of carbon brushes, which creates a maintenance issue. Induction machines exhibits the advantage of low cost and high robustness but need sophisticated control to accommodate wide speed operation [3]. Reluctance machines suffer from low efficiency and relatively low power density [4]. PMSM machines are typically known for their high torque density for a given loss, high reliability, and high system efficiency. However, there are some drawbacks of this machine which includes rising rare-earth permanent magnets cost, machine assembly cost, and susceptibility of permanent magnet demagnetization under fault conditions.

PMSM machines can in general be classified as Surface Mounted Permanent Magnet Synchronous Machines (SM-PMSM), Fig.1.2, or Interior Permanent Magnet Synchronous Machines (IPMSM), Fig 1.3, with a variety of different structures emerging from these general classes. The SM-PMSM have permanent magnets placed on the surface of the rotor, which are secured in position by glue or an inert material band. In IPMSM, the permanent magnets are buried in the rotor backiron. This provides mechanical protection to the permanent magnets.

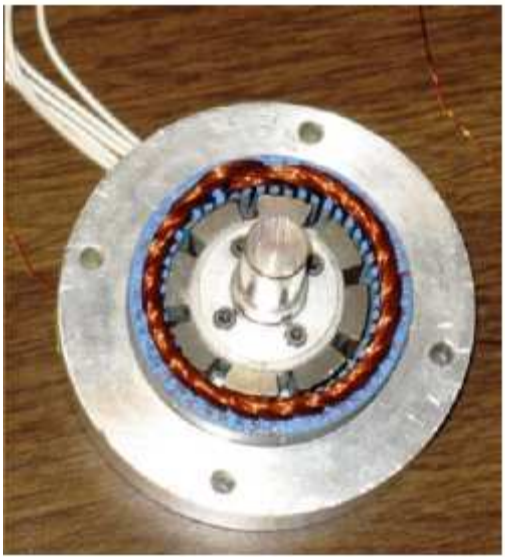

Fig. 1.2. A sample SM-PMSM [19]

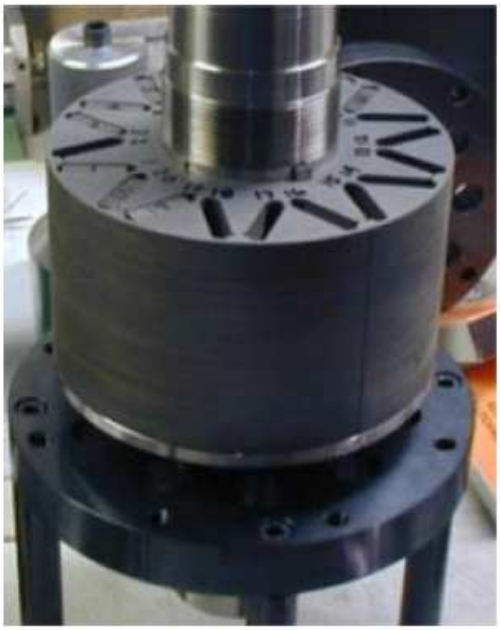

Fig. 1.3. Rotor of an IPMSM used in [30]

In traction applications, one of the main requirements for an electric motor is to have the capability of maintaining a wide CPSR. For instance, consider Fig. 1.4, were an ideal torque versus speed capability curve of a PMSM motor is shown. The PMSM is assumed to be connected to a dc power supply and a three phase inverter to permit variable-speed drive operation. Superimposed is the corresponding power versus speed curve, shown in red. Two regions can be identified in the figure; a constant torque region and a constant power region. It is common in literature to refer to the constant power region as the flux weakening region, where the term is adopted from "field weakening" applied in machines that include field windings around the rotor. The CPSR ratio is defined as the ratio of the maximum constant power speed over rated speed.

Typically in constant torque region, the current phase angle is optimized to implement a maximum torque per amp control. This control is abandoned upon transitioning from constant torque region into flux weakening region (constant power region). This transition occurs when the voltage limit associated with the dc power supply supplying the PMSM is reached. To reduce the machine voltage below the maximum limit, permanent magnet flux weakening is applied, most often by injecting a negative *d*-axis current. Doing so, however, reduces the machine's output torque due to the reduction in *q*-axis current which must be reduced in order to avoid violating the machines current limits. The reduction in torque continues until the voltage limit can no longer be maintained without reducing the rms-current below rated current. This point defines the maximum speed the system is rated for.

Research to enhance the CPSR performance of PMSM machines can be generalized into two categories: advanced control methods or an improved magnetic design of the machine. In the first category, advanced control strategies were proposed to optimally control the *qd* currents in the flux weakening region. These control methods can be classified into four methods: feed-forward control, feed-back control, hybrid control, and non-linear control theory techniques [5]. Feed-forward control methods [6,7] are generally known for their good stability and transient responses. They are strongly dependent on machine parameters (lumped circuit model parameters). Hence, any variation in temperature or magnetic saturation effects can deteriorate the controller response. Feed-back control techniques [8]-[10] on the other hand are robust to the variation of motor parameters. One issue with the feed-back control is its performance in transient operation. Hybrid control strategies [11,12] aim to combine the advantages of feed-forward and feed-back control. Usually they require look-up tables, which require extensive experimental data collection. Finally, non-linear control theory [13,14]

combines speed and current controllers. The machine and controller parameters are updated in real time. This method is therefore robust to variations in motor parameters. Yet, it is considered as the most computationally complex method compared to the previous three control methods.

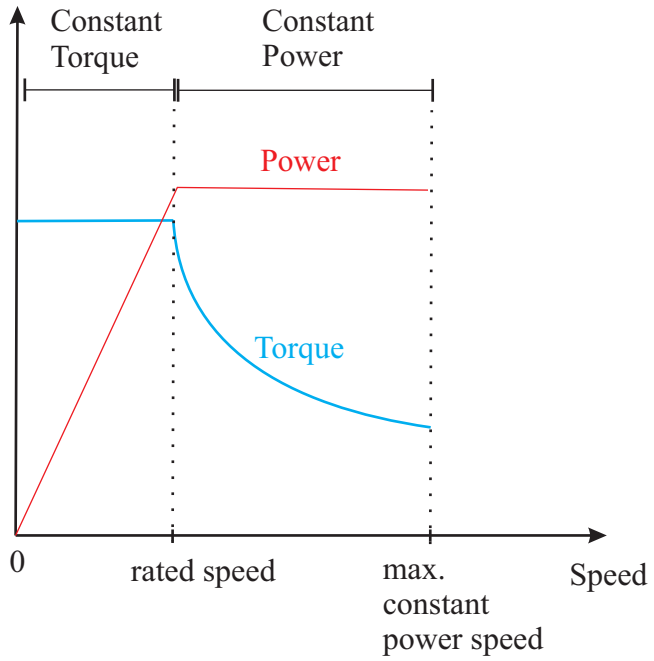

Fig. 1.4. Ideal torque and power versus speed capabilities of a PMSM

The second research category on enhancing CPSR in PMSM focuses on proper magnetic design of the machine, where the design is modified by either altering the machine's geometrical structure or by applying specific excitation methods. Modifying the machine structure is usually done with the goal of increasing the saliency in the machine, which is the difference between the *d*- and *q*-axes inductances. Adding saliency to the machine structure produces what is commonly known as saliency or reluctance torque, which contributes to the overall torque production in addition to the torque produced by the permanent magnet. Compared to a non-salient machine, a salient machine needs less *q*-axis current to produce the same total torque, which could potentially increase the machine's efficiency.

An interesting study on the power capability of salient pole machines in variable speed drive application was conducted in [15]. A constant parameter equivalent circuit

model that neglects motor losses was used to determine the effects of *qd* inductances and back-emf voltage on the power capability of salient pole permanent magnet motors in variable speed drive applications. It was concluded therein that a tradeoff exist between the maximum torque a machine can output and the maximum speed range over which constant power can be maintained. In theory, if losses are neglected, the maximum speed in constant power speed range could be extended to infinity if the characteristic current, defined as the ratio of the permanent magnet flux linkage and *d*-axis inductance, is equal to the machine rated current. Finally, it was claimed that it is better, in a CPSR sense, to have low rather than high *d*-axis inductance.

Several techniques have been demonstrated to increase saliency in PMSMs. One technique is the use of flux barriers in SM-PMSM and IPMSM to modify the *qd* inductances as shown in Fig. 1.5. This procedure has been reported in [16]-[18]. This was done to maximize the difference between the *q*-axis inductance and the *d*-axis inductance, and thus increase the torque density output by producing saliency torque. An investigation on the effects of saliency on CPSR performance in SM-PMSMs has been conducted in [19]. In particular, an inset SM-PMSM was designed and compared to a regular SM-PMSM with similar design specifications. It was shown that although saliency can increase torque density, it can lead in an increased machine loss profile. It was concluded that no major benefits, towards the design objectives, are obtained by adopting a salient machine structure.

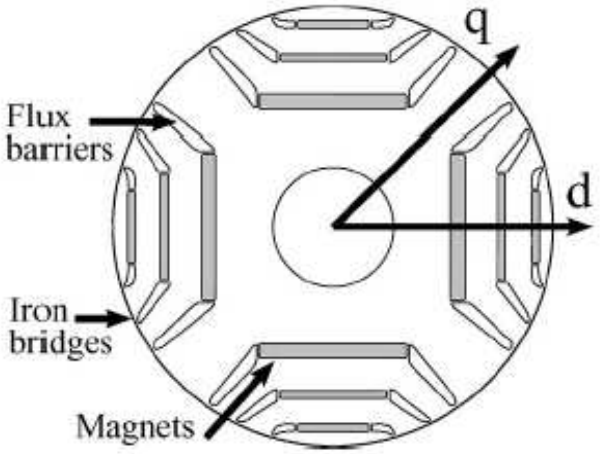

Fig. 1.5. A rotor lamination of a Permanent Magnet Assisted Synchronous Reluctance Motor (PMASR) [18]

In [39], a theoretical analysis of a synchronous machine equipped with a hybrid rotor was conducted. The two part rotor consists of a reluctance part and a surface mounted PM/excitation part both placed on the same shaft. The main purpose of this study was to examine the effects of having a displaced or shifted reluctance rotor relative to the surface mounted PM rotor, as shown in Fig. 1.6. Using a normalized system of equations, and assuming linear, lossless, harmonic-free system, it was shown that for a motor with fixed saliency ratio, the maximum output torque-to-magnet cost ratio is achievable with the displacement angle $\beta = 60^o$. In other words, displacing the reluctance axis with the right amount can reduce the overall cost of the machine.

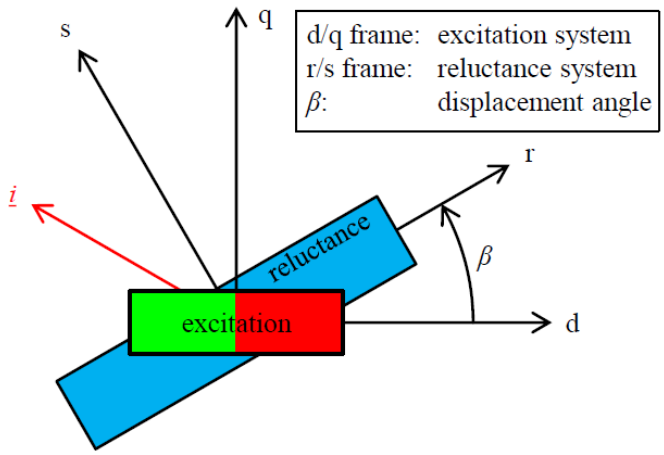

Fig. 1.6. Basic reference frames of two part rotor with the reluctance part displaced relative to the excitation part [39]

Saliency can also be introduced by tapering the machine structure. This has been done to a reluctance machine [4], where it was shown that the torque density improved by tapering the rotor asymmetrically. The torque density produced in the counter clockwise direction was noticeably improved at the expense of torque density in clockwise direction. In [20], a rotationally asymmetric IPMSM was designed for a low-voltage battery-powered electric motorcycle. A sketch of a portion of the rotor is shown in Fig. 1.6. It was demonstrated via simulation and experimental verification that the asymmetrical IPMSM coupled with conduction angle control successfully mitigated torque ripple and achieved a wide CPSR. However, a detailed explanation on the design procedure of the asymmetric rotor was not presented. In addition, the effects of the asymmetric rotor on the other machine properties such as loss were not studied.

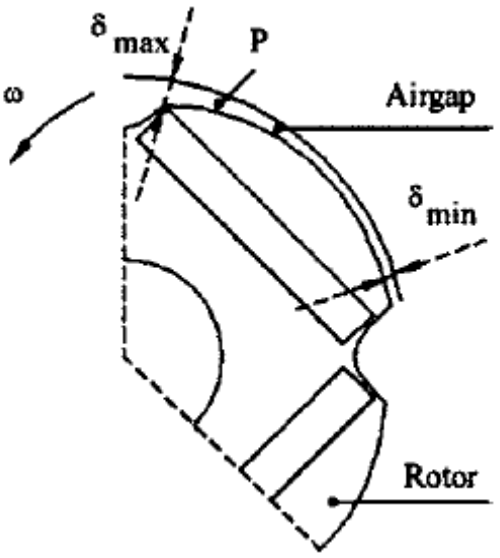

Fig. 1.7. Asymmetric IPMSM [20]

Another tapered air gap machine topology was considered in [21], and a sketch of its cross section is shown in Fig. 1.7. Therein, a self-starting single-phase SM-PMSM with tapered stator teeth was investigated using Finite Element Analysis (FEA). The tapered structure eliminates the need for a starting dead point, which reduces the machines cost. Losses were not considered in that work and are part of the planned future work.

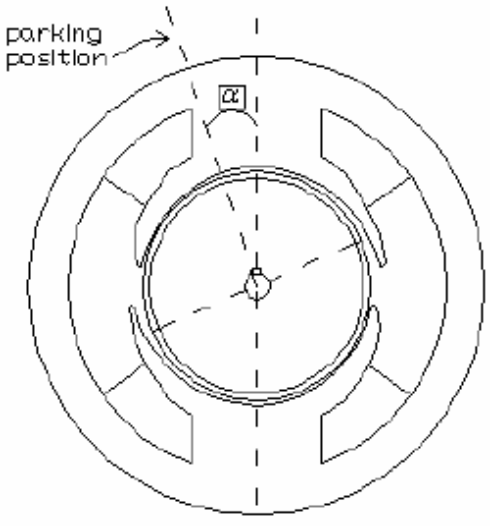

Fig. 1.8. Asymmetric SM-PMSM [21]. Note that the stator teeth are tapered and that the air gap reduces in the counter clockwise direction.

In [22], a rotationally symmetric rotor structure, Fig. 1.8, for an IPMSM was designed for hybrid electric vehicle application. Rotor poles were tapered symmetrically such that the minimum air gap coincides with the *d*-axis while the maximum air gap is at the *q*-axis. This was done to increase saliency such that the ratio of *d*-axis inductance over *q*-axis inductance is greater than 1. FEA results were presented along with loss calculations using analytical models. The proposed machine was compared to a typical IPMSM (which has a ratio of *d*-axis inductance over *q*-axis inductance less than 1) with similar dimensions, materials, winding configuration, rated power and rated torque. The comparison revealed that higher efficiency was obtained at low and high speeds using the proposed machine design. However, it is difficult to truly compare different machine types by comparing point designs, since there are multiple metrics for comparison. In addition, the modification applied here counters the conclusion reached in [15], which favors a low *d*-axis inductance for CPSR applications. Thus, more analysis is needed to determine the effect of this modification on CPSR performance.

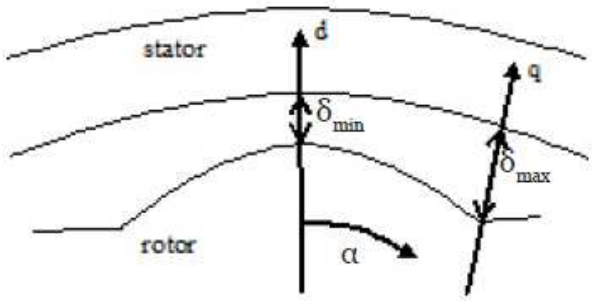

Fig. 1.9. Rotationally symmetric tapered rotor [22]

In non-salient machine topologies, such as SM-PMSMs, [23] suggested using a concentrated, fractional slot winding in the stator windings to increase the low *qd* inductance and ultimately enhance the CPSR performance. A 6 kW fractional-slot concentrated winding SM-PMSM for automotive direct-drive starter/alternator with a CPSR of 10:1 was designed. Experimental validation was later provided in [24], were a CPSR of 5:1 was demonstrated. A close-up view of the machine used for verification is shown in Fig. 1.9. Although test results have convincingly demonstrated machine's ability to deliver wide CPSR operation as well as high machine efficiency, a multi-objective comparison showing the tradeoff in different machine metrics, for example loss versus mass, between SM-PMSM equipped with concentrated winding and a SM-PMSM

equipped with a distributed winding was not presented, which hinders making definite conclusions on the improvements obtained from a concentrated winding. Comparing loss in particular is important in this case because of the rich harmonic content in the air gap flux due to the use of fractional slot concentrated winding.

Fig. 1.10. Close up view of 6kW 36-slot/30-pole fractional-slot concentrated winding SM-PMSM used in [24]

In this work, taking a similar approach to [4], [20], [21] and [22], the CPSR and torque density of PMSMs is elevated by designing an asymmetrical salient rotor, shown in Fig. 1.1. The proposed machine is rotationally asymmetric. However, unlike the previous designs which focused on decreasing torque ripple, the new machine couples saliency and rotational asymmetry to produce higher torque density compared to a conventional SM-PMSM as described in [26]. In addition, the AS-PMSM machine possesses a wide CPSR as will be demonstrated.

The multi-physics properties of electric machines, large design space, and several competing objectives, necessitate a proper multi-objective design treatment in order to obtain reliable conclusions on machine designs. This has been done for the case of an IPMSM [25] and a SM-PMSM in [26], were a multi-objective design with a large design space considered. In [27], a stepwise multiple regression technique have been presented which enables reducing design space dimensions by screening nonessential variables

which are less relevant to performance improvement. A thorough discussion on multi-objective design approach can be found in [28]. A summary of recent developments in electrical machine design optimization methods can be found in [29].

Herein, the AS-PMSM is designed using multi-objective optimization techniques similar to the approach presented in [25] and [26]. The process is formulated to minimize the cost and total losses of the machine. The Pareto-optimal front showing the tradeoff between the competing objectives is presented and used to compare the performance of the AS-PMSM to a nominal SM-PMSM designed under the same design specifications.

1.2 Thesis Organization

The organization of this document is as follows. In Chapter 2, a simplified PMSM design problem is considered. The problem is formulated to provide the motivation for a detailed analysis of the AS-PMSM. In Chapter 3, a detailed analysis of the AS-PMSM is provided. In Chapter 4, design results of an AS-PMSM are presented. The AS-PMSM is compared to a SM-PMSM. The comparison shows that the new machine architecture gives significant improvements in the Pareto-optimal front between loss and cost. In Chapter 5, the AS-PMSM and SM-PMSM analytical designs are validated versus 3-D Finite Element Analysis (FEA) models. The validation process compares the analytical and FEA output torque and machine lumped model parameters. In Chapter 6, a case study is presented in which the AS-PMSM is designed for a heavy hybrid electric vehicle. Lastly, Chapter 7 concludes this thesis and suggests areas for further investigation in future work.

2. AN INITIAL LOOK INTO SALIENT PERMANENT MAGNET MACHINES

This chapter provides motivation for the new machine structure proposed herein and shown in Fig. 1.1. In particular, a simplified single objective optimization design problem of a salient SM-PMSM is studied. In Section 2.1, the design specifications and applications are stated. The design analysis is presented in Section 2.2. Therein, the design space, constraints and objective function are formulated. In Section 2.3, four different design configurations are introduced. These configurations will be suggestive of the advantages gained from the new machine structure. Finally in Section 2.4, design results are presented and discussed. These results will motivate a detailed study of the proposed machine structure in Chapter 3.

2.1 Design Specifications and Applications

A design of a salient SM-PMSM motor is considered herein. The design specifications are listed in Table 2.1. The machine is assumed to be driven from a dc power supply connected to a three phase inverter. The dc power supply voltage is denoted as v_{dc}. The machine stator windings are assumed to be symmetrical with a resistance R_s. Parameters P and $\lambda_{m,mx}$ denote the magnetic poles of the machine and the maximum permanent magnet flux linkage available. The machine inductances will be determined as design variables.

The machine is designed for a CPSR of 5:1. This range is characterized by three operating points. The three operating points mechanical rotor speeds are denoted by vector $\boldsymbol{\omega}_{rm}$ while the target electromagnetic torque at each point is denoted by $\mathbf{T}_e^*$. The constant output power, $\mathbf{P}_{out}$, achieved in this range is 3.7 kW. Weighted machine power loss is calculated using one of the three weighting vectors $\mathbf{w}_1$, $\mathbf{w}_2$ or $\mathbf{w}_3$. The first weighting vector weighs the power loss at each operating point equally while the second and third weighting vectors weigh the power loss towards the lowest speed and highest speed respectively.

TABLE 2.1
Design Specifications

Parameter	Value	Units
v_{dc}	187	V
R_s	0.25	Ω
P	4	N/A
$\lambda_{m,mx}$	0.115	Vs
$\boldsymbol{\omega}_{rm}$	[1000, 2236, 5000]	rpm
$\mathbf{T}_e^*$	[35.6, 15.9, 7.12]	Nm
$\mathbf{P}_{out}$	[3.7, 3.7, 3.7]	kW
$\mathbf{w}_1$	[0.333, 0.334, 0.333]	N/A
$\mathbf{w}_2$	[0.7, 0.2, 0.1]	N/A
$\mathbf{w}_3$	[0.1, 0.2, 0.7]	N/A

The CPSR requires monitoring to the maximum line-to-line voltage the power supply can provide. As the rotor speed increases, the maximum line-to-line voltage increases until it reaches the maximum limit that can be supplied by the dc power supply. A common procedure to address this situation when encountered is to inject negative *d*-axis current to weaken the permanent magnet flux and thus decrease the operating maximum line-line voltage. The drawback of injecting negative *d*-axis current, however, is a decrease in machine efficiency and output power rating. One of the purposes of the investigation conducted in this chapter is to examine what machine properties, in terms of a lumped parameter model, are conducive to obtaining wide CPSR.

2.2 Design Analysis

The design analysis begins by first considering the machine's stator *qd* flux linkage equation. The *qd* flux linkage equation for a PMSM is given as the sum of the flux linkage due to machine's inductance and the flux linkage due to the rotor permanent magnet. This is expressed as

$$\boldsymbol{\lambda}_{qds}^{R} = \boldsymbol{\lambda}_{qdx}^{R} + \boldsymbol{\lambda}_{qdpm}^{R} \tag{2.1}$$

where $\boldsymbol{\lambda}_{qds}^{R}$ is the stator *qd* flux linkage vector, $\boldsymbol{\lambda}_{qdx}^{R}$ is the *qd* flux linkage vector due to the machine inductance while $\boldsymbol{\lambda}_{qdpm}^{R}$ is the *qd* flux linkage vector due to the permanent magnet. The flux linkages are expressed in a frame of reference R that rotates with the rotor. Note that the zero sequence flux linkage is ignored since a wye-connected three phase winding is assumed.

In a typical PMSM, the inductance flux linkage depends on a decoupled *qd* inductance matrix while the permanent magnet flux linkage is centered at the *d*-axis. However, in reference frame R the arrangement shown in Fig. 2.1 is assumed. Therein, the *qd* inductance flux linkages are decoupled, as is the case for a nominal PMSM. However, the permanent magnet flux linkage λ_m projects on both the *q*- and *d*-axes. The angular phase shift between the *d*-axis and the permanent magnet flux linkage in frame of reference R is expressed by angle ϕ_{dm}.

For the setting illustrated in Fig 2.1, (2.1) can be expressed as

$$\begin{bmatrix} \lambda_{qs}^{R} \\ \lambda_{ds}^{R} \end{bmatrix} = \begin{bmatrix} \lambda_{qx}^{R} \\ \lambda_{dx}^{R} \end{bmatrix} + \lambda_m \begin{bmatrix} \sin(\phi_{dm}) \\ \cos(\phi_{dm}) \end{bmatrix} \tag{2.2}$$

which may be expanded to

$$\begin{bmatrix} \lambda_{qs}^{R} \\ \lambda_{ds}^{R} \end{bmatrix} = \begin{bmatrix} L_q & 0 \\ 0 & L_d \end{bmatrix} \begin{bmatrix} i_{qs}^{R} \\ i_{ds}^{R} \end{bmatrix} + \lambda_m \begin{bmatrix} \sin(\phi_{dm}) \\ \cos(\phi_{dm}) \end{bmatrix} \tag{2.3}$$

where, L_q and L_d are the *q*- and *d*-axis inductances and i_{qs}^{R} and i_{ds}^{R} are the *qd* currents in reference frame R.

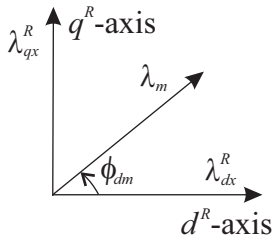

Fig. 2.1. Reluctance and permanent magnet flux linkages in reference frame *R*

It is possible to center the permanent magnet flux linkage on the *d*-axis by applying a frame-to-frame transformation. This transformation transforms the *qd* axes by an angular displacement equal to ϕ_{dm}, as shown in Fig. 2.2. This new frame is denoted by a superscript r. Note that in this new frame, the *qd* reluctance flux linkages, λ_{qx}^{r} and λ_{dx}^{r}, project on both the *q*- and *d*-axes.

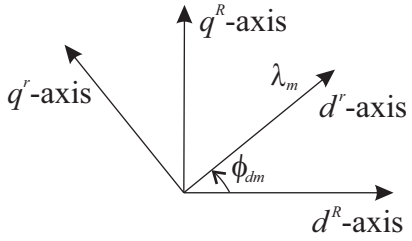

Fig. 2.2. Transformation into frame of reference *r*

The frame-to-frame transformation applied in Fig. 2.2 is given by [28]

$$ {}^{R}K^{r} = \begin{bmatrix} \cos(\phi_{dm}) & -\sin(\phi_{dm}) \\ \sin(\phi_{dm}) & \cos(\phi_{dm}) \end{bmatrix} \tag{2.4} $$

where ${}^{R}K^{r}$ means a transformation from frame of reference R to frame of reference r. Multiplying both sides of (2.3) by ${}^{R}K^{r}$ and using the inverse matrix ${}^{R}K^{r^{-1}}$ to eliminate the *qd* currents in frame of reference R yields

$$ \begin{bmatrix} \lambda_{qs}^{r} \\ \lambda_{ds}^{r} \end{bmatrix} = {}^{R}K^{r} \begin{bmatrix} L_q & 0 \\ 0 & L_d \end{bmatrix} {}^{R}K^{r^{-1}} \begin{bmatrix} i_{qs}^{r} \\ i_{ds}^{r} \end{bmatrix} + \lambda_m \begin{bmatrix} 0 \\ 1 \end{bmatrix} \tag{2.5} $$

Evaluating (2.5) results in

$$ \begin{bmatrix} \lambda_{qs}^{r} \\ \lambda_{ds}^{r} \end{bmatrix} = \begin{bmatrix} L_{qq} & L_{qd} \\ L_{qd} & L_{dd} \end{bmatrix} \begin{bmatrix} i_{qs}^{r} \\ i_{ds}^{r} \end{bmatrix} + \lambda_m \begin{bmatrix} 0 \\ 1 \end{bmatrix} \tag{2.6} $$

where

$$ L_{qq} = L_q \cos^2(\phi_{dm}) + L_d \sin^2(\phi_{dm}) \tag{2.7} $$

$$L_{dd} = L_q \sin^2(\phi_{dm}) + L_d \cos^2(\phi_{dm}) \tag{2.8}$$

$$L_{qd} = (L_q - L_d)\cos(\phi_{dm})\sin(\phi_{dm}) \tag{2.9}$$

In (2.6), the inductance matrix includes non-diagonal inductances that account for the coupling between the *q*- and *d*- axes. Diagonal inductances are a function of the phase shift between the inductance *d*-axis flux linkage , λ_{dx}^r, and the permanent magnet flux linkage, λ_m, which is now centered on the *d*-axis as shown in Fig. 2.2.

The steady state *qd* voltage equations are given by [28]

$$\begin{bmatrix} v_{qs}^r \\ v_{ds}^r \end{bmatrix} = r_s \begin{bmatrix} i_{qs}^r \\ i_{ds}^r \end{bmatrix} + \omega_r \begin{bmatrix} \lambda_{ds}^r \\ -\lambda_{qs}^r \end{bmatrix} \tag{2.10}$$

where ω_r is the electrical rotor speed in radians per second. The relation between ω_r and ω_{rm}, is expressed as

$$\omega_r = \frac{P}{2}\omega_{rm} \tag{2.11}$$

It is important to monitor and limit the peak line-to-line voltage so that the maximum limit achievable by the system is not exceeded. The peak line-to-line voltage is expressed as

$$v_{ll,pk} = \sqrt{3}\sqrt{\left(v_{qs}^r\right)^2 + \left(v_{ds}^r\right)^2} \tag{2.12}$$

Another important metric is the electromagnetic torque produced by the machine can be shown to be equal to

$$T_e = \frac{3}{2}\frac{P}{2}\left(\lambda_{ds}^r i_{qs}^r - \lambda_{qs}^r i_{ds}^r\right) \tag{2.13}$$

Substituting (2.6) into (2.13) and then substituting (2.7)-(2.9) for L_{qq}, L_{dd}, and L_{qd} and rearranging gives

$$T_e = T_{ex} + T_{em} \tag{2.14}$$

where the electromagnetic torque due to machine's asymmetrical inductance is given by

$$\begin{aligned} T_{ex} = & \frac{3}{2}\frac{P}{2} i_{qs}^r i_{ds}^r \left(L_q \left(\sin^2\left(\phi_{dm}\right) - \cos^2\left(\phi_{dm}\right)\right) + L_d \left(\cos^2\left(\phi_{dm}\right) - \sin^2\left(\phi_{dm}\right)\right)\right) \\ & + \frac{3}{2}\frac{P}{2}\left(L_q - L_d\right)\cos\left(\phi_{dm}\right)\sin\left(\phi_{dm}\right)\left(\left(i_{qs}^r\right)^2 - \left(i_{ds}^r\right)^2\right) \end{aligned} \tag{2.15}$$

and the electromagnetic torque due to the permanent magnet is given by

$$T_{em} = \frac{3}{2}\frac{P}{2} i_{qs}^r \lambda_m \tag{2.16}$$

The torque produced in a nominal surface mounted PMSM is mainly from the permanent magnet torque (2.16), since negligible saliency exists.

The only loss component taken into account in this design problem is dc conduction loss. The dc conduction loss is equal to

$$P_r = \frac{3}{2} R_s \left(\left(i_{qs}^r\right)^2 + \left(i_{ds}^r\right)^2 \right) \tag{2.17}$$

The dc conduction loss is calculated at each operating point. Then the weighted power loss is calculated by taking the dot product of the conduction power loss vector for all operating point with a weighing vector. This operation is given as

$$P_{rw} = \mathbf{P}_r \mathbf{w}_x^T \tag{2.18}$$

where $\mathbf{w}_x^T$ is one of the weighting vectors listed in the design specifications and superscript *T* denotes transpose operation.

The stage is now set to introduce the design space, constraints and the fitness function. The design space is given by

$$\boldsymbol{\theta} = \left[L_q \;\; L_d \;\; \phi_{dm} \;\; \alpha_m \;\; i_{qs,1}^r \;\; i_{ds,1}^r \;\; i_{qs,2}^r \;\; i_{ds,2}^r \;\; i_{qs,3}^r \;\; i_{ds,3}^r \right] \tag{2.19}$$

where α_m is a fraction to control the flux in the permanent magnet. Thus, the permanent magnet flux linkage is given by

$$\lambda_m = \alpha_m \lambda_{m,mx} \tag{2.20}$$

where $\lambda_{m,mx}$ is the maximum attainable permanent magnet flux linkage given in the design specifications.

Two constraints are imposed on the design problem. These are implemented using a 'less than' and a 'greater than' function. The 'less than' function is defined as

$$\mathrm{ltn}\left(x, x_0\right) = \begin{cases} 1 & x \le x_0 \\ \dfrac{1}{1 + x - x_0} & x > x_0 \end{cases} \tag{2.21}$$

where x is the quantity to be constrained and x_0 is the allowed upper limit. If x is less than x_0, then the less than function returns a value of 1. However, if x exceeds the upper limit, then the value returned by the functions rapidly decreases towards 0.

Similarly, the 'greater than' function is used to compare a quantity to a lower allowed limit. It is defined as

$$\mathrm{gtn}\left(x, x_0\right) = \begin{cases} 1 & x \ge x_0 \\ \dfrac{1}{1 + x_0 - x} & x < x_0 \end{cases} \tag{2.22}$$

When x is greater than the lower limit, the output of the function is equal to 1. When x is smaller than the lower limit, the function returns value that decreases rapidly ltowards 0 as the difference between the limit and the quantity of interest goes to infinity.

The first constraint applied is a limit on the maximum line-to-line voltage. The maximum line-to-line voltage limit is equal to v_{dc} (ignoring any forward semiconductor voltage drops). The constraint is expressed as

$$c_1 = \mathrm{ltn}\left(\max\left(\mathbf{v}_{ll,pk}\right), v_{dc}\right) \tag{2.23}$$

where $\mathbf{v}_{pk,ll}$ is a vector of peak line-to-line voltages at all operating point, each calculated using (2.12).

The second constraint applied ensures that the output torque at every operating point, calculated using (2.14), is greater than or equal to the target torque given by the design specifications. This constraint is expressed as

$$c_2 = \text{gtn}\left(\min\left(\mathbf{T}_e - \mathbf{T}_e^*\right), 0\right) \tag{2.24}$$

where $\mathbf{T}_e$ is the calculated torque vector for each operating point and $\mathbf{T}_e^*$ is the target torque vector defined in Table 2.1. The average of c_1 and c_2 is given as

$$\hat{c} = \frac{c_1 + c_2}{2} \tag{2.25}$$

Finally, the fitness function is expressed as

$$\text{f}\left(\boldsymbol{\theta}\right) = \begin{cases} \dfrac{\hat{c} - 1}{10^3} & \hat{c} < 1 \\ \dfrac{1}{P_{rw}} & \hat{c} = 1 \end{cases} \tag{2.26}$$

In the next section, a number of design configurations are introduced. These configurations provide an insight on the advantages obtained in the improving the machine performance as a result of the ideas proposed in this thesis.

2.3 Design Configurations

To obtain insight on the effectiveness of the machine structure proposed in this work, four design space configurations are considered. Configuration 1 represent a nominal PMSM machine, were torque is solely produced from the interaction between the *q*-axis current and the permanent magnet flux. All parameters in this case are fixed except for the *qd* currents at the three operating points. Configuration 2 is similar to the configuration 1 but allows a weaker permanent magnet to be chosen if needed by the design algorithm. Configuration 3 adds symmetrical saliency into the design space used by allowing L_q and L_d to vary. The only fixed parameter in this case is ϕ_{dm}, which will

be set to zero. Finally, configuration 4 allows designing a machine that has an asymmetrical saliency by setting ϕ_{dm} to a value between 0 and $\pi/2$. All design parameters in configuration 4 are set free to be chosen between their maximum and minimum limits. Tables 2.2-2.5 show these configurations and the maximum and minimum limits on each of the design parameters defined in (2.19).

The single objective optimization analysis described in Section 2.2 is applied for all four configurations. For each configuration, the optimization is done three time with each weighting vector, $\mathbf{w}_1$, $\mathbf{w}_2$ and $\mathbf{w}_3$, which are listed in Table 2.1. In total, 12 studies are conducted and their results are discussed in the next section.

Table 2.2
Design Parameters – Configuration 1 (Nominal Machine)

Parameter	Minimum	Maximum	Units
L_q	1.70	1.70	mH
L_d	1.70	1.70	mH
ϕ_{dm}	0	0	rad
α_m	1	1	N/A
$i^r_{qs,1}$	0	206	A
$i^r_{ds,1}$	-103	103	A
$i^r_{qs,2}$	0	206	A
$i^r_{ds,2}$	-103	103	A
$i^r_{qs,3}$	0	206	A
$i^r_{ds,3}$	-103	103	A

Table 2.3

Design Parameters – Configuration 2 (Adjustable Permanent Magnet Flux)

Parameter	Minimum	Maximum	Units
L_q	1.70	1.70	mH
L_d	1.70	1.70	mH
ϕ_{dm}	0	0	rad
α_m	0.1	1	N/A
$i^r_{qs,1}$	0	206	A
$i^r_{ds,1}$	-103	103	A
$i^r_{qs,2}$	0	206	A
$i^r_{ds,2}$	-103	103	A
$i^r_{qs,3}$	0	206	A
$i^r_{ds,3}$	-103	103	A

Table 2.4

Design Parameters – Configuration 3 (Symmetrical Saliency)

Parameter	Minimum	Maximum	Units
L_q	1.70	3.40	mH
L_d	1.70	3.40	mH
ϕ_{dm}	0	0	rad
α_m	0.1	1	N/A
$i^r_{qs,1}$	0	206	A
$i^r_{ds,1}$	-103	103	A
$i^r_{qs,2}$	0	206	A
$i^r_{ds,2}$	-103	103	A
$i^r_{qs,3}$	0	206	A
$i^r_{ds,3}$	-103	103	A

Table 2.5
Design Parameters – Configuration 4 (Asymmetrical Saliency)

Parameter	Minimum	Maximum	Units
L_q	1.70	3.40	mH
L_d	1.70	3.40	mH
ϕ_{dm}	0	$\pi/2$	Rad
α_m	0.10	1	N/A
$i^r_{qs,1}$	0	206	A
$i^r_{ds,1}$	-103	103	A
$i^r_{qs,2}$	0	206	A
$i^r_{ds,2}$	-103	103	A
$i^r_{qs,3}$	0	206	A
$i^r_{ds,3}$	-103	103	A

2.4 Results and Discussions

The optimization studies were conducted using a genetic algorithm [31]. In each study, the population size was set equal to 1500 while the number of generation was set equal to 100.

Figs 2.2-2.5 show a subplot of the gene distribution and the design fitness for each of the four configurations with the power loss weighted using $\mathbf{w}_1$. The genes are ordered as listed in (2.19) and are shown normalized between 0 and 1. The x-axis denotes the number of generations. A detailed explanation of the gene distribution plot is set forth in [28].

Genes 1-4 in Fig 2.2 denote design parameters L_q, L_d, ϕ_{dm} and α_m. They were forced to a constant by equating the minimum and maximum limits. This explains the non-convergence witnessed in their respective normalized genes. Genes 5-10 denote the *qd* currents at the three operating points. It is observed that these parameters converged properly in the specified range. In the second subplot in Fig. 2.2, three traces are shown. The blue trace denotes the best design fitness value in a design generation, the green trace denotes the median fitness value in a design generation, and the red trace denotes the mean fitness value in a design generation. At the final generation, generation 100, the best fitness converged to a value close to 6×10^{-4} W^{-1}.

The same explanation stated above can be used to describe Figs 2.3-2.6. Note that when parameters L_q, L_d and α_{dm}, are allowed to vary, they are chosen at their maximum or minimum limits. Since the problem is formulated to achieve a required torque and lower copper losses, there is no advantage in setting α_m less than 1 as long as the voltage limit is not violated, which seems to be the case in these studies. The inductances L_q and L_d are chosen at opposite limits in configurations 3 and 4; L_q at the maximum limit and L_d at the minimum limit. This behavior can be understood by inspecting equation (2.15), which shows that the reluctance torque depends on the difference between these inductances. In other words, the greater the difference is, the more salient the machine is and more reluctance torque can be produced. Note that the choice on which inductance is bigger is made depending on the sign of i_{ds}^r, such that a positive reluctance torque is produced.

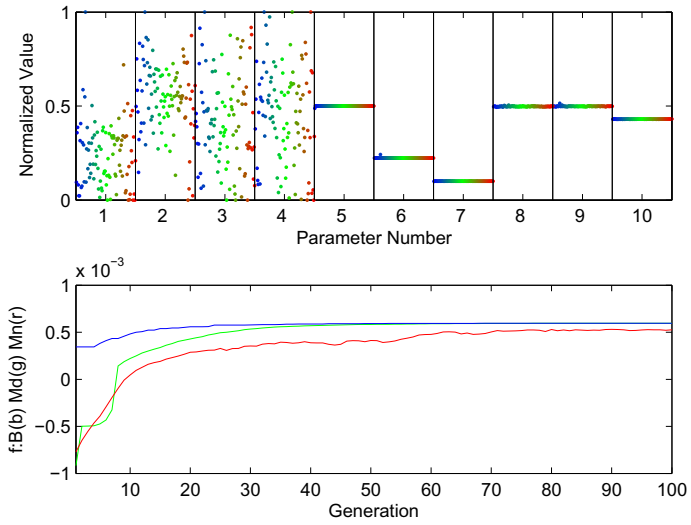

Fig. 2.3. Gene distribution and fitness evolution plots for Configuration 1 (nominal machine) using weighting vector $\mathbf{w}_1$

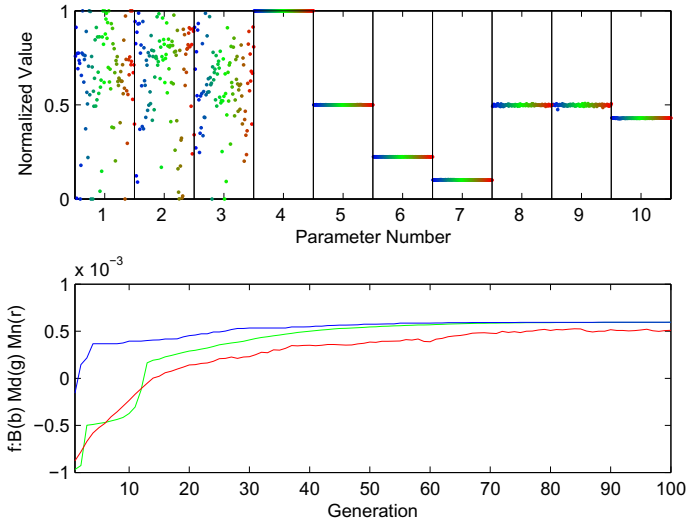

Fig. 2.4. Gene distribution and fitness evolution plots for Configuration 2 (adjustable magnet) using weighting vector $\mathbf{w}_1$

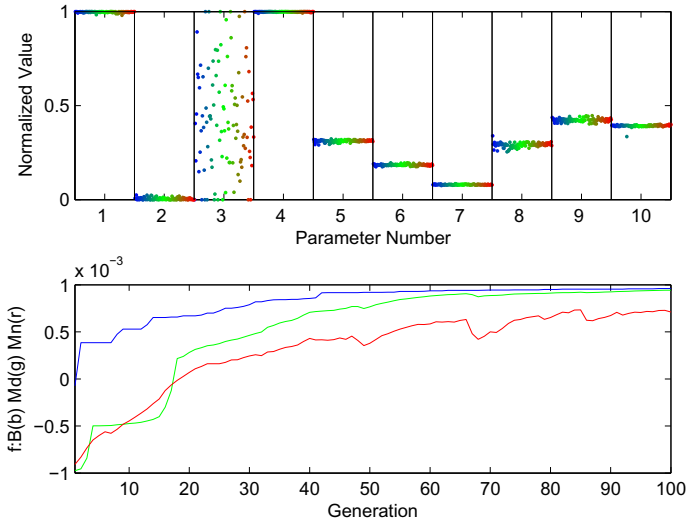

Fig. 2.5. Gene distribution and fitness evolution plots for Configuration 3 (symmetrical saliency) using weighting vector $\mathbf{w}_1$

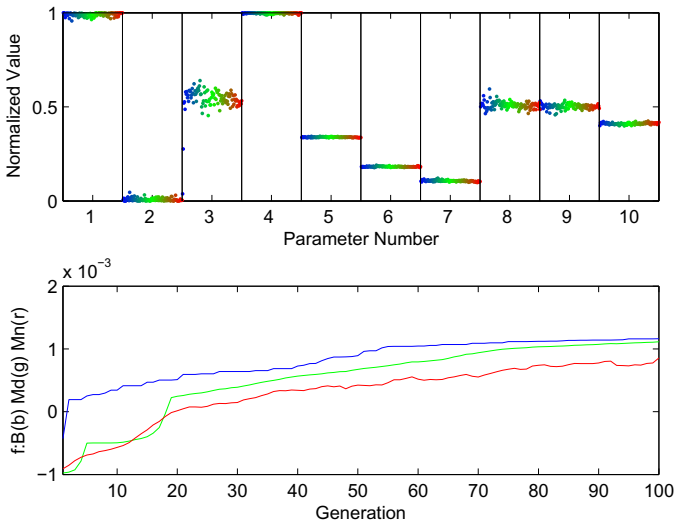

Fig. 2.6. Gene distribution and fitness evolution plots for Configuration 4 (asymmetrical saliency) using weighting vector $\mathbf{w}_1$

The design parameters obtained for each of the four configuration studies using weighting vector $\mathbf{w}_1$ are shown in Tables 2.6-2.9. Also shown in these tables are the reluctance torque vector, permanent magnet torque vector, overall torque vector and the best design fitness value. A number of important points can be made with regards to the results presented in Tables 2.6-2.9.

In Table 2.6, where Configuration 1 (nominal machine) is considered, saliency does not exist and torque is produced solely due to the interaction between the *q*-axis current and permanent magnet flux. It is observed that a relatively large *q*-axis current is chosen at the first and second operating points to satisfy the torque constraint, c_2. At the third operating point, with a rotor speed of 5000 rpm, the *q*-axis current is reduced while an injection of *d*-axis current occurs. This is done to satisfy the constraint set on the maximum line-line voltage, constraint c_1. The best design fitness achieved for this configuration, which equal to the inverse of the weighted power loss, was found to be equal to 6×10^{-4} W^{-1}.

Table 2.7 lists configuration 2 (adjustable magnet) results. The results are similar to that in Configuration 1. The design specifications and constraints can be satisfied without reducing α_m below 1 (i.e. : using a weaker magnet).

In Table 2.8, Configuration 3 (symmetrical saliency) results are presented. The *q*-axis inductance evolved to its maximum limit while the *d*-axis inductance was set at its minimum limit. This allowed reluctance torque to be generated. Note that the second term

on the right hand side of the reluctance torque expression, (2.15), is equal to zero because ϕ_{dm} in this configuration is enforced to zero. Thus, reluctance torque is proportional to the product of the *qd* currents and the difference $L_d - L_q$. Which inductance, L_q or L_d, is greater than the other depends on the sign of the *d*-axis current, such that a positive reluctance torque is produced (the *d*-axis current gene has the freedom to be chosen as a positive value).

Injecting considerable *d*-axis current to create saliency torque can lead to a high power loss profile, and therefore it might seem from an initial look that saliency torque is not advantageous and should be eliminated by choosing the *qd* inductances equal. However, comparing the sum $\left(i_{qs}^r\right)^2 + \left(i_{ds}^r\right)^2$, which is proportional to the square of the rms current, in Configuration 3 to that in Configurations 1 and 2, shows that a smaller rms current is utilized in Configuration 3. This gives a lower power loss as in this configuration than the previous configurations, as can be deduced from (2.17). In Configuration 3, reluctance torque contributed with around 38.4%, 18.7%, and 22.6% of the total torque produced at the first, second and third operating points respectively. Thus, less *q*-axis current was needed, which decreased the overall loss and improved the design fitness.

Configuration 4 (asymmetrical saliency), enables all design parameters to vary between their specified minimum and maximum limits. In particular, the phase shift angle ϕ_{dm} is set between a minimum of 0 and a maximum of $\pi/2$.

A considerable phase shift equal to 0.78 rad (44.7°) was picked by the optimization algorithm. Also noted was a close to zero *d*-axis current in operating points 1 and 2. A closer inspection into (2.15) implies that most of saliency torque produced at operating points 1 and 2 is due to the second term on the right hand side with little contribution from the first term. Since negligible *d*-axis current is injected at the first and second operating points, losses in this configuration are smaller than that in the Configuration 3. The percentage of torque produced from reluctance torque at the first, second and third operating points is 33.1 %, 20.6 %, and 4.50%, respectively. The best fitness obtained in this configuration is 1.2×10^{-3} W^{-1} and was found to be the highest compared to all design configurations using weighting vector $\mathbf{w}_1$.

TABLE 2.6
Configuration 1 (Nominal Machine) Results Using Weighting Vector $\mathbf{w}_1$

Parameter	Value	Units
L_q	1.70	mH
L_d	1.70	mH
ϕ_{dm}	0	rad
α_m	1	N/A
$\mathbf{i}_{qs}^r$	[103, 46.2, 20.7]	A
$\mathbf{i}_{ds}^r$	[-0.28, -0.31, -14.2]	A
$\mathbf{T}_{ex}$	[0, 0, 0]	Nm
$\mathbf{T}_{em}$	[35.6, 15.9, 7.13]	Nm
$\mathbf{T}_e$	[35.6, 15.9, 7.13]	Nm
P_{rw}	1.67	kW
$\mathrm{f}(\boldsymbol{\theta})$	6×10^{-4}	W^{-1}

TABLE 2.7
Configuration 2 (Adjustable Magnet) Results Using Weighting Vector $\mathbf{w}_1$

Parameter	Value	Units
L_q	1.70	mH
L_d	1.70	mH
ϕ_{dm}	0	rad
α_m	1	N/A
$\mathbf{i}_{qs}^r$	[103.3, 46.2, 20.7]	A
$\mathbf{i}_{ds}^r$	[-0.65, -0.04, -14.4]	A
$\mathbf{T}_{ex}$	[0, 0, 0]	Nm
$\mathbf{T}_{em}$	[35.6, 15.9, 7.14]	Nm
$\mathbf{T}_e$	[35.6, 15.9, 7.14]	Nm
P_{rw}	1.67	kW
$\mathrm{f}(\boldsymbol{\theta})$	6×10^{-4}	W^{-1}

TABLE 2.8
Configuration 3 (Symmetrical Saliency) Results Using Weighting Vector $\mathbf{w}_1$

Parameter	Value	Units
L_q	3.30	mH
L_d	1.70	mH
ϕ_{dm}	0	rad
α_m	1	N/A
$\mathbf{i}_{qs}^r$	[65.8, 37.8, 16.1]	A
$\mathbf{i}_{ds}^r$	[-43.8, -15.5, -20.4]	A
$\mathbf{T}_{ex}$	[13.8, 3.00, 1.62]	Nm
$\mathbf{T}_{em}$	[22.0, 13.0, 5.55]	Nm
$\mathbf{T}_e$	[35.9, 16.0, 7.18]	Nm
P_{rw}	1.0	kW
$\mathrm{f}(\boldsymbol{\theta})$	1×10^{-3}	W^{-1}

TABLE 2.9
Configuration 4 (Asymmetrical Saliency) Results Using Weighting Vector $\mathbf{w}_1$

Parameter	Value	Units
L_q	3.30	mH
L_d	1.70	mH
ϕ_{dm}	0.78	rad
α_m	1	N/A
$\mathbf{i}_{qs}^r$	[69.2, 36.9, 19.7]	A
$\mathbf{i}_{ds}^r$	[2.10, -4.50, -16.3]	A
$\mathbf{T}_{ex}$	[11.8, 3.30, 0.32]	Nm
$\mathbf{T}_{em}$	[23.9, 12.7, 6.80]	Nm
$\mathbf{T}_e$	[35.6, 16.0, 7.12]	Nm
P_{rw}	0.83	kW
$\mathrm{f}(\boldsymbol{\theta})$	1.2×10^{-3}	W^{-1}

All four configurations were repeated using weighting vector $\mathbf{w}_2$ and $\mathbf{w}_3$. The results obtained followed a similar pattern and are listed in Tables 2.10-2.17. An interesting behavior is found in Table 2.12, where results from Configuration 3 using weighting vector $\mathbf{w}_2$ are shown. Therein, $L_d > L_q$ and as expected, the *d*-axis currents at the first and second operating points where chosen positive to allow generating a positive reluctance torque. However, at the third operating point, a negative *d*-axis current was chosen, which gives a negative reluctance torque. Yet, the torque constraint was still satisfied since enough permanent magnet torque was produced. The reason for this behavior is that this weighting function $\mathbf{w}_2$ weighs the third operating point by 10%. Therefore, loss in the third operating point is insignificant to the total weighted loss, and although negative reluctance torque is not advantageous, enough *q*-axis current can be injected to overshadow the negative reluctance torque.

TABLE 2.10
Configuration 1 (Nominal Machine) Results Using Weighting Vector $\mathbf{w}_2$

Parameter	Value	Units
L_q	1.70	mH
L_d	1.70	mH
ϕ_{dm}	0	rad
α_m	1	N/A
$\mathbf{i}_{qs}^r$	[103, 46.2, 20.6]	A
$\mathbf{i}_{ds}^r$	[-0.10, 0.14, -14.3]	A
$\mathbf{T}_{ex}$	[0, 0, 0]	Nm
$\mathbf{T}_{em}$	[35.6, 15.9, 7.12]	Nm
$\mathbf{T}_e$	[35.6, 15.9, 7.12]	Nm
P_{rw}	3.03	kW
$\mathrm{f}(\boldsymbol{\theta})$	3.3×10^{-4}	W^{-1}

TABLE 2.11
Configuration 2 (Adjustable Magnet) Results Using Weighting Vector $\mathbf{w}_2$

Parameter	Value	Units
L_q	1.70	mH
L_d	1.70	mH
ϕ_{dm}	0	rad
α_m	1	N/A
$\mathbf{i}_{qs}^r$	[103, 46.2, 20.7]	A
$\mathbf{i}_{ds}^r$	[0.24, -0.40, -14.2]	A
$\mathbf{T}_{ex}$	[0, 0, 0]	Nm
$\mathbf{T}_{em}$	[35.6, 15.9, 7.14]	Nm
$\mathbf{T}_e$	[35.6, 15.9, 7.14]	Nm
P_{rw}	3.03	kW
$\mathrm{f}(\boldsymbol{\theta})$	3.3×10^{-4}	W^{-1}

TABLE 2.12
Configuration 3 (Symmetrical Saliency) Results Using Weighting Vector $\mathbf{w}_2$

Parameter	Value	Units
L_q	1.70	mH
L_d	3.30	mH
ϕ_{dm}	0	rad
α_m	1	N/A
$\mathbf{i}_{qs}^r$	[66.6, 41.1, 29.8]	A
$\mathbf{i}_{ds}^r$	[40.0, 14.3, -16.4]	A
$\mathbf{T}_{ex}$	[13.0, 2.90, -2.40]	Nm
$\mathbf{T}_{em}$	[22.97, 14.2, 10.3]	Nm
$\mathbf{T}_e$	[40.0, 17.0, 7.90]	Nm
P_{rw}	1.75	kW
$\mathrm{f}(\boldsymbol{\theta})$	5.7×10^{-4}	W^{-1}

TABLE 2.13
Configuration 4 (Asymmetrical Saliency) Results Using Weighting Vector $\mathbf{w}_2$

Parameter	Value	Units
L_q	3.30	mH
L_d	1.70	mH
ϕ_{dm}	0.81	rad
α_m	1	N/A
$\mathbf{i}_{qs}^r$	[69.1, 35.6, 22.0]	A
$\mathbf{i}_{ds}^r$	[2.50, 0.94, -17.9]	A
$\mathbf{T}_{ex}$	[11.8, 3.30, 0.29]	Nm
$\mathbf{T}_{em}$	[23.8, 12.6, 7.60]	Nm
$\mathbf{T}_e$	[35.6, 15.9, 7.88]	Nm
P_{rw}	1.39	kW
$\mathrm{f}(\boldsymbol{\theta})$	7.2×10^{-4}	W^{-1}

TABLE 2.14
Configuration 1 (Nominal Machine) Results Using Weighting Vector $\mathbf{w}_3$

Parameter	Value	Units
L_q	1.70	mH
L_d	1.70	mH
ϕ_{dm}	0	rad
α_m	1	N/A
$\mathbf{i}_{qs}^r$	[103, 46.2, 20.6]	A
$\mathbf{i}_{ds}^r$	[-0.36, -0.01, -14.2]	A
$\mathbf{T}_{ex}$	[0, 0, 0]	Nm
$\mathbf{T}_{em}$	[35.6, 15.9, 7.12]	Nm
$\mathbf{T}_e$	[35.6, 15.9, 7.12]	Nm
P_{rw}	0.71	kW
$\mathrm{f}(\boldsymbol{\theta})$	1.4×10^{-3}	W^{-1}

TABLE 2.15
Configuration 2 (Adjustable Magnet) Results Using Weighting Vector $\mathbf{w}_3$

Parameter	Value	Units
L_q	1.7	mH
L_d	1.7	mH
ϕ_{dm}	0	rad
α_m	1	N/A
$\mathbf{i}_{qs}^r$	[103, 46.2, 20.6]	A
$\mathbf{i}_{ds}^r$	[0.50, 0.14, -14.2]	A
$\mathbf{T}_{ex}$	[0, 0, 0]	Nm
$\mathbf{T}_{em}$	[35.6, 15.9, 7.12]	Nm
$\mathbf{T}_e$	[35.6, 15.9, 7.12]	Nm
P_{rw}	0.71	kW
$\mathrm{f}(\boldsymbol{\theta})$	1.4×10^{-3}	W^{-1}

TABLE 2.16
Configuration 3 (Symmetrical Saliency) Results Using Weighting Vector $\mathbf{w}_3$

Parameter	Value	Units
L_q	3.30	mH
L_d	1.70	mH
ϕ_{dm}	0	rad
α_m	1	N/A
$\mathbf{i}_{qs}^r$	[63.1, 36.8, 16.1]	A
$\mathbf{i}_{ds}^r$	[-46.6, -18.4, -20.2]	A
$\mathbf{T}_{ex}$	[14.2, 3.30, 1.57]	Nm
$\mathbf{T}_{em}$	[21.8, 12.7, 5.55]	Nm
$\mathbf{T}_e$	[36.0, 16.0, 7.12]	Nm
P_{rw}	0.53	kW
$\mathrm{f}(\boldsymbol{\theta})$	1.9×10^{-3}	W^{-1}

TABLE 2.17
Configuration 4 (Asymmetrical Saliency) Results Using Weighting Vector $\mathbf{w}_3$

Parameter	Value	Units
L_q	3.30	mH
L_d	1.70	mH
ϕ_{dm}	0.87	Rad
α_m	1	N/A
$\mathbf{i}_{qs}^r$	[70.6, 36.7, 20.2]	A
$\mathbf{i}_{ds}^r$	[-6.80, 2.50, -15.1]	A
$\mathbf{T}_{ex}$	[11.3, 3.30, 0.15]	Nm
$\mathbf{T}_{em}$	[24.3, 12.6, 7.00]	Nm
$\mathbf{T}_e$	[35.6, 16.0, 7.10]	Nm
P_{rw}	0.45	kW
$\mathrm{f}(\boldsymbol{\theta})$	2.2×10^{-3}	W^{-1}

For each weighting function, the fitness obtained for each of the four configurations was normalized based on Configuration 1 (nominal machine). Table 2.18 lists the normalized finesses for all studies. The normalized fitness is denoted as $\frac{\mathrm{f}_\zeta(\boldsymbol{\theta})}{\mathrm{f}_1(\boldsymbol{\theta})}$, where subscript ζ is the configuration number. In summary, Configuration 4 (asymmetrical saliency) gave the best loss metric for all weighting choices. This is particularly true for weighting vector $\mathbf{w}_2$ which emphasizes low-speed performance.

This chapter provided the initial basis for considering an Asymmetrical Salient Permanent Magnet Synchronous Machine (AS-PMSM). It has been shown that considerable torque and efficiency improvements are made possible by this machine structure, as was summarized in Table 2.18.

This study however includes some limitations. It was shown in a more inclusive study [19], that a salient machine, similar to the magnetic structure in Configuration 3, gives no superior improvements compared to a non-salient machine, such as machine Configurations 1 and 2, when the Pareto-optimal front between loss and mass is compared. As was pointed out therein, the presence of rotor tooth leads to an increase flux transfer between the stator and rotor. The additional flux will cause an increased core

TABLE 2.18
Normalized Fitness Values for All 12 Studies

Design Configuration	$\frac{f_\zeta(\theta)}{f_1(\theta)}$, w_1	$\frac{f_\zeta(\theta)}{f_1(\theta)}$, w_2	$\frac{f_\zeta(\theta)}{f_1(\theta)}$, w_3
Nominal Machine	1	1	1
Adjustable Magnet	1	1	1
Symmetrical Saliency	1.67	1.73	1.36
Asymmetrical Saliency	2.00	2.20	1.57

loss in the stator teeth and backiron. Also, an increase in the overall machine's mass is needed to accommodate the additional flux. These drawbacks explain why a salient machine did not show better performance compared to a non-salient machine in CPSR applications.

Hence, to be confident about the benefits predicted by the results Table 2.18, a detailed study of the asymmetrical salient machine configuration is required. This is considered in the next chapter, where a formal design and analysis of an AS-PMSM is presented.

3. ASYMMETRICAL SALIENT PERMANENT MAGNET MACHINE ANALYSIS

Chapter 2 provided motivation to consider a detailed design of an Asymmetrical Salient Permanent Magnet Synchronous Machine (AS-PMSM). A detailed analysis of the AS-PMSM is set forth herein to support a multi-objective optimization based design. The analysis done here is similar to that done for a nominal SM-PMSM in [28].

The order of this chapter is as follows. In Section 3.1, the geometry of the AS-PMSM is described, where geometrical parameters are calculated in terms of a set of independent machine design parameters. In Section 3.2, the stator winding configuration is discussed. In Section 3.3, the machine's material properties are considered. In Section 3.4 a discussion of the electrical current control philosophy utilized to control the machine is provided. In Section 3.5, the flux density in the region between the rotor backiron and the stator tooth is formulated. An important assumption in this formulation is assuming that the field is solely in the radial direction. Section 3.6 includes a derivation of the lumped model parameters. Section 3.7 briefly describes procedure to apply ferromagnetic field analysis. The procedure is similar to that presented in [28] and hence only a brief discussion to clarify some points is presented. The chapter concludes with Section 3.8, were expressions for ac losses, in particular skin effect and proximity effect losses are formulated.

3.1 Geometrical Analysis

A cross section of an 12-pole, 3-phase AS-PMSM is shown in Fig. 3.1. The rotor position θ_{rm} is measured in the counter-clockwise direction from the *a*-phase magnetic axis. A spatial angle ϕ_{sm} is measured with respect a-phase axis. Another useful angle is the spatial position with respect to the rotor position ϕ_{rm}. The relation between θ_{rm}, ϕ_{sm} and ϕ_{rm} is given as

$$\phi_{sm} = \theta_{rm} + \phi_{rm} \tag{3.1}$$

Labeled in Fig. 3.1 is the stator back iron, a stator tooth and a stator slot, the three phase conductors, a radially magnetized permanent magnet, the rotor back iron, inert material and the shaft. The rotor contains a rotor teeth positioned next to the permanent magnets in an asymmetrical fashion. The machine laminations are assumed to be axially stacked.

Note that the stator teeth in the figure do not include a tooth tip. Usually a tooth tip is added to increase the span of the tooth and allow more flux to enter and leave the stator. In order to simplify the analysis however, tooth tips are not considered at this point.

It was shown in [19] that adding a symmetrical pair of rotor teeth (symmetrical saliency) surrounding each PM gives no advantage to the machine performance. However, in this work, it will be shown that by having an asymmetrical rotor tooth design, an increase in the machine efficiency in a CPSR application is obtained.

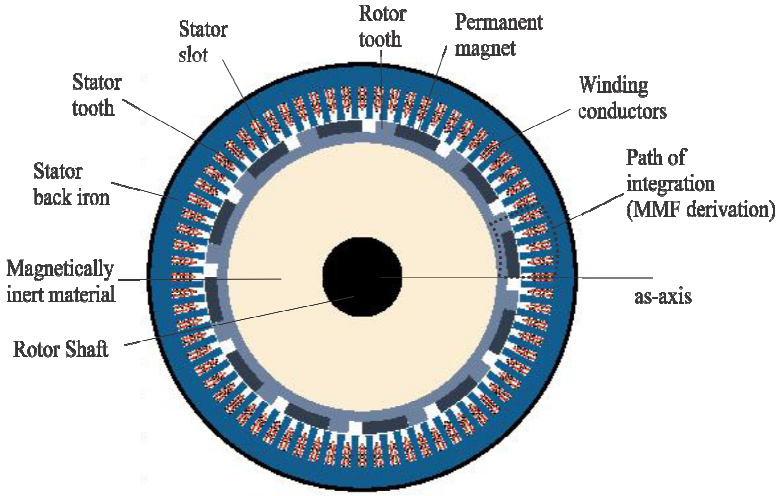

Fig. 3.1. Cross section of a sample 12 pole AS-PMSM

A detailed drawing of a stator tooth is shown in Fig. 3.2. Therein, r_{st} is the radius from the center of the machine cross section to the center of a stator tooth, r_{sb} is the radius to a tooth base, and r_{ss} is the radius to the outer boundary of the stator back iron. The height of a tooth base is denoted by d_{tb}, the width of a tooth is denoted by w_{tb} and the thickness of the stator back iron is denoted as d_{sb}. The angle from the tooth center to the tooth tip is denoted by θ_t while the angle spanning the tooth base circumference at $r = r_{sb}$ is denoted by θ_{tb}. The span of a stator slot is denoted by θ_{st}. Note that

$$\theta_{st} + \theta_t = \frac{2\pi}{S_s} \tag{3.2}$$

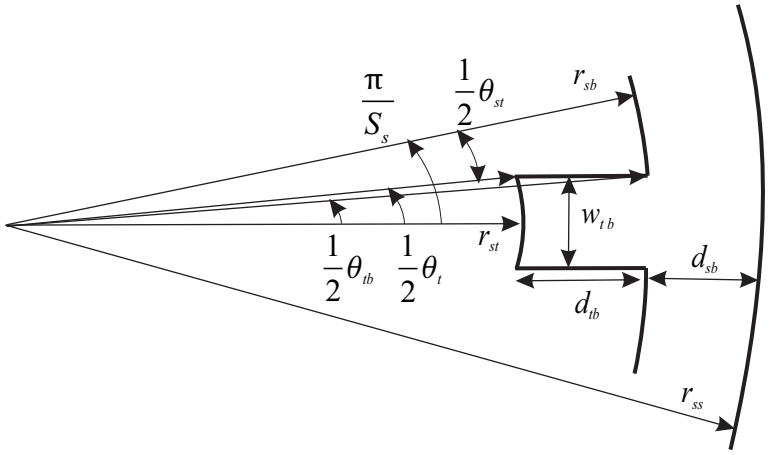

Fig. 3.2. Stator tooth

A developed diagram of a section of the rotor is shown in Fig 3.3. Note that the counter clockwise direction maps into a linear movement from right to left in the developed diagram Fig. 3.3.

The rotor shaft radius is denoted by r_{rs} while the inert material and rotor back iron depths are denoted by d_i and d_{rb} respectively. The radius to the outer boundary of the rotor back iron is denoted by r_{rb}. The depth of the permanent magnet is denoted by d_m while the air gap separating it from the stator region is g. The sum of the rotor back iron radius, the magnet depth and magnet-stator air gap, defines the radius to the stator region r_{st}. A rotor tooth is situated to the left of the PM with its depth denoted by d_{rt} and the air gap separating it from the stator region denoted by g_{rt}. Note that the depth of the rotor tooth can be set greater than, equal to, or less than the depth of the permanent magnet. The rotor can be tapered if needed by setting the value of the fraction α_{tap} below 1, as shown in the figure. The tapering follows a similar approach to that taken in [4] however in this case it is applied optimimily instead of using a calculated trajectory.

The span of the permanent magnet, rotor teeth, and space at the end of the pole which is sometimes filled with inert material, are denoted by θ_{pm}, θ_{rt} and θ_{in}, respectively. The sum of these angles is equal to the span of a rotor pole θ_p. The dotted lines show the transition points. These are represented by spatial angular positions $\phi_{pt1,i}$, $\phi_{pt2,i}$, $\phi_{pt3,i}$, $\phi_{pt4,i}$ and $\phi_{pt5,i}$, where subscript *i* denotes the magnetic pole number.

An angular position dependent radius $\mathbf{r}_{rg}$ (which can be written as $\mathrm{r}_{rg}(\phi_{rm})$) is used to define the outer boundary of the rotor tooth and permanent magnet by the following relationship

$$\mathrm{r}_{rg}\left(\phi_{rm}\right)=\begin{cases} r_{rb}+d_m & \phi_{pt1,i}\le\phi_{rm}\le\phi_{pt2,i} \\ \left[\dfrac{d_{rt}\left(1-\alpha_{tap}\right)}{\theta_{rt}}\phi_{rm}+\dfrac{\left(d_{rt}+r_{rb}\right)\theta_{rt}+d_{rt}\left(1-\alpha_{tap}\right)\phi_{pt2,i}}{\theta_{rt}}\right] & \phi_{pt2,i}\le\phi_{rm}\le\phi_{pt3,i} \\ r_{rb} & \phi_{pt3,i}\le\phi_{rm}\le\phi_{pt4,i} \end{cases} \tag{3.3}$$

The value of $\mathrm{r}_{rg}\left(\phi_{rm}\right)$ over the span of the rotor tooth is derived using a linear line equation. Similarly a position dependent air gap $\mathbf{g}_v$ (which can be written as $\mathrm{g}_v\left(\phi_{rm}\right)$) is defined using

$$\mathrm{g}_v\left(\phi_{rm}\right)=r_{st}-\mathrm{r}_{rg}\left(\phi_{rm}\right) \tag{3.4}$$

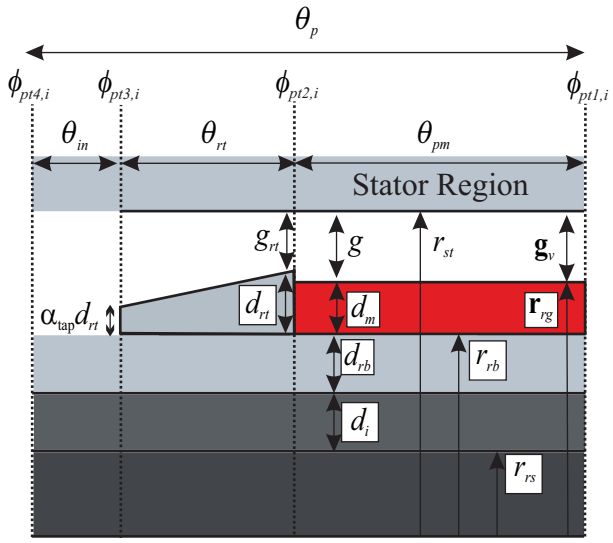

Fig. 3.3. Developed diagram of a rotor pole

Before proceeding, a number of geometrical variables are chosen as independent machine design parameters. These parameters will be chosen optimally in the next chapter when the machine design is treated. One possible choice for these independent geometrical parameters is

$$\mathbf{G}_I = \left[P_p \;\; d_i \;\; d_{rb} \;\; d_m \;\; g \;\; d_{tb} \;\; \alpha_t \;\; d_{sb} \;\; \alpha_{pm} \;\; l \;\; g_{rt}^* \;\; \alpha_{rt} \;\; \alpha_{tap} \right]^T \tag{3.5}$$

where P_p designates the number of pole pairs, α_t, α_{pm} and α_{rt} are fractions between 0 and 1 used to set the span of the stator tooth, PM and rotor tooth, respectively. The stack length of the machine is denoted by l (all laminations and PMs have the same stack length). The maximum air gap (i.e.: $\phi_{rm} = \phi_{pt2,i}$) between the rotor tooth and the stator region is set using target air gap g_{rt}^* by the following

$$g_{rt} = \min\left(g_{rt}^*, g + d_m \right) \tag{3.6}$$

where 'min' is a function that finds the minimum of its arguments. Equation (3.6) ensures that the depth of the rotor tooth is greater than zero.

Parameters in (3.5) are used to find the following dependent geometrical variables

$$P = 2P_p \tag{3.7}$$

$$S_s = 3P n_{spp} \tag{3.8}$$

$$r_{rb} = r_{rs} + d_i + d_{rb} \tag{3.9}$$

$$r_{st} = r_{rb} + d_m + g \tag{3.10}$$

$$d_{rt} = r_{st} - g_{rt} - r_{rb} \tag{3.11}$$

$$\theta_t = \alpha_t \frac{2\pi}{S_s} \tag{3.12}$$

$$\theta_{st} = \left(1 - \alpha_t\right) \frac{2\pi}{S_s} \tag{3.13}$$

$$\theta_{pm} = \alpha_{pm} \frac{2\pi}{P} \tag{3.14}$$

$$\theta_{rt} = \left(1 - \alpha_{pm}\right) \frac{\pi}{P} \alpha_{rt} \tag{3.15}$$

$$\theta_{in} = \left(1 - \alpha_{pm}\right) \frac{\pi}{P} \left(1 - \alpha_{rt}\right) \tag{3.16}$$

$$w_{tb} = 2 r_{st} \sin\left(\frac{\theta_t}{2} \right) \tag{3.17}$$

$$r_{sb} = \sqrt{\left(r_{st} \cos\left(\frac{\theta_t}{2} \right) + d_{tb} \right)^2 + \frac{w_{tb}^2}{4}} \tag{3.18}$$

$$r_{ss} = r_{sb} + d_{sb} \tag{3.19}$$

$$\theta_{tb} = 2\text{asin}\left(\frac{w_{tb}}{2r_{sb}}\right) \tag{3.20}$$

$$w_{so} = 2r_{st}\sin\left(\frac{\theta_{st}}{2}\right) \tag{3.21}$$

$$\phi_{ss,y} = \frac{2\pi(y-1)}{S_s} + \phi_{ss,1} \tag{3.22}$$

$$\phi_{st,y} = \frac{2\pi\left(y-\frac{3}{2}\right)}{S_s} + \phi_{ss,1} \tag{3.23}$$

where P is the number of magnetic poles, n_{spp} is the number of slots per pole per phase, w_{so} is the slot opening, defined as the distance of an imaginary straight line joining to adjacent tooth tips. Equations (3.22) and (3.23) give the center angular location of the stator slot and stator tooth respectively, where $\phi_{ss,1}$ is the angular position of the center of the first stator slot. Therein, subscript y is the stator slot or tooth number. Note that $\phi_{st,y}$ is a different property than θ_{st}.

The surface area of the shaft a_{rs}, magnetic inert material a_i, rotor back iron a_{rb}, total permanent magnets a_{pm}, a single rotor tooth a_{rts}, a single stator tooth a_{tb}, a single stator slot a_{slt}, and stator back iron a_{sb} are given as

$$a_{rs} = \pi r_{rs}^2 \tag{3.24}$$

$$a_i = \pi r_i^2 - a_{rs} \tag{3.25}$$

$$a_{rb} = \pi\left(r_{rb}^2 - r_i^2\right) \tag{3.26}$$

$$a_{pm} = \pi\left(\left(r_{rb}+d_m\right)^2 - r_{rb}^2\right)\alpha_{pm} \tag{3.27}$$

$$a_{tb} = d_{tb}w_{tb} - \frac{\theta_t r_{st}^2}{2} + \frac{w_{tb}}{2}\sqrt{r_{st}^2 - \frac{w_{tb}^2}{4}} \tag{3.28}$$

$$a_{slt} = \frac{\pi}{S_s}\left(r_{sb}^2 - r_{st}^2\right) - a_{tb} \tag{3.29}$$

$$a_{sb} = \pi\left(r_{ss}^2 - r_{sb}^2\right) \tag{3.30}$$

The total volume of the shaft v_{rs}, inert material v_i, rotor backiron v_{rb}, rotor laminations v_{rl}, total permanent magnets v_{pm}, stator teeth v_{st}, stator backiron v_{sb} and stator laminations v_{sl} may be expressed as

$$v_{rs} = l\, a_{rs} \tag{3.31}$$
$$v_{i} = l\, a_{i} \tag{3.32}$$
$$v_{rb} = l\, a_{rb} \tag{3.33}$$
$$v_{rl} = v_{rt} + v_{rb} \tag{3.34}$$
$$v_{pm} = l\, a_{pm} \tag{3.35}$$
$$v_{st} = S_s\, l\, a_{tb} \tag{3.36}$$
$$v_{sb} = l\, a_{sb} \tag{3.37}$$
$$v_{sl} = v_{st} + v_{sb} \tag{3.38}$$

The volume of the rotor teeth v_{rt} was calculated by numerical integration. To calculate the leakage inductance associated with a phase winding, it is helpful to approximate the stator slot geometry into a rectangular slot, as shown in Fig. 3.4. The shaded region represents the area occupied by conductors.

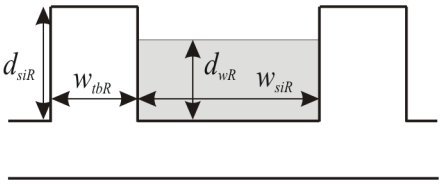

Fig. 3.4. Rectangular slot approximation

The width of the slot in this case is taken as the average of the slot width at $r = r_{st}$ (i.e. : w_{so}) and the slot width at $r = r_{sb}$ given as

$$w_{siR} = \frac{w_{so} + 2r_{sb}\sin\left(\dfrac{\pi}{S_s} - \dfrac{\theta_{tb}}{2}\right)}{2} \tag{3.39}$$

Maintaining the areas of the tooth base and tooth slot found in expressions (3.28) and (3.29) respectively, the width of the tooth base and depth of the slot are set in accordance with

$$w_{tbR} = \frac{a_{tb}}{d_{siR}} \tag{3.40}$$
$$d_{siR} = \frac{a_{slt}}{w_{siR}} \tag{3.41}$$

The parameter d_{wR} will be derived in the next section when the winding configuration is discussed. Next, a discussion of the stator winding configuration is presented.

3.2 Stator Winding

Winding configurations commonly used in 3-phase PM brushless machines can be classified as [32] as overlapping, either distributed or concentrated, or non-overlapping concentrated, often referred to as Fractional Slot Concentrated Winding (FSCW), with either all teeth wound or alternate teeth wound.

Overlapping distributed winding configuration produce a sinusoidal air gap MMF. However, increased interest have been shown towards FSCW configurations due to several advantages, such as short end turns and higher conductor slot fill factor which can be obtained using a segmented stator [32]. In this work, a direct objective is to increase the torque density without necessarily relying on segmented stator cores. In addition, although it was shown in [24] that the use of FSCW in a SM-PMSM can allow utilizing this machine topology in CPSR applications, core loss in permanent magnets and rotor steel due to the rich harmonic content in the air gap flux density can be a concern. Thus, an overlapping sinusoidally distributed 3-phase winding configuration with an integer slot per pole per phase number, n_{spp}, is adopted.

The continuous representation of the conductor density distribution may be expressed

$$\mathrm{n}_{as}\left(\phi_{sm}\right) = N_{s1}^{*}\left(\sin\left(\frac{P\phi_{sm}}{2}\right) - \alpha_3^{*}\sin\left(3\frac{P\phi_{sm}}{2}\right)\right) \tag{3.42}$$

$$\mathrm{n}_{bs}\left(\phi_{sm}\right) = N_{s1}^{*}\left(\sin\left(\frac{P\phi_{sm}}{2} - \frac{2\pi}{3}\right) - \alpha_3^{*}\sin\left(3\frac{P\phi_{sm}}{2}\right)\right) \tag{3.43}$$

$$\mathrm{n}_{cs}\left(\phi_{sm}\right) = N_{s1}^{*}\left(\sin\left(\frac{P\phi_{sm}}{2} + \frac{2\pi}{3}\right) - \alpha_3^{*}\sin\left(3\frac{P\phi_{sm}}{2}\right)\right) \tag{3.44}$$

where n_x is the conductor density of the x stator phase or winding, N_{s1}^{*} is the target amplitude of the fundamental conductor density component, and α_3^{*} is the target ratio between the 3rd harmonic component and the fundamental component. The third harmonic content is included to improve the slot fill factor.

To properly allocate conductors in the stator slots, discrete conductor density

configuration is needed. Transformation from a continuous conductor density distribution to a discrete distribution is possible using

$$N_{x,y} = \text{round}\left(\int_{\phi_{ss,y}-\pi/S_s}^{\phi_{ss,y}+\pi/S_s} \text{n}_x\left(\phi_{sm}\right) d\phi_{sm} \right) \tag{3.45}$$

where subscript y is the stator slot or tooth number and $\phi_{ss,y}$ is the center position of stator slot as calculated in (3.22). Substituting (3.42)-(3.44) into (3.45) and integrating gives

$$N_{as,y} = \text{round}\left(\frac{4N_{s1}^*}{P}\left(\sin\left(\frac{P}{2}\phi_{ss,y}\right)\sin\left(\frac{P}{2}\frac{\pi}{S_s}\right) - \frac{\alpha_3^*}{3}\sin\left(\frac{3P}{2}\phi_{ss,y}\right)\sin\left(\frac{3P}{2}\frac{\pi}{S_s}\right)\right)\right) \tag{3.46}$$

$$N_{bs,y} = \text{round}\left(\frac{4N_{s1}^*}{P}\left(\sin\left(\frac{P}{2}\phi_{ss,y} - \frac{2\pi}{3}\right)\sin\left(\frac{P}{2}\frac{\pi}{S_s}\right) - \frac{\alpha_3^*}{3}\sin\left(\frac{3P}{2}\phi_{ss,y}\right)\sin\left(\frac{3P}{2}\frac{\pi}{S_s}\right)\right)\right) \tag{3.47}$$

$$N_{cs,y} = \text{round}\left(\frac{4N_{s1}^*}{P}\left(\sin\left(\frac{P}{2}\phi_{ss,y} + \frac{2\pi}{3}\right)\sin\left(\frac{P}{2}\frac{\pi}{S_s}\right) - \frac{\alpha_3^*}{3}\sin\left(\frac{3P}{2}\phi_{ss,y}\right)\sin\left(\frac{3P}{2}\frac{\pi}{S_s}\right)\right)\right) \tag{3.48}$$

The function round(.) rounds its argument to the nearest integer. Using (8.1-22) from [28] and (3.46), the effective values of N_{s1} and α_3 are derived in terms of $N_{as,\text{y}}$ and given by

$$N_{s1} = \frac{1}{\pi}\sum_{y=1}^{S_s} N_{as,y}\sin\left(\frac{P}{2}\phi_{ss,y}\right) \tag{3.49}$$

$$\alpha_3 = \frac{-1}{\pi N_{s1}}\sum_{y=1}^{S_s} N_{as,y}\sin\left(\frac{3P}{2}\phi_{ss,y}\right) \tag{3.50}$$

The difference between N_{s1}^*, α_3^*, and N_{s1}, α_3, results from rounding operations when converting from continuous representation of a conductor distribution to a discrete conductor distribution. The total number of conductors in each slot is found by summing the absolute value of (3.46)-(3.48) as shown below

$$N_{s,y} = \left|N_{as,y}\right| + \left|N_{bs,y}\right| + \left|N_{cs,y}\right| \tag{3.51}$$

Conductors parallel to the machine end surfaces are referred to as end conductors. Knowledge of the distribution of these conductors is necessary to accurately calculate conductor losses. Following the procedure described in [28] Section 9.4, the discrete end conductor density for phase winding x is given by

$$M_{x,y} = M_{x,y-1} + N_{x,y-1} \tag{3.52}$$

where

$$M_{x,1} = -\frac{1}{2}\sum_{y=1}^{S_s/P} N_{x,y} \tag{3.53}$$

Note that if a non-integer value was obtained from evaluation of (3.53), minor alterations can be done to the end conductor arrangement so that a proper connectivity with an integer number of conductors is obtained.

An important concept in distributed windings is the winding function. Using (8.2-11) from reference [28], the continuous winding function for the conductor density distribution (3.42)-(3.44) is given as

$$\mathrm{w}_{as}\left(\phi_{sm}\right) = \frac{2N_{s1}}{P}\left(\cos\left(\frac{P}{2}\phi_{sm}\right) - \frac{\alpha_3}{3}\cos\left(\frac{3P}{2}\phi_{sm}\right)\right) \tag{3.54}$$

$$\mathrm{w}_{bs}\left(\phi_{sm}\right) = \frac{2N_{s1}}{P}\left(\cos\left(\frac{P}{2}\phi_{sm} - \frac{2\pi}{3}\right) - \frac{\alpha_3}{3}\cos\left(\frac{3P}{2}\phi_{sm}\right)\right) \tag{3.55}$$

$$\mathrm{w}_{cs}\left(\phi_{sm}\right) = \frac{2N_{s1}}{P}\left(\cos\left(\frac{P}{2}\phi_{sm} + \frac{2\pi}{3}\right) - \frac{\alpha_3}{3}\cos\left(\frac{3P}{2}\phi_{sm}\right)\right) \tag{3.56}$$

The winding function will be used to find the air gap Magneto-Motive Force (MMF) distribution.

In addition to the distribution of conductors, the stator conductors cross sectional area and diameter are needed to evaluate the machine's efficiency. The conductor cross sectional area and the slot packing factor are related by the following expression.

$$k_{pf} = \frac{\max\left(\mathbf{N}_s\right)a_c}{a_{slt}} \tag{3.57}$$

where k_{pf} is the packing factor, $\mathbf{N}_s$ is a vector of total number of conductors in each slot calculated using (3.51), a_c is the conductor cross sectional area and a_{slt} is the slot area calculated using (3.28). Note that the maximum of $\mathbf{N}_s$ is taken to calculate the maximum packing factor in all slots. Rearranging (3.57) for the conductor cross sectional area gives

$$a_c = \frac{k_{pf}\, a_{slt}}{\max\left(\mathbf{N}_s\right)} \tag{3.58}$$

The conductor diameter is found from a_c

$$d_c = \sqrt{\frac{4a_c}{\pi}} \tag{3.59}$$

The depth of the winding within the slot in the rectangular slot approximation shown in Fig. 3.4 can now be readily expressed as

$$d_{wR} = \frac{\max\left(\mathbf{N}_s\right) a_c}{k_{pf} w_{siR}} \tag{3.60}$$

Another variable of interest is the length of the end winding bundle in the axial direction. This dimension is approximated as

$$l_{ew} = \frac{\max\left(\left|M_{as}\right| + \left|M_{bs}\right| + \left|M_{cs}\right|\right)}{k_{pf} d_{wR}} \tag{3.61}$$

Finally, the volume of the of stator conductor per phase, v_{cd}, is equal to [28]

$$v_{cd} = \left(l + 2l_{eo}\right) a_c \sum_{y=1}^{S_s} \left|N_{as,y}\right| + \frac{2\pi}{S_s}\left(r_{st} + r_{sb}\right) a_c \sum_{y=1}^{S_s} \left|M_{as,y}\right| \tag{3.62}$$

where l_{eo} is the end winding offset which amounts to the overhang in end winding between the end of the stator lamination stack and the end winding bundle. It is desirable to make l_{eo} as small as possible but that comes at the expense of increasing the leakage inductance and core loss somewhat.

3.3 Material Parameters

The type of material used to build the machine strongly affects its performance. From an electro-magnetical perspective, four regions in the machine require a careful decision on the choice of material chosen. These are the stator, rotor, permanent magnet and the winding conductors.

In this section a mapping is created between integer valued variables s_t, r_t, c_t and m_t and the stator, rotor, permanent magnet and winding conductors material, respectively. Each parameter represents a specific material that is summarized with its properties in a predetermined materials library or catalog. The mapping can be represented mathematically as

$$\mathbf{S} = F_{sc}\left(s_t\right) \tag{3.63}$$

$$\mathbf{R} = F_{sc}\left(r_t\right) \tag{3.64}$$

$$\mathbf{M} = F_{mc}\left(m_t\right) \tag{3.65}$$

$$\mathbf{C} = F_{cc}\left(c_t\right) \tag{3.66}$$

where subscripts sc, mc and cc denote the steel, magnet and conductor catalogs respectively, and where $\mathbf{S}, \mathbf{R}$, $\mathbf{M}$ and $\mathbf{C}$ are vectors containing the chosen material physical parameters for the stator laminations, rotor laminations, permanent magnet and winding conductors, respectively. These physical parameters are

$$\mathbf{S} = \left[\rho_s \;\; c_s \;\; B_{s,lim1} \;\; B_{s,lim2} \;\; k_h \;\; k_e \;\; \alpha \;\; \beta\right]^T \tag{3.67}$$

$$\mathbf{R} = \left[\rho_r \;\; c_r \;\; B_{r,lim1}\right]^T \tag{3.68}$$

$$\mathbf{M} = \left[\rho_m \;\; c_m \;\; B_r \;\; \chi_m \;\; H_{ci}\right]^T \tag{3.69}$$

$$\mathbf{C} = \left[\rho_c \;\; c_c \;\; \sigma_c \;\; J_{lim}\right]^T \tag{3.70}$$

where ρ_s, ρ_r, ρ_m and ρ_c are the mass density of the stator, rotor, magnet and conductor materials respectively and c_s, c_r, c_m and c_c are the cost density in \$/kg of the stator, rotor, permanent magnet and conductor materials respectively. The cost density of the steel laminations and winding conductors were estimated using available market price. The cost of permanent magnets was obtained from [40].

There are two recommended upper limit flux density values used to avoid magnetic saturation in the stator lamination denoted by $B_{s,lim1}$ and $B_{s,lim2}$, and one in the rotor lamination denoted by or $B_{r,lim1}$. The recommended flux density with subscript 1 corresponds to a relative absolute permeability of 1000 while the flux density with subscript 2 corresponds to a relative absolute permeability of 100. As discussed later in this chapter, the stator tooth magnetic saturation is modeled in the air gap flux density derivation. However, although saturation is modeled therein, it was found that it is advantageous from a computational convergence perspective to limit the peak tooth flux density. In this case, the flux density corresponding to a relative absolute permeability of 100 is used as an upper limit.

Core loss is calculated only in the stator laminations. With a sinusoidal distribution of MMF, core loss in rotor laminations or magnets can be ignored since no significant harmonic contents are present in the air gap flux density waveform. To calculate core loss, the Modified Steinmetz Equation (MSE) is used [33]. The MSE parameters are given by k_h, k_e, α and β. More on core loss calculation is discussed in Section 3.7.

In (3.69) the permanent magnet remnant flux density and linear magnetic susceptibility are denoted as B_r and χ_m while the coercive field intensity of the magnet is denoted as H_{ci}. Finally, in (3.70) the conductivity and the recommended current density upper limit of the conductor are denoted as σ_c and J_{lim}.

Appendices A, B, C and D contain a list of steel, permanent magnet, and conductor material properties for different materials. In the next section, the stator current excitation and control is discussed.

3.4 Stator Current and Control Philosophy

The machine's input is fed from a three phase inverter as shown in Fig 3.7, where a three-phase Y-connection is adopted. Therein, v_{dc} is a dc voltage source which is typically either a three-phase rectifier or a battery, v_{ag}, v_{bg} and v_{cg} are the three-phase line-to-ground voltages, v_{as}, v_{bs} and v_{cs} are the line to neutral voltages and i_{as}, i_{bs} and i_{cs} are the three phase currents. As shown in the figure, a phase leg consists of two transistor/diode combinations. The transistors typically used are the Insulated Gate Bipolar Transistors (IGBTs).

The main function of the inverter for this work is to regulate the three phase current output to the desired value needed to obtain a commanded torque. It will be assumed that the commanded current values are equal to the measured values with no error between them. In terms of *qd* variables, this means that $i_{qs}^{r*} = i_{qs}^{r}$ and $i_{ds}^{r*} = i_{ds}^{r}$.

The rms current and current phase angle are obtained from the *qd* currents as shown below [28]

$$I_s = \frac{1}{\sqrt{2}}\sqrt{\left(i_{qs}^{r*}\right)^2 + \left(i_{ds}^{r*}\right)^2} \tag{3.71}$$

$$\phi_i = \text{angle}\left(i_{qs}^{r*} - j\, i_{ds}^{r*}\right) \tag{3.72}$$

Thus, the *abc* currents are given as

$$\mathrm{i}_{as}\left(\theta_{rm}\right) = \sqrt{2}\, I_s \cos\left(\frac{P}{2}\theta_{rm} + \phi_i\right) \tag{3.73}$$

$$\mathrm{i}_{bs}\left(\theta_{rm}\right) = \sqrt{2}\, I_s \cos\left(\frac{P}{2}\theta_{rm} + \phi_i - \frac{2\pi}{3}\right) \tag{3.74}$$

$$\mathrm{i}_{cs}\left(\theta_{rm}\right) = \sqrt{2}\, I_s \cos\left(\frac{P}{2}\theta_{rm} + \phi_i + \frac{2\pi}{3}\right) \tag{3.75}$$

Note that the currents are a function of the rotor angle. The rotor position is typically obtained via sensors placed inside the machine. Another method to obtain the rotor position is through sensorless control mechanisms [34]. Note that for magneto-static analysis, rotor position is fixed and therefore (3.73)-(3.75) reduce to constant values.

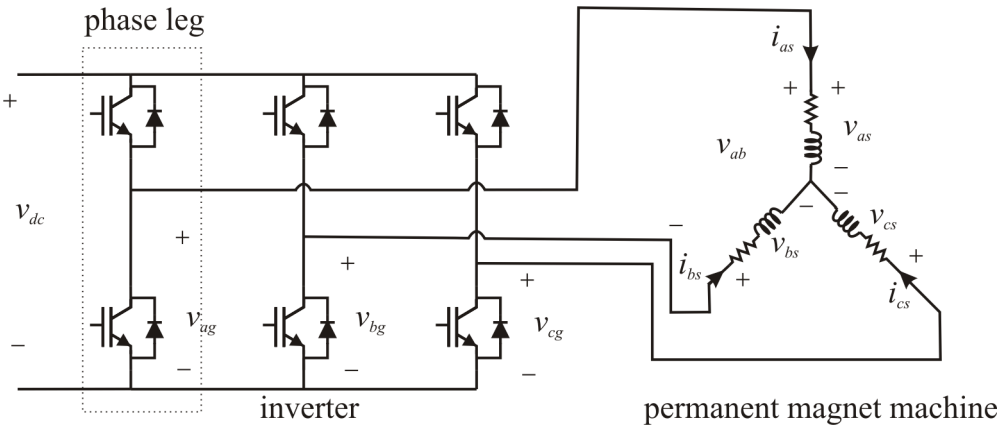

Fig. 3.5. Three phase inverter connected to the input of the machine

There are three more details that need to be addressed that are related to the machine electrical drive. First is the maximum line-to-line voltage that can be achieved, which constrained by the available dc power supply voltage v_{dc} and the forward voltage semiconductor switch drop v_{fs}. As shown in [28], the maximum line-to-line voltage that can be outputted is equal to

$$v_{llmx} = v_{dc} - 2v_{fs} \tag{3.76}$$

In (3.76), it is assumed that the forward voltage drop of the IGBT and the diode are equal and denoted by v_{fs}. The second point that should be considered is the average semiconductor switch conduction power loss, which can be shown to be equal to [28]

$$P_s = \frac{6\sqrt{2}}{\pi} v_{fs} I_s \tag{3.77}$$

More information on the switch conduction loss model can be found in [19]. Finally, the machine's dc conduction loss is equal to

$$P_r = \frac{3}{2} R_s I_s^2 \tag{3.78}$$

3.5 Radial Field Analysis

The magnetic analysis of the machine is conducted using an analytical radial field analysis. A number of assumptions are first made. The magneto-motive force (MMF drop) across steel is neglected except in the stator teeth. Second, the flux density in the permanent magnet and air gap only has a radial component. Third, linear magnetic properties are assumed in rotor teeth with a fixed susceptibility. Finally, temperature effects are neglected.

With these assumptions taken into account, the order of this section is as follows. First the MMF in the permanent magnet and air gap region is derived. Then, the radial flux density expression as a function of radius and angular position in the permanent magnet and air gap is formulated. This relationship in particular is important since it permits finding the flux density in different locations across of the machine.

From the knowledge of the winding functions and the three phase currents, the

spatial distribution of the MMF can be obtained. It can be shown that the stator MMF is given by the dot product between the winding function vector and the three phase currents vector [28]

$$\mathrm{F}_s\left(\theta_{rm},\phi_{sm}\right)=\mathrm{i}_{as}\left(\theta_{rm}\right)\mathrm{w}_{as}\left(\phi_{sm}\right)+\mathrm{i}_{bs}\left(\theta_{rm}\right)\mathrm{w}_{bs}\left(\phi_{sm}\right)+\mathrm{i}_{cs}\left(\theta_{rm}\right)\mathrm{w}_{cs}\left(\phi_{sm}\right) \tag{3.79}$$

Substituting (3.54)-(3.56) and (3.73)-(3.75) into (3.83) yields

$$\mathrm{F}_s\left(\theta_{rm},\phi_{sm}\right)=\frac{3\sqrt{2}}{P}I_s N_{s1}\cos\left(\frac{P}{2}\left(\phi_{sm}-\theta_{rm}\right)-\phi_i\right) \tag{3.80}$$

Equation (3.84) shows that the MMF sinusoidally varies and rotates with the rotor at a speed proportional to the mechanical rotor speed.

It will be convenient to express the MMF in terms of *qd* variables. This can be done by taking advantage of the relationship between the *qd* currents in the rotor frame of reference, the rms current I_s and current phase angle ϕ_i. The MMF in *qd* variables may be expressed as

$$\mathrm{F}_s\left(\theta_{rm},\phi_{sm}\right)=\frac{3N_{s1}}{P}\left[\cos\left(\frac{P}{2}\left(\phi_{sm}-\theta_{rm}\right)\right)\quad -\sin\left(\frac{P}{2}\left(\phi_{sm}-\theta_{rm}\right)\right)\right]\begin{bmatrix} i_{qs}^r \\ i_{ds}^r \end{bmatrix} \tag{3.81}$$

The stator MMF is equal to the sum MMF drops from the rotor back iron to the stator teeth. Thus

$$\mathrm{F}_s\left(\theta_{rm},\phi_{sm}\right)=\int_{r_{rb}}^{\mathrm{r}_{rg}\left(\phi_{rm}\right)}\mathrm{H}\left(r,\phi_{sm}\right)\bullet d\vec{l}+\int_{\mathrm{r}_{rg}\left(\phi_{rm}\right)}^{r_{st}}\mathrm{H}\left(r,\phi_{sm}\right)\bullet d\vec{l}+\int_{r_{st}}^{r_{st}+d_{tb}}\mathrm{H}_t\left(\phi_{sm}\right)\bullet d\vec{l} \tag{3.82}$$

where $\mathrm{H}\left(r,\phi_{sm}\right)$ is the radial field intensity between $r_{rb}\le r\le r_{st}$ and $\mathrm{H}_t\left(\phi_{sm}\right)$ is the field intensity in the stator tooth. The first term on the RHS accounts for the MMF drop across the permanent magnet-rotor tooth region, the second term is the MMF drop across the air gap while the third term is due to the MMF drop across the stator teeth. In order to evaluate (3.82), expressions for the field intensities in each region are needed. These expressions are next derived for one magnetic pole.

Fig. 3.6 shows a thin sector of the machine. Therein, Φ_r denotes the radial magnetic flux flowing from the rotor to the stator through an imaginary surface at an

arbitrary radius r. The flux flowing out of the imaginary surface towards a stator tooth is denoted by Φ_{st}. Applying gauss law at the boundary, the radial flux density can be shown to be equal to

$$\mathrm{B}\left(r,\phi_{sm}\right)=\frac{r_{st}}{r}\mathrm{B}_{st}\left(\phi_{sm}\right),\quad r_{rb}\le r\le r_{st} \tag{3.83}$$

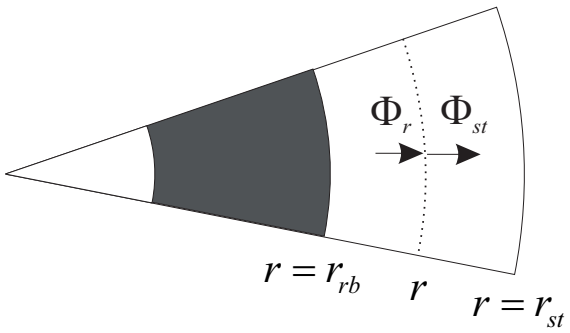

Fig. 3.6. Thin sector of machine

The flux density in the permanent magnet-rotor tooth region can be linearly expressed as a function of the field intensity. This relationship is given by

$$\mathrm{B}\left(r,\phi_{sm}\right)=\mu_0\mu_{rm}\left(\phi_{rm}\right)\mathrm{H}\left(r,\phi_{sm}\right)+\mathrm{B}_m\left(\phi_{rm}\right),\quad r_{rb}\le r\le \mathrm{r}_{rg}\left(\phi_{rm}\right) \tag{3.84}$$

where μ_0 is the permeability of the vacuum, $\mu_{rm}\left(\phi_{rm}\right)$ is the permanent magnet-rotor tooth relative permeability as function of angular position, $\mathrm{H}\left(r,\phi_{sm}\right)$ is the field intensity, and $\mathrm{B}_m\left(\phi_{rm}\right)$ is the residual flux density in the tooth and permanent magnet as a function of angular position.

From Fig. 3.3, the residual flux density function is expressed as

$$\mathrm{B}_m\left(\phi_{rm}\right)=\begin{cases}\left(-1\right)^i B_r & \phi_{pt1,i}\le\phi_{rm}\le\phi_{pt2k,i}\\ 0 & \phi_{pt2k,i}\le\phi_{rm}\le\phi_{pt2,i}\\ 0 & \phi_{pt2,i}\le\phi_{rm}\le\phi_{pt3,i}\\ 0 & \phi_{pt3,i}\le\phi_{rm}\le\phi_{pt4,i}\end{cases} \tag{3.85}$$

where B_r is the PM residual flux density. Note that the permanent magnet polarity changes for every consecutive pole, were the pole number is denoted by i. The permeability function is expressed as

$$\mu_{rm}\left(\phi_{rm}\right)=\begin{cases}1+\chi_m & \phi_{pt1,i}\le\phi_{rm}\le\phi_{pt2k,i}\\ 1 & \phi_{pt2k,i}\le\phi_{rm}\le\phi_{pt2,i}\\ 1+\chi_{rt} & \phi_{pt2,i}\le\phi_{rm}\le\phi_{pt3,i}\\ 1 & \phi_{pt3,i}\le\phi_{rm}\le\phi_{pt4,i}\end{cases} \tag{3.86}$$

where χ_{rt} is the susceptibility of the rotor tooth steel and χ_m is PM magnetic susceptibility.

In the air gap separating the rotor and permanent magnet from the stator $\mathrm{r}_{rg}\left(\phi_{rm}\right)\le r\le r_{st}$, the flux density is given as

$$\mathrm{B}\left(r,\phi_{sm}\right)=\mu_0\mathrm{H}\left(r,\phi_{sm}\right),\quad \mathrm{r}_{rg}\left(\phi_{rm}\right)\le r\le r_{st} \tag{3.87}$$

To compute the flux density flowing in the stator tooth, all the flux from the air gap within one span of a slot and tooth converges into the tooth as shown in Fig. 3.8. Therein, Φ_{st} is the air gap slot/tooth flux and Φ_t is the flux flowing inside the stator tooth for a generic tooth.

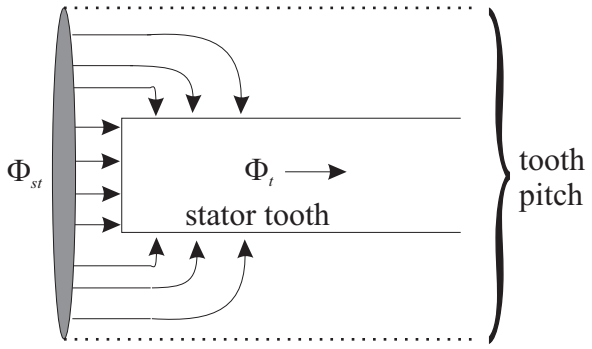

Fig. 3.7. Magnetic flux flow into a stator tooth

By Gauss's law

$$\Phi_{st} = \Phi_t \tag{3.88}$$

Assuming a uniform flux density, (3.88) can be simplified to

$$\mathrm{B}_t\left(\phi_{sm}\right) = \frac{2\pi r_{st}}{w_{tb} S_s}\mathrm{B}_{st}\left(\phi_{sm}\right) \tag{3.89}$$

where $\mathrm{B}_t\left(\phi_{sm}\right)$ is the tooth flux density. The tooth flux density can be expressed in terms of the field intensity as

$$\mathrm{B}_t\left(\phi_{sm}\right) = \mu_B\left(\mathrm{B}_t\left(\phi_{sm}\right)\right)\mathrm{H}_t\left(\phi_{sm}\right) \tag{3.90}$$

where $\mu_B\left(\mathrm{B}_t\left(\phi_{sm}\right)\right)$ is the steel permeability as a function of flux density. Details on this function can be found in [35]. Note that (3.90) is approximate since it does not account for hysteresis.

Resolving (3.84), (3.87) and (3.90) for the field intensities and then substituting into (3.82)

$$\begin{aligned}\mathrm{F}_s\left(\phi_{sm}\right) = &\int_{r_{rb}}^{\mathrm{r}_{rg}\left(\phi_{rm}\right)} \frac{\mathrm{B}\left(r,\phi_{sm}\right) - \mathrm{B}_m\left(\phi_{rm}\right)}{\mu_0\mu_{rm}\left(\phi_{rm}\right)} \bullet d\vec{l} + \int_{\mathrm{r}_{rg}\left(\phi_{rm}\right)}^{r_{st}} \frac{\mathrm{B}\left(r,\phi_{sm}\right)}{\mu_0} \bullet d\vec{l} \\ &+ \int_{r_{st}}^{r_{st}+d_{tb}} \frac{\mathrm{B}_t\left(\phi_{sm}\right)}{\mu_B\left(\mathrm{B}_t\left(\phi_{sm}\right)\right)} \bullet d\vec{l}\end{aligned} \tag{3.91}$$

Since a radial field is assumed, $d\vec{l} = dr$. By means of (3.83) and (3.89), evaluating (3.91) yields

$$\begin{aligned}\mathrm{F}_s\left(\theta_{rm},\phi_{sm}\right) = &\mathrm{R}_{pm}\left(\phi_{rm}\right)\mathrm{B}_{st}\left(\phi_{sm}\right) - \mathrm{F}_{pm}\left(\phi_{rm}\right) + \mathrm{R}_g\left(\phi_{rm}\right)\mathrm{B}_{st}\left(\phi_{sm}\right) \\ &+ \frac{z}{\mu_B\left(z\,\mathrm{B}_{st}\left(\phi_{sm}\right)\right)} d_{tb}\mathrm{B}_{st}\left(\phi_{sm}\right)\end{aligned} \tag{3.92}$$

where

$$\mathrm{F}_{pm}\left(\phi_{rm}\right)=\frac{\mathrm{B}_{m}\left(\phi_{rm}\right)}{\mu_{0}\mu_{rm}\left(\phi_{rm}\right)}\left(\mathrm{r}_{rg}\left(\phi_{rm}\right)-r_{rb}\right) \tag{3.93}$$

$$\mathrm{R}_{pm}\left(\phi_{rm}\right)=\frac{r_{st}}{\mu_{0}\mu_{rm}\left(\phi_{rm}\right)}\ln\left(\frac{\mathrm{r}_{rg}\left(\phi_{rm}\right)}{r_{rb}}\right) \tag{3.94}$$

$$\mathrm{R}_{g}\left(\phi_{rm}\right)=\frac{r_{st}}{\mu_{0}}\ln\left(\frac{r_{st}}{r_{st}-\mathrm{g}_{v}\left(\phi_{rm}\right)}\right) \tag{3.95}$$

$$z=\frac{2\pi r_{st}}{w_{tb}S_{s}} \tag{3.96}$$

A Newton-Raphson iteration process is used to solve for the stator tooth flux density $\mathrm{B}_{st}\left(\phi_{sm}\right)$ in (3.92). Knowing the stator tooth flux density, the flux density between $r_{rb}\le r\le r_{st}$ and $0\le\phi_{sm}\le 2\pi$ is found using (3.83). This concludes the radial field analytical analysis. The stage is now set for the next section where the lumped model parameters are derived.

3.6 Lumped Model Parameters

In this section, the *qd* flux linkages and the stator resistance are obtained. Knowing these variables allows calculating the *qd* voltages and electromagnetic torque.

The stator three phase flux linkage equation of the machine expressed in *abc* variables may be expressed as

$$\boldsymbol{\lambda}_{abcs}=\boldsymbol{\lambda}_{abcl}+\boldsymbol{\lambda}_{abcm} \tag{3.97}$$

where $\boldsymbol{\lambda}_{abcl}$ and $\boldsymbol{\lambda}_{abcm}$ are the three phase leakage and magnetizing flux linkages respectively. By definition, stator leakage flux linkage is the flux that does not cross the air gap to the rotor, while the stator magnetizing flux linkage is due to the stator flux that crosses and communicates between the stator and the rotor. Expressing the flux linkages in *qd0* variables instead of *abc* variables is more convenient. Using Park's transformation [10], the flux linkage in *qd0* variables in the rotor frame of reference is given as

$$\boldsymbol{\lambda}^{r}_{qd0s}=\boldsymbol{\lambda}^{r}_{qd0l}+\boldsymbol{\lambda}^{r}_{qd0m} \tag{3.98}$$

For the system configuration considered in this work, the zero sequence does not play any role and therefore will be dropped. Work done in Sections 8.6, 8.7 and 9.8 of [28] shows that the leakage and magnetizing flux linkages in *qd* variables may be expressed as

$$\boldsymbol{\lambda}_{qdl}^{r} = L_{ls}\mathrm{i}_{qds}^{r} \tag{3.99}$$

and

$$\boldsymbol{\lambda}_{qdm}^{r} = lr_{st}\int_{0}^{2\pi}\mathbf{K}_{s}^{r}\left(\theta_{rm}\right)\Big|_{\mathrm{utr}}\mathbf{w}_{abcs}\left(\phi_{sm}\right)\mathrm{B}_{st}\left(\phi_{sm}\right)d\phi_{sm} \tag{3.100}$$

respectively and where,

$$L_{ls} = L_{lp} - L_{lm} \tag{3.101}$$

and

$$\mathbf{K}_{s}^{r}\left(\theta_{rm}\right)\Big|_{\mathrm{utr}} = \frac{2}{3}\begin{bmatrix} \cos\left(\frac{P\theta_{rm}}{2}\right) & \cos\left(\frac{P\theta_{rm}}{2}-\frac{2\pi}{3}\right) & \cos\left(\frac{P\theta_{rm}}{2}+\frac{2\pi}{3}\right) \\ \sin\left(\frac{P\theta_{rm}}{2}\right) & \sin\left(\frac{P\theta_{rm}}{2}-\frac{2\pi}{3}\right) & \sin\left(\frac{P\theta_{rm}}{2}+\frac{2\pi}{3}\right) \end{bmatrix} \tag{3.102}$$

A method to calculate L_{lp} and L_{lm} in equation (3.101) has been presented in Section 8.7 of [28]. In the same chapter of the same reference, Section 8.8 provides a procedure to obtain the stator winding resistance R_s. The focus herein will be directed towards obtaining the magnetizing flux linkages in equation (3.100). Further simplification of (3.100) reveals

$$\lambda_{qm}^{r} = \frac{2lr_{st}N_{s1}}{P}\int_{0}^{2\pi}\cos\left(\frac{P}{2}\phi_{rm}\right)\mathrm{B}_{st}\left(\phi_{sm}\right)d\phi_{rm} \tag{3.103}$$

and

$$\lambda_{dm}^{r} = -\frac{2lr_{st}N_{s1}}{P}\int_{0}^{2\pi}\sin\left(\frac{P}{2}\phi_{rm}\right)\mathrm{B}_{st}\left(\phi_{sm}\right)d\phi_{rm} \tag{3.104}$$

Note that integrating with respect to ϕ_{rm} or ϕ_{sm} gives similar results because the integral is for one complete revolution. The magnetizing flux linkages are calculated by evaluating the integrals in (3.103) and (3.104) numerically.

Next, the steady state *qd* voltage equations are equal to

$$v_{qs}^{r} = r_s i_{qs}^{r} + \omega_r \left(L_{ls} i_{ds}^{r} + \lambda_{dm}^{r} \right) \tag{3.105}$$

and

$$v_{ds}^{r} = r_s i_{ds}^{r} - \omega_r \left(L_{ls} i_{qs}^{r} + \lambda_{qm}^{r} \right) \tag{3.106}$$

where ω_r is the rotor electrical speed which is equal to rotor mechanical speed ω_{rm} multiplied by the number of pole pairs $P/2$.

From the *qd* voltage, the peak line-to-line voltage can be calculated as

$$v_{ll,pk} = \sqrt{3}\sqrt{\left(v_{qs}^{r}\right)^2 + \left(v_{ds}^{r}\right)^2} \tag{3.107}$$

The peak line-to-line voltage will be constrained by the maximum upper limit equation (3.76).

Finally, the torque output of the machine can be calculated using

$$T_e = \frac{3}{2}\frac{P}{2}\left(\lambda_{dm}^{r} i_{qs}^{r} - \lambda_{qm}^{r} i_{ds}^{r} \right) \tag{3.108}$$

In the next section, a ferromagnetic field analysis is discussed.

3.7 Ferromagnetic Field Analysis

The flux density at a number of locations in the machine is needed to evaluate the overall efficiency and to check magnetic saturation condition on the stator and rotor steel. In addition, the field intensity in the permanent magnet should be constrained to avoid demagnetizing the permanent magnets. The ferromagnetic field analysis of the stator tooth and stator back iron regions have been discussed in details in reference [28]. Since there are no substantial differences in the field analysis done therein for SM-PMSM and

the field analysis required for the proposed AS-PMSM, the procedure described therein is adopted and is not presented again in this document.

Using the procedure set forth in [28], the following parameters are obtained

$$\mathbf{F}_D = \left[\mathbf{B}_{t1c}\ \mathbf{B}_{b1s}\ B_{t1mx}\ B_{b1mx}\ B_{rbtmx}\ B_{rbrmx}\ H_{mn}\right]^T \tag{3.109}$$

where $\mathbf{B}_{t1c}$ and $\mathbf{B}_{b1s}$ are the flux density time waveforms over one period in stator tooth 1 and backiron segment 1, respectively. The maximum flux density in stator tooth 1, stator backiron segment 1, tangential component of the rotor back iron and the radial component of the rotor back iron are denoted by B_{t1mx}, B_{b1mx}, B_{rbtmx}, and B_{rbrmx}, respectively. Finally, the minimum permanent magnet field intensity is denoted by H_{mn}. To calculate the tooth flux density time waveform, special attention was made for material transition points when carrying out the integrals shown in (9.9-1) in [28].

The core loss in the stator tooth and back iron is calculated using an empirical loss model known as the Modified Steinmetz Equation [33]. The model breaks the total core loss into two components, hysteresis loss and eddy current loss, as shown below

$$p = k_h\, f_{eq}^{\alpha-1} B_{mx}^{\beta} f + f\, k_e \int_0^T \left(\frac{dB}{dt}\right)^2 dt \tag{3.110}$$

where p is the power loss per volume, B_{mx} is the maximum flux density over the time domain, $\frac{dB}{dt}$ is the time derivative of the flux density waveform over one period, and $f = \frac{4\pi}{P}\omega_{rm}$ is the fundamental electrical frequency. The equivalent frequency, f_{eq}, is defined as

$$f_{eq} = \frac{2}{\Delta B^2 \pi^2} \int_0^T \left(\frac{dB}{dt}\right)^2 dt \tag{3.111}$$

where ΔB is the peak to peak flux density. The equivalent frequency accounts for a non-sinusoidal flux density waveform. The MSE parameters k_h, α, β and k_e are model parameters found using magnetic material characterization methods [36]. Appendix D gives these parameters for steel materials used in this work. Note that the units of k_h and k_e indicate that the power loss per volume is calculated in W/m^3.

Denoting the power loss density in the stator tooth and stator back iron by p_{ct} and p_{cb}, the core loss is equal to

$$P_c = p_{ct} v_{st} + p_{cb} v_{sb} \tag{3.112}$$

3.8 AC Losses

The last step is to include ac losses into the total loss calculation. Two ac losses are considered: skin effect loss and proximity effect loss. The procedure described here is discussed in details in [28].

The first step in calculating skin effect losses is to find the dc and ac resistance associated with a single phase of the winding. The dc resistance is given by

$$r_{dc,s} = \frac{\frac{v_{cd}}{a_c}\sum_{i=1}^{S_s}\left|N_{as,\mathrm{i}}\right|}{\pi r_c^2 \sigma_c} \tag{3.113}$$

The ac resistance is equal to

$$r_{ac,s} = -\mathrm{real}\left(\frac{\frac{v_{cd}}{a_c}\sum_{i=1}^{S_s}\left|N_{as,\mathrm{i}}\right| \mathrm{J}_B\left(r_c/\kappa\right)}{2\pi r_c \kappa \sigma_c \mathrm{J}'_B\left(r_c/\kappa\right)}\right) \tag{3.114}$$

where function 'real' returns the real component of its argument, J_B is the Bessel function of the first kind and zero order, J'_B is the derivative of the Bessel function of the first kind and zero order (i.e.: the Bessel function of the first kind and first order). Constant κ is equal to

$$\kappa = \sqrt{\frac{j}{\omega_r \sigma_c \mu_0}} \tag{3.115}$$

where j is the imaginary number and ω_r is the electrical rotor speed in rad/sec. The skin effect ac losses are given by the difference between ohmic losses due to dc resistance and ohmic losses due to ac resistance. This is expressed

$$P_{skin} = 3I_s^2 \left(r_{ac,s} - r_{dc,s} \right) \tag{3.116}$$

To calculate proximity losses, it is assumed that only two phases exist in one slot at maximum. Using subscripts *x* and *y* to denote the phases occupying stator slot 1, the proximity effect losses of the machine are given by

$$P_{prox} = \frac{\pi \sigma_c l r_c^4 \omega_r^2 \mu_0^2 S_s}{12 w_{siR}^2} I_s^2 \left(\left| N_{xs,1} \right| + \left| N_{ys,1} \right| \right) \left(N_{xs,1}^2 - N_{xs,1} N_{ys,1} + N_{ys,1}^2 \right) \tag{3.117}$$

This chapter presented the analysis procedure of an AS-PMSM, where a treatment of the machine's overall geometrical, electrical and magnetical aspects has been applied. This procedure is utilized in the next chapter to design the machine using a population based optimization algorithm. The design results are then used to compare the AS-PMSM to a SM-PMSM designed under the same design specifications.

4. MULTI OBJECTIVE DESIGN OF AN ASYMETRICAL SALIENT PERMANENT MAGNET SYNCHRONOUS MACHINE

This chapter presents the design results of an asymmetrical salient PMSM using a multi-objective optimization approach. The optimization algorithm used herein the Genetic Algorithm (GA) [31]. The population size and number of generation are both set equal to 3000 in all studies presented in this chapter.

In Section 4.1, the formulation of the design problem is presented. Therein, the design space, design parameters and design objectives are defined. Section 4.2 lists the design constraints. These constraints are added to ensure that sensible machine designs obtained and to enhance the convergence of the optimization algorithm. In Section 4.3, the convergence of the optimization algorithm is confirmed by comparing the results obtained from several runs and making sure that they are consistent. Section 4.4 compares the design results of AS-PMSM and SM-PMSM. The AS-PMSM design results are then further analyzed and discussed.

4.1 Formulation of Design Problem

The design problem specifications are listed in Table 4.1. Most of the parameters listed therein have been defined and discussed in Chapter 3. A fraction $k_m = 0.75$ sets the limit on the minimum permanent magnet field intensity allowed to avoid demagnetization of the permanent magnet. The procedure described in [28] and referred to Section 3.7 varies the rotor position by a specific amount in order to obtain the flux density time waveforms. The number of rotor positions considered is equal to *J*. Parameters α_{tar} and α_{so} set the stator tooth aspect ratio (d_{tb} / w_{tb}) and stator slot opening (w_{so} / d_c), respectively. The rotor tooth is assumed to operate in the linear magnetic region, with a constant susceptibility $\chi_{rt} = 7000$ (check (3.86)). To enhance the computational efficiency, the design space is reduced by applying upper limits on the electromagnetic mass and total weighted power loss M_{emmx} and P_{lmx} respectively.

The design targets a CPSR of 5:1. Three operating points are studied starting from a speed of 1000 rpm and reaching to a maximum speed of 5000 rpm, resulting in a

TABLE 4.1
Design Specifications

Parameter	Value	Units	Parameter	Value	Units
v_{dc}	400	V	M_{emmx}	14	kg
n_{spp}	2	N/A	P_{lmx}	500	W
k_m	0.75	N/A	α_{tar}	10	N/A
k_{pf}	0.5	N/A	α_{so}	1.5	N/A
l_{eo}	1	cm	$\boldsymbol{\omega}_{rm}$	[1000, 2236, 5000]	rpm
r_{rs}	2	cm	$\mathbf{T}_e^*$	[17.8, 7.96, 3.56]	Nm
v_{fs}	2	V	$\mathbf{P}_{out}^*$	[1.86, 1.86, 1.86]	kW
J	80	N/A	$\mathbf{w}_1$	[0.333, 0.334, 0.333]	N/A
$\phi_{ss,1}$	π / S_s	rad	$\mathbf{w}_2$	[0.7, 0.2, 0.1]	N/A
χ_{rt}	7000	N/A	$\mathbf{w}_3$	[0.1, 0.2, 0.7]	N/A

constant output power equal to 1.86 kW or 2.5 hp. To analyze each operating point, a subset of the complete analysis presented in Chapter 3 is repeated. In particular, Sections 3.4 through 3.8, which depend on the operating point characteristics (speed and *qd* currents), are analyzed separately for each operating point.

A total of 25 design parameters make up the design space. The design space may be represented by a vector $\boldsymbol{\theta}$ given as

$$\boldsymbol{\theta} = [s_t \; r_t \; c_t \; m_t \; P_p \; d_i \; d_{rb} \; d_m \; g \; d_{tb} \; \alpha_t \; d_{sb} \; \alpha_{pm} \; l \; N_{s1}^* \; \alpha_3^* \; \alpha_{rt} \; g_{rt}^* \; i_{qs,1}^r \; i_{ds,1}^r \; i_{qs,2}^r \; i_{ds,2}^r \; i_{qs,3}^r \; i_{ds,3}^r \; \alpha_{tap}]^T \tag{4.1}$$

The design space parameters are listed in Table 4.2 with their maximum and minimum limits shown. Entries in the encoding column states whether each variable is represented in the GA as a continuous linear mapping (Lin), a continuous logarithmic mapping (Log), or a discrete integer mapping (Int) [28]. The type of stator and rotor steel and conductor parameters, s_t, r_t and c_t are fixed at a constant value equal to 1. This enforces the design algorithm to consider only one type of steel and one type of conductor materials. As shown in Appendices A and C, these materials are M19 steel and copper. These parameters were included in the design space and not as constants to facilitate including different materials into the design space in future work.

TABLE 4.2
Parameters Range

Parameter	Min.	Max.	Encoding	Units	Parameter	Min.	Max.	Encoding	Units
s_t	1	1	Int	N/A	l	1	50	Log	cm
r_t	1	1	Int	N/A	N_{s1}^{*}	10	1000	Log	cond./rad
c_t	1	1	Int	N/A	α_3^{*}	0.1	0.7	Lin	N/A
m_t	1	7	Int	N/A	α_{rt}	0.1	1.0	Lin	N/A
P_p	4	6	Int	N/A	g_{rt}^{*}	0.5	2.0	Lin	mm
d_i	0.1	10	Log	cm	$i_{qs,1}^{r}$	0.1	100	Log	A
d_{rb}	0.1	5.0	Log	cm	$i_{ds,1}^{r}$	-30	0.0	Lin	A
d_m	0.1	5.0	Log	cm	$i_{qs,2}^{r}$	0.1	100	Log	A
g	0.5	2.0	Lin	mm	$i_{ds,2}^{r}$	-30	0.0	Lin	A
d_{tb}	0.1	5.0	Log	cm	$i_{qs,3}^{r}$	0.1	100	Log	A
α_t	0.05	0.95	Lin	N/A	$i_{ds,3}^{r}$	-30	0.0	Lin	A
d_{sb}	0.1	5.0	Log	cm	α_{tap}	0.0	1.0	Lin	N/A
α_{pm}	0.4	0.9	Lin	N/A					

This section defined the design specification and design parameters for the design problem investigated in this chapter. The next section presents the design constraints and fitness functions.

4.2 Design Constraints and Fitness Functions

Various constraints are imposed to ensure a proper and sensible machine designs are achieved. These constraints shape the machine design topology from several aspects such as geometry and electromagnetical behavior. The machine's thermal performance is not considered herein but is a part of planned future work. Also note that constraints related to the mechanical performance (e.g. : stresses on the permanent magnet) are not included.

There are a total of 17 constraints imposed on the optimization design problem. To impose those constraints, the 'less than' and 'greater than' functions defined in Chapter 2, Section 2.2, are used.

The first constraint ensures a reasonable stator teeth depth/width ratio, such that a skinny tooth is avoided. Thus, the constraint is

$$c_1 = \text{ltn}\left(d_{tb}, \alpha_{tar} w_{tb}\right) \tag{4.2}$$

where α_{tar} is the tooth aspect ratio chosen by the machine designer. In order to make the machine easier to wind, the conductor diameter which was found in (3.59) , multiplied by the slot opening factor α_{so} , must be less than the width of the slot opening w_{so} ,

$$c_2 = \text{ltn}\left(d_c \alpha_{so}, w_{so}\right) \tag{4.3}$$

In order to limit the search space, a constraint on the maximum allowed electromagnetic mass is added. The electromagnetic mass is given by the sum of the rotor laminations, stator lamination, permanent magnets and stator winding. This is given as

$$M_{em} = \rho_s v_{sl} + \rho_r v_{rl} + \rho_m v_{pm} + 3\rho_c v_{cd} \tag{4.4}$$

where v_{sl}, v_{rl} and v_{pm} are the volumes stator laminations, rotor laminations, and permanent magnets given in Section 3.1, while v_{cd} is the volume of stator conductors per phase given in Section 3.2. The respective mass per volume densities ρ_s, ρ_r, ρ_m and ρ_c are given in Appendices A-C. The constraints on the electromagnetic mass is expressed as

$$c_3 = \text{ltn}\left(M_{em}, M_{emmx}\right) \tag{4.5}$$

A number of magnetic constraints are applied to make sure that magnetic saturation is avoided at specific locations and to avoid demagnetization of the permanent magnet. These conditions are checked in the case when no current is applied (zero excitation) and in the case when current excitation is applied. To distinguish between non-excited and a excited constraints, an additional subscript '*nc*' is added to denote no current conditions: $B_{t1mx,nc}$, $B_{b1mx,nc}$, $B_{rbtmx,nc}$, $B_{rbrmx,nc}$ and $H_{mn,nc}$. Thus, the following constraints when no excitation is applied are imposed

$$c_4 = \text{ltn}\left(B_{t1mx,nc}, B_{s,lim2}\right) \tag{4.6}$$

$$c_5 = \text{ltn}\left(B_{b1mx,nc}, B_{s,lim1}\right) \tag{4.7}$$

$$c_6 = \text{ltn}\left(B_{rbtmx,nc}, B_{r,lim1}\right) \tag{4.8}$$

$$c_7 = \text{ltn}\left(B_{rbrmx,nc}, B_{r,lim1}\right) \tag{4.9}$$

$$c_8 = \text{gtn}\left(H_{mn,nc}, H_{lim}\right) \tag{4.10}$$

where the limits $B_{s,lim2}$, $B_{s,lim1}$ and $B_{r,lim1}$ are given in the steel and magnet appendices. The limit on the permanent magnet field intensity, H_{lim}, is given as

$$H_{lim} = k_m H_{ci} \tag{4.11}$$

where k_m is given in the design specifications Table 4.1 and H_{ci} is given in permanent magnets appendix.

Two constraints are applied to the electrical system. First, the current density should not exceed an allowed maximum value the conductor material is able to handle J_{lim}. This constraint is expressed as

$$c_9 = \text{ltn}\left(I_s / a_c, J_{lim}\right) \tag{4.12}$$

The second electrical constraint is applied to limit the peak line-to-line voltage, given in Section 3.6 equation (3.107), to ensure that the dc power supply capabilities are not exceeded. Hence,

$$c_{10} = \text{ltn}\left(v_{ll,pk}, v_{llmx}\right) \tag{4.13}$$

When an electrical excitation is applied, the following magnetical constraints are imposed

$$c_{11} = \text{ltn}\left(B_{t1mx}, B_{s,lim2}\right) \tag{4.14}$$

$$c_{12} = \text{ltn}\left(B_{b1mx}, B_{s,lim1}\right) \tag{4.15}$$

$$c_{13} = \text{ltn}\left(B_{rbtmx}, B_{r,lim1}\right) \tag{4.16}$$

$$c_{14} = \text{ltn}\left(B_{rbrmx}, B_{r,lim1}\right) \tag{4.17}$$

$$c_{15} = \text{gtn}\left(H_{mn}, H_{lim}\right) \tag{4.18}$$

The machine output torque can be calculated using (3.108). However, the lumped parameter model expression needs to be adjusted by a sufficient amount to account for core loss. The corrected torque is thus given as

$$T_{ec} = T_e - \frac{P_c}{\omega_{rm}} \qquad \omega_{rm} > 0 \tag{4.19}$$

Note that (4.19) should be used only for motor operation. At stall, no core loss exists and therefore $T_{ec} = T_e$.

The next constraint ensures that the corrected torque needs to be greater than the target torque specified in the design specifications. This is expressed as

$$c_{16} = \text{gtn}\left(T_{ec}, T_e^*\right) \tag{4.20}$$

Finally, the last constraint limits the design space by constraining the power loss. The total power loss at an operating point is given by the sum of switch loss, conduction loss, core loss, skin effect and proximity effect loss. This is expressed as

$$P_l = P_s + P_r + P_c + P_{skin} + P_{prox} \tag{4.21}$$

where P_s and P_r are given in Section 3.4, P_c in Section 3.7 and the ac losses in Section 3.8. The last constraint is expressed as

$$c_{17} = \text{ltn}\left(P_l, P_{lmx}\right) \tag{4.22}$$

Constraints c_9 through c_{17} depend on the operating point currents. Therefore, they are evaluated repeatedly for each operating point. This ensures that the machine designs satisfy the requirements expressed by these constraints over the speed range considered.

In this multi-objective optimization design, the two objectives applied are minimizing both the cost of the machine and the total machine losses subject to the constraints imposed. The cost of the machine is modeled as the cost of the materials used in construction and does not account for labor cost or any other expenses. Therefore, the total machine cost is equal to

$$\mathbb{C} = c_s \rho_s v_{sl} + c_r \rho_r v_{rl} + c_m \rho_m v_{pm} + 3c_c \rho_c v_{cd} \tag{4.23}$$

where c_s, c_r, c_m and c_c are the cost per mass in \$/kg of the stator, rotor, permanent magnet and conductor materials. These are given in the material appendices.

The weighted power loss is given by the dot product of the total power loss at all operating points with a weighting vector. This is given as

$$P_{lw} = \mathbf{P}_l \mathbf{w}_x^T \tag{4.24}$$

where $\mathbf{w}_x$ is one of the weighting vectors listed in the design specifications.

The fitness function is evaluated as follows. In the case when all constraints or a predetermined number of constraints are not satisfied then the fitness function is equal to

$$\mathrm{f}(\boldsymbol{\theta}) = \varepsilon \left(\frac{C_S - N_C}{N_C} \right) \begin{bmatrix} 1 \\ 1 \end{bmatrix} \quad C_S < C_I \tag{4.25}$$

else if all constraints have been satisfied then

$$\mathrm{f}(\boldsymbol{\theta}) = \begin{bmatrix} \dfrac{1}{\mathbb{C}} & \dfrac{1}{P_{lw}} \end{bmatrix}^T \quad C_S = N_C \tag{4.26}$$

where C_S, C_I and N_C are the number of constraints satisfied, the number of constraints evaluated, and the total number of constraints, respectively. The variable ε in (4.25) is a very small number (e.g.: 10^{-10}) which decreases the fitness value of designs not passing all constraints. To increase the computational efficiency of the design process, after a predetermined number of constraint evaluation, the code checks if any constraint was not satisfied. If that is the case, the fitness function is equal to (4.25) and the calculation is terminated at an early stage in code.

The pseudo-code showing the steps to determine the design fitness is listed in Tables 4.3 and 4.4. Table 4.3 is the main code used to evaluate the fitness function; Table 4.4 is a code sequence executed at predetermined stages in the design fitness calculation code to check if constraints evaluated at this stage are all satisfied. This check is done after computing c_1- c_3, c_4- c_8, c_9- c_{10}, c_{11}- c_{15} and c_{16}- c_{17}, as described in Table 4.3. The evaluation of constraints c_9- c_{17} is performed repeatedly for every operating point. Thus, for 3 three operating points, the constraint checking algorithm in Table 4.4 is called 12 times.

TABLE 4.3
Fitness Function Calculation Pseudo-Code

1. Initialization, geometrical calculation and material selection
   initialize number of constraints to 17
   calculate machine geometry (Section 3.1) and find material properties (Section 3.3)
   evaluate c_1
2. perform winding calculations
   winding calculations (Section 3.2)
   evaluate c_2
3. mass and cost calculation
   compute total mass and cost using (4.4) and (4.23).
   evaluate c_3
   check constraints c_1 - c_3 (Table 4.4)
4. electrical resistance and leakage inductance calculation
   compute R_s and L_{ls} in using [28]
5. field analysis under no current excitation conditions (Section 3.7)
   evaluate $c_4 - c_8$
   check constraints $c_4 - c_8$ (Table 4.4)
6. initialize total number of operating points $N_{OP} = 3$ and operating point $n_{op} = 1$
7. WHILE n_{op} <= N_{OP} <= 3 AND $C_S = C_I$
   i. current excitation analysis (Section 3.4)
      evaluate c_9
   ii. radial field analysis (Section 3.5)
   iii. lumped model parameters calculation (Section 3.6)
      evaluate c_{10}
      check constraints c_9 - c_{10} (Table 4.4)
   iv. field analysis under operating point excitation conditions (Section 3.7)
      evaluate $c_{11} - c_{15}$
      check constraints $c_{11} - c_{15}$ (Table 4.4)
   vi. calculate corrected torque using (4.19)
      evaluate c_{16}

vii. compute losses
compute total loss using (4.21) and store it in $\mathbf{P}_l$
evaluate c_{17}
check constraints $c_{16} - c_{17}$ (Table 4.4)
viii. update operating point $n_{op} = n_{op} + 1$
ENDWHILE
7. compute weighted power loss P_{lw} using (4.24)
8. evaluate fitness using (4.25)
return

TABLE 4.4
Constraint Fulfillment Pseudo-Code

update C_S
update C_I
IF $(C_S < C_I)$
$$\mathbf{f} = \varepsilon\left(\frac{C_S - N_C}{N_C}\right)\begin{bmatrix}1\\1\end{bmatrix}$$
return
ENDIF

This concludes this section, were the design constraints and fitness function have been defined. In the coming sections, a number of case studies are conducted and their results are presented.

4.3 Case Study 1: Optimization Convergence

The convergence of the optimization is studied and confirmed in this section. One way to confirm convergence is by executing the design problem formulated in Sections 4.1 and 4.2 multiple times and comparing results obtained from each execution. If a close match in results is obtained, then confidence can be built on the convergence of the code.

Perhaps the best way to compare machine design results is by utilizing the Pareto-optimal fronts, which show the tradeoff between competing objectives. The Pareto-

optimal front for the design problem considered in this chapter shows the tradeoff between total weighted loss and cost of the machine designed. It will be used to confirm the convergence of the optimization process.

The applied convergence studies are summarized in Table 4.5. Six sets of studies are performed, where each set contains three sub-sets repeated under the same settings. The first three sets are for a design of a nominal Surface Mount Permanent Magnet Synchronous Machine (SM-PMSM). The last three sets are for a design of an AS-PMSM. The SM-PMSM and AS-PMSM are designed using the three weighting vectors listed in Table 4.1.

The design procedure of a SM-PMSM is presented in Chapter 9 of [28]. However, slight differences between the design procedure presented therein and the designs presented in this work exist. The first difference is that the design presented herein is for a multiple operating speed points. Second, the tooth flux density saturation in this design is taken into account and constrained by $B_{s,lim2}$. Third, the objective functions in these runs are minimizing weighted loss and cost, while the objectives in [28] were minimizing loss and mass. Lastly, the design space vector for the SM-PMSM is structured by 22 parameters instead of 24 and is given by

$$\begin{aligned}\boldsymbol{\theta}_s = [&s_t\ r_t\ c_t\ m_t\ P_p\ d_i\ d_{rb}\ d_m\ g\ d_{tb}\ \alpha_t\ d_{sb}\ \alpha_{pm}\ l \\ &N_{s1}^*\ \alpha_3^*\ i_{qs,1}^r\ i_{ds,1}^r\ i_{qs,2}^r\ i_{ds,2}^r\ i_{qs,3}^r\ i_{ds,3}^r]^T\end{aligned} \tag{4.27}$$

where subscript s in $\boldsymbol{\theta}_s$ is used to distinguish between the AS-PMSM and SM-PMSM design space vectors.

Figs. 4.1-4.3 show the Pareto optimal fronts obtained for SM-PMSM design study sets 1-3 while Figs. 4.4-4.6 shows the Pareto optimal fronts obtained for the AS-PMSM designs study sets 4-6. The figures plot the weighted loss versus the machine cost. Each design set includes three repeated identical study runs.

Overall, the Pareto-optimal fronts in each study set match very closely which indicates that convergence has been reached. Note that a perfect match in Pareto-fronts in design problems with large design space, such as the one considered herein, should not be expected. In the next section, the design results of AS-PMSM are considered in more details and compared to SM-PMSM design results.

TABLE 4.5
Convergence Studies

Study Set	Machine Designed	Weighting Vector	Number of Repetitions
1	SM-PMSM	$\mathbf{w}_1$	3
2	SM-PMSM	$\mathbf{w}_2$	3
3	SM-PMSM	$\mathbf{w}_3$	3
4	AS-PMSM	$\mathbf{w}_1$	3
5	AS-PMSM	$\mathbf{w}_2$	3
6	AS-PMSM	$\mathbf{w}_3$	3

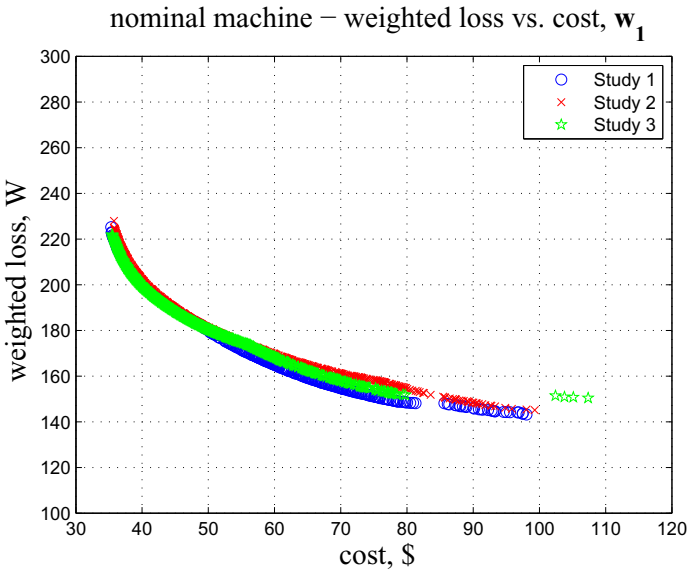

Fig. 4.1. SM-PMSM convergence study Set 1

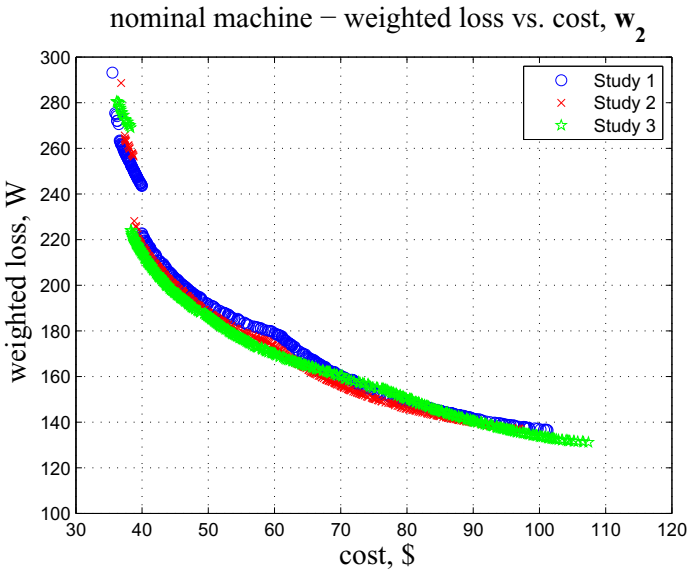

Fig. 4.2. SM-PMSM convergence study Set 2

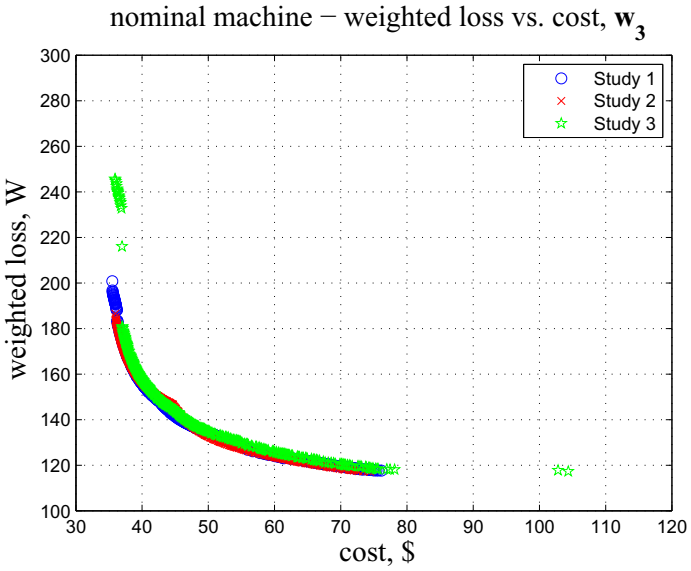

Fig. 4.3. SM-PMSM convergence study Set 3

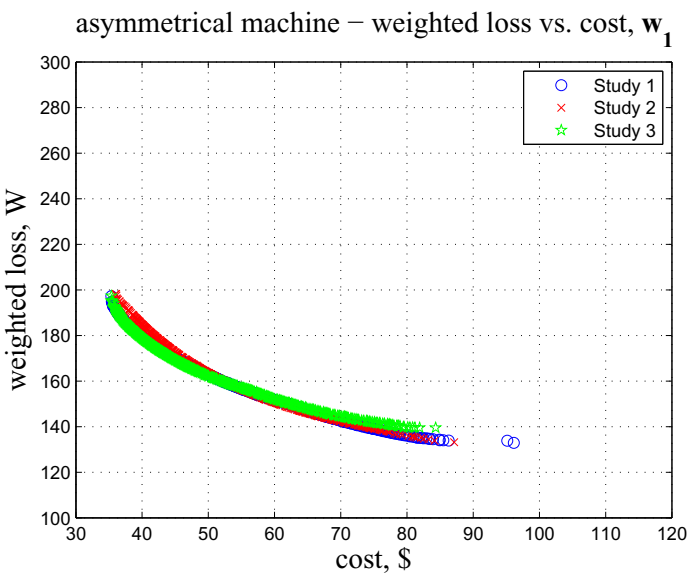

Fig. 4.4. AS-PMSM convergence study Set 4

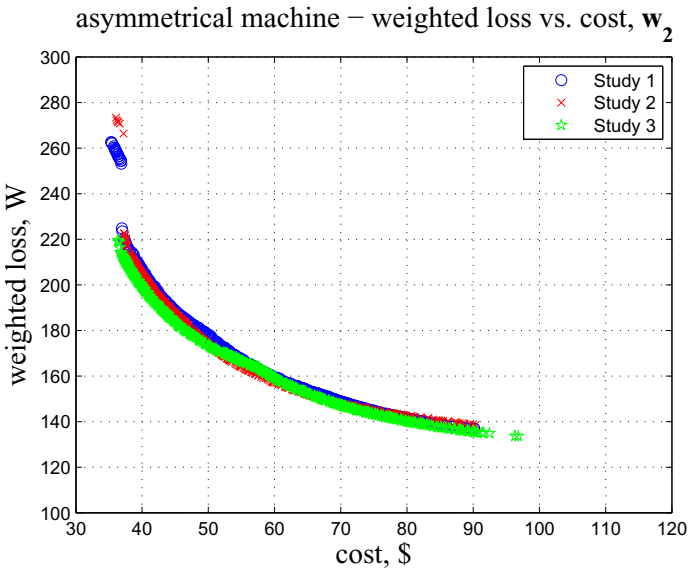

Fig. 4.5. AS-PMSM convergence study Set 5

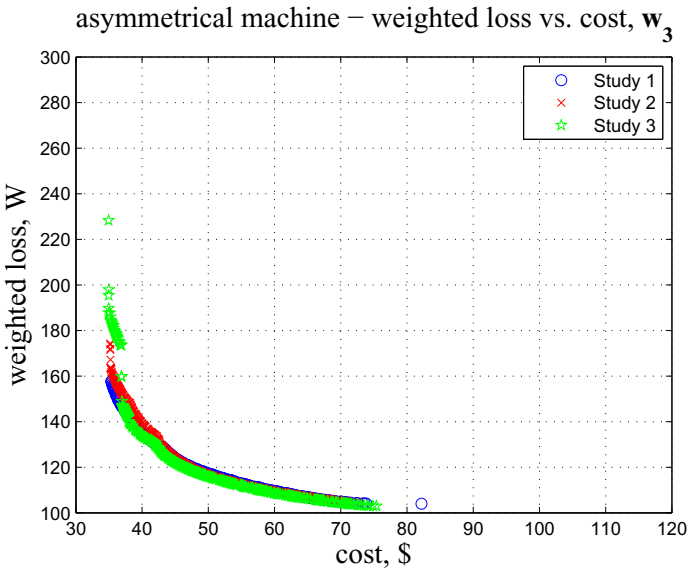

Fig. 4.6. AS-PMSM convergence study Set 6

4.4 Case Study 2: Comparing AS-PMSM to SM-PMSM

The design of the AS-PMSM under the design settings described in Sections 4.1 and 4.2 is considered herein. Only design results using weighting vector $\mathbf{w}_1$ are discussed in details while brief highlights on the results with weighting vectors $\mathbf{w}_2$ and $\mathbf{w}_3$ are included. The design results corresponding to Study 1 Pareto-front in Fig. 4.1 and Study 3 in Fig. 4.4 are used for the SM-PMSM and AS-PMSM comparison.

The Pareto designs gene distribution of the SM-PMSM and the AS-PMSM with weighting vector $\mathbf{w}_1$ are shown in Figs. 4.7 and 4.8, respectively. As a reminder, the *x*-axis which denotes parameter number, is ordered as shown in $\boldsymbol{\theta}_s$, (4.27), for the SM-PMSM and $\boldsymbol{\theta}$, (4.1), for the AS-PMSM. The design parameters in both cases are normalized between 0 and 1. Parameters of higher cost individuals within a population are placed on the left side of the column while individuals with lower cost are placed to the right of the column. A detailed explanation of the gene distribution plot is set forth in [28].

Parameters 1-3 in Figs. 4.7 and 4.8, as was discussed before were fixed to 1 by setting the minimum and maximum limits equal to 1. In Figs. 4.7 and 4.8, Parameter 4, which controls the type permanent magnet material, is equal to a normalized value of

0.84, which maps into Ferrite AC-12 permanent magnet. A few designs in both figures have a normalized value of around 0.33, which corresponds to SmCo R20 magnet.

Parameter 5 in both figures represents the number of pole pairs. Almost all SM-PMSM designs use the maximum allowed number of pole pairs, equal to 6. This is advantageous from a cost perspective since less magnet volume is needed as the number of magnetic poles increases. However, in the list of AS-PMSM designs, a number of designs have pole pair values equal to 5 and 4. Inspecting parameter 7, the rotor backiron thickness, these designs use a thicker rotor back iron which indicates that a high flux density level at the operating points considered required decreasing the number of pole pairs.

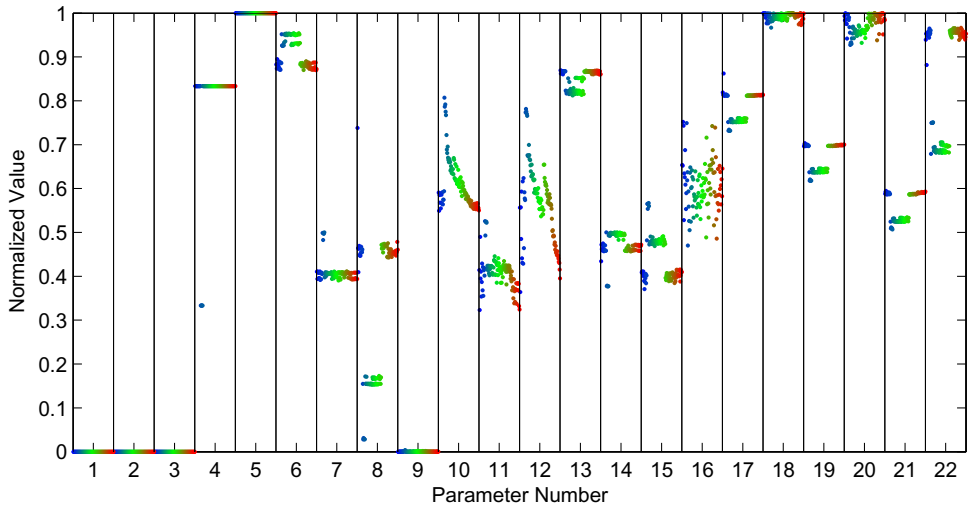

Fig. 4.7. Gene distribution plot for SM-PMSM design with $\mathbf{w}_1$

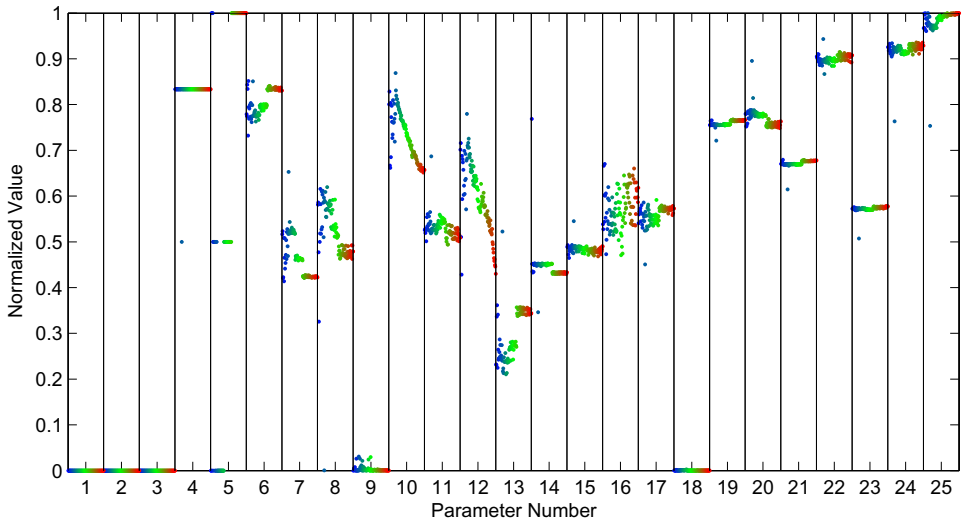

Fig. 4.8. Gene distribution plot for AS-PMSM design with $\mathbf{w}_1$

The 9th and 18th parameters in Fig. 4.8 are the air gaps g and g_{rt}^{*} . Both appear to be driven to their lower allowed limits. Since ferrite permanent magnet with low B_r is used, having a small air gap is much needed to achieve an effective and efficient transfer of flux between the rotor and stator. Parameters 25, the rotor tooth taper fraction, for the majority of designs is equal to 1.

A Pareto-optimal front comparison between the two machine topologies is shown in Fig. 4.9. The AS-PMSM outperforms the SM-PMSM by a significant amount as shown. For example, for a constant loss of 180 W, the AS-PMSM cost was \$40.0 while the SM-PMSM cost was \$50.0. This amounts to a cost saving of around 18%.

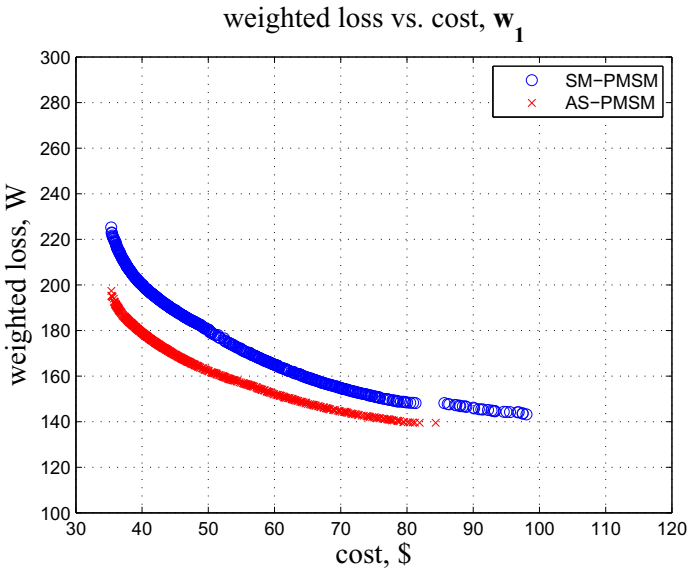

Fig. 4.9. Pareto optimal fronts with $\mathbf{w}_1$

In Fig. 4.10, the weighted power loss was plotted versus the machine mass for both the SM-PMSM and AS-PMSM. Overall, the mass of all AS-PMSM is less than the mass of SM-PMSM design for a given loss.

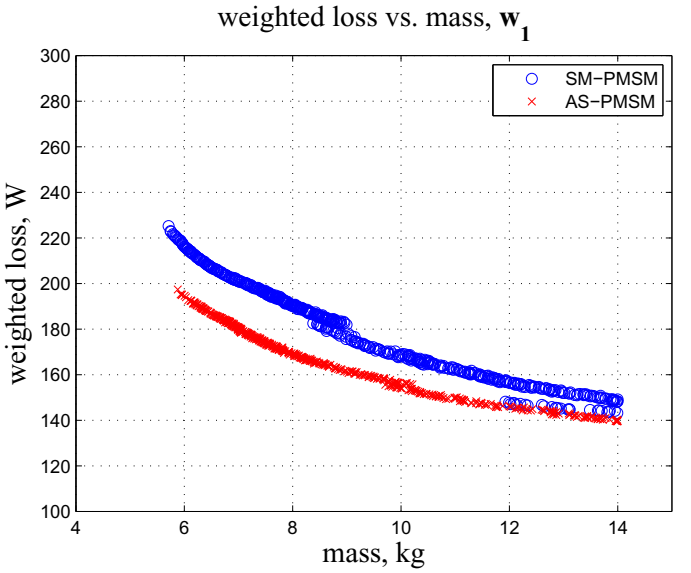

Fig. 4.10. Weighted power loss vs. mass with $\mathbf{w}_1$

Figs. 4.11-4.16 show various properties attributed with the AS-PMSM designs plotted versus cost. The mass versus cost for all designs is shown in Fig. 4.11. As expected, as machines become more massive the cost increases. The mass of all designs does not exceed the maximum limit of $M_{emmx} = 14\,\text{kg}$.

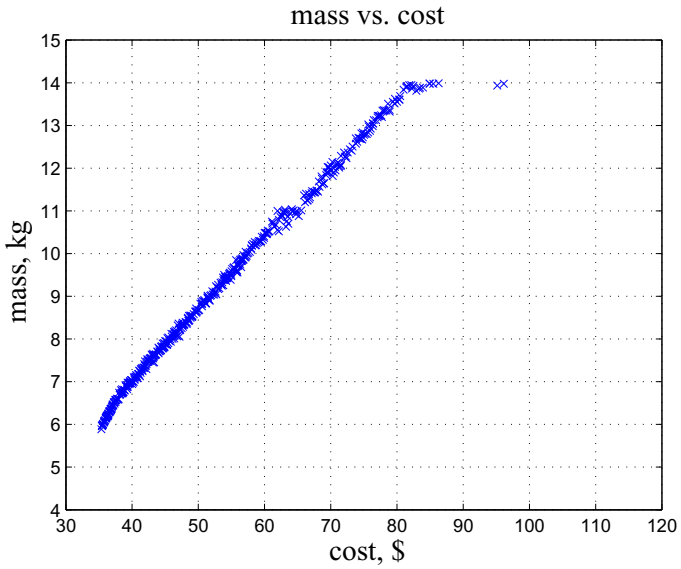

Fig. 4.11. AS-PMSM mass versus machine component cost

Fig. 4.12, a breakdown of separate machine component costs is given. The cost of the steel laminations, rotor laminations, conductors and permanent magnet is given. The most expensive component is the three phase conductors, followed by the stator steel. The cost of these two components keeps rising as the total cost increases. This is reflective of the increase of mass in these two regions, which is increased to lower conductive and core losses that are present only in the stator region. On the contrary, the cost of the rotor laminations and permanent magnet is mainly constant with respect to the total cost. Interestingly, the cheapest component was the permanent magnet. As was mentioned previously, the discontinuity beyond $85 is due to the change in permanent magnet type.

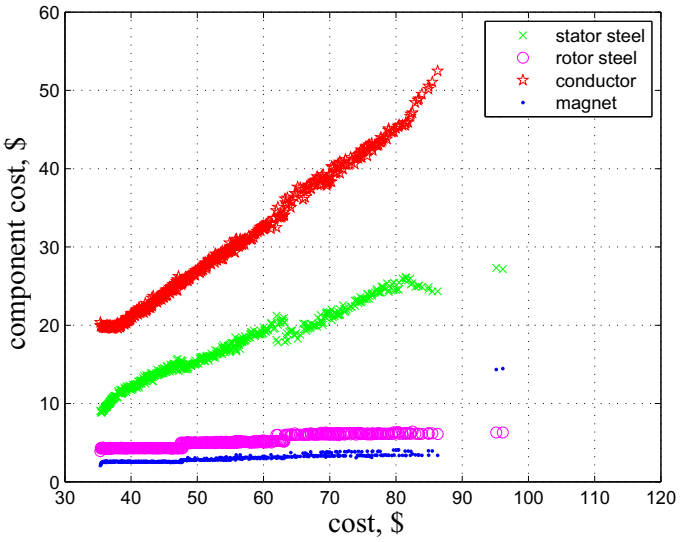

Fig. 4.12.Components cost versus machine cost

The permanent magnet-stator teeth and rotor teeth-stator teeth air gaps, g and g_{rt}, are plotted versus cost in Fig. 4.13 for all Pareto-front designs. Note that the minimum allowed gap was equal to 0.5 mm. Almost all designs minimized g and g_{rt} to 0.5 mm, which is mainly done to facilitate flux transfer between the rotor and stator. It can be seen that some designs have rotor tooth air gaps that are slightly smaller than the permanent magnet air gaps. The thicker tooth enhances the flux transfer mechanism between the rotor and the stator.

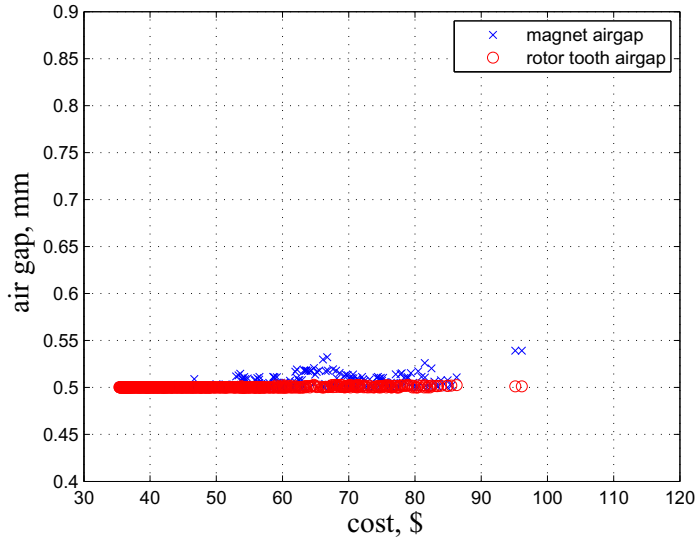

Fig. 4.13. Rotor tooth and permanent magnet air gaps versus machine cost

The fractions that control the span of the rotor tooth α_{rt}, the taper applied α_{tap}, and the depth of the rotor tooth d_{rt} are plotted in Fig. 4.14. Most designs have rotor tooth with $\alpha_{rt} = 0.6$ and no taper applied.

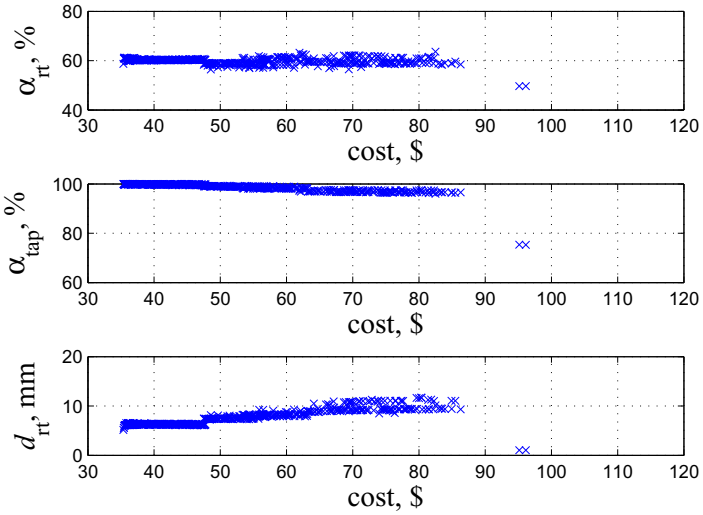

Fig. 4.14. α_{rt}, α_{tap} and d_{rt} versus machine cost

The Pareto-optimal fronts obtained from design studies with weighting vectors $\mathbf{w}_2$ and $\mathbf{w}_3$ are shown in Figs. 4.15 and 4.17, respectively. The weighted loss versus mass for these studies is shown in Figs. 4.16 and 4.18, respectively.

In general, based on the Pareto-optimal front comparison, the AS-PMSM outperforms the SM-PMSM. The improvements however are less significant in Fig. 4.15, where $\mathbf{w}_2$ was used. On the other hand, significant improvements are seen using AS-PMSM in Fig. 4.17, where $\mathbf{w}_3$ is used. The improvements seen therein are more significant than that seen in Fig. 4.9, when $\mathbf{w}_1$ was used. Finally note that AS-PMSM designs are less massive for a given loss than SM-PMSM designs, as illustrated in Figs. 4.16 and 4.18.

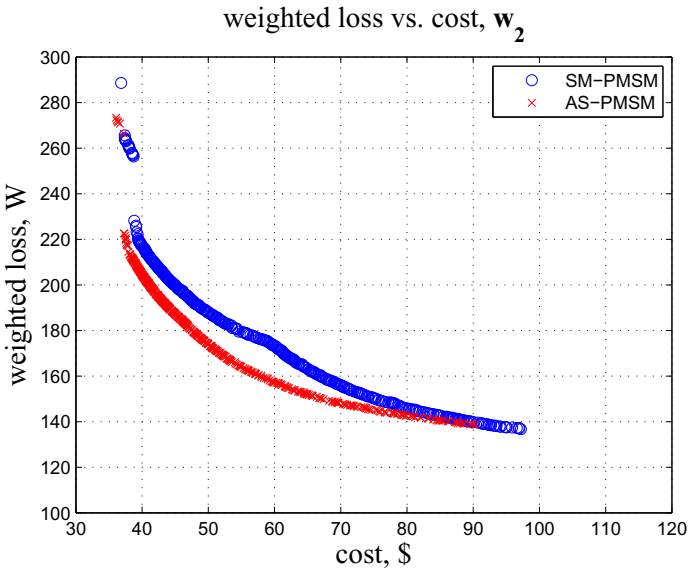

Fig. 4.15. Pareto optimal fronts with $\mathbf{w}_2$

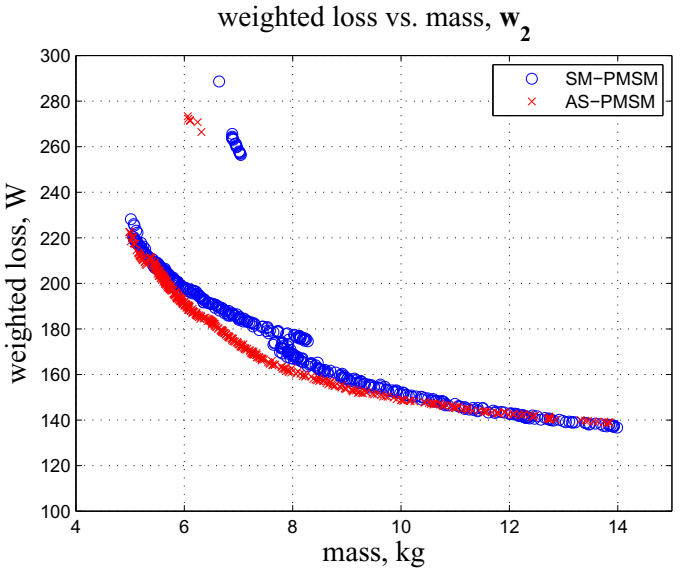

Fig. 4.16. Weighted power loss vs. mass with $\mathbf{w}_2$

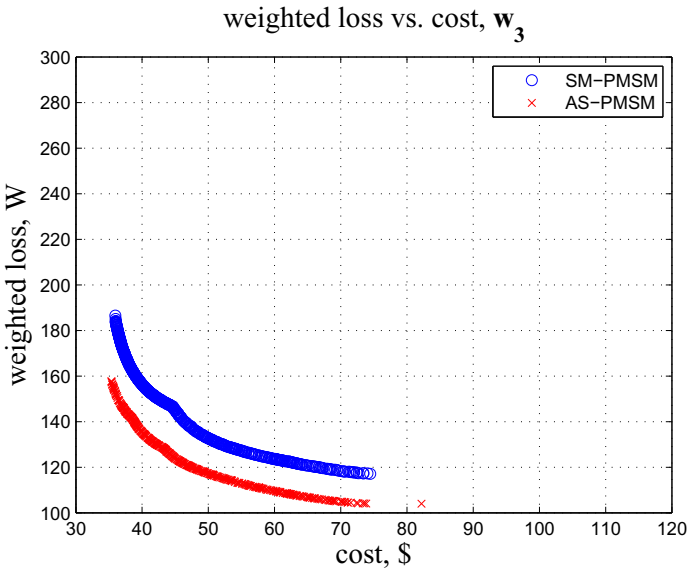

Fig. 4.17. Pareto optimal fronts with $\mathbf{w}_3$

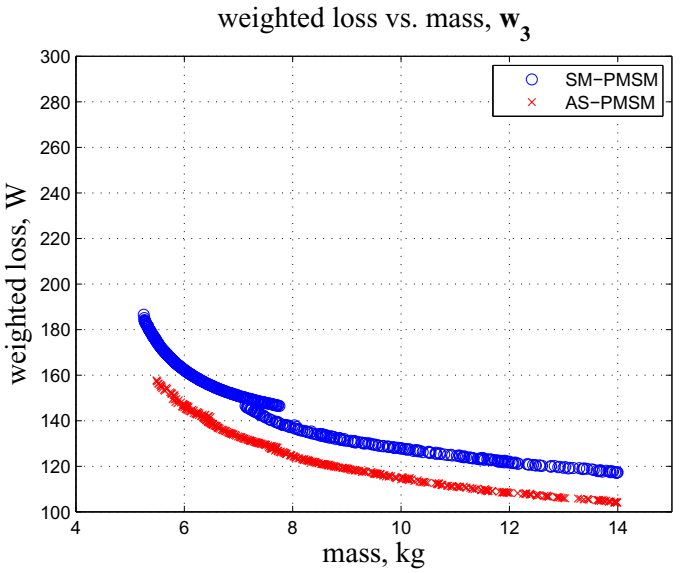

Fig. 4.18. Weighted power loss vs. mass with $\mathbf{w}_3$

For a closer inspection, the AS-PMSM Pareto-front design number 200 with cost of $46, mass of 8.1 kg and weighted power loss of 168 W was selected. Tables 4.6 and 4.7 list a number of properties for this design. A cross section of the machine is shown in Fig. 4.19, with an enlarged section shown in Fig. 4.20 to provide a closer look on the rotor pole.

TABLE 4.6
Design Number 200 Characteristics

Outside Diameter	21 cm	Tooth Fraction	53.3 %
Total Length	9.43 cm	Tooth Base Width:	0.366 cm
Active Length	5.45 cm	Stator Backiron Depth	0.998 cm
Number of Poles	12	Rotor Backiron Depth	0.527 cm
Number of Slots	72	Fundamental Conductor Density	90 cond/rad
Stator Material Type	M19	3rd Harmonic Conductor Density	42%
Rotor Material Type	M19	Conductor Diameter	1.76 mm
Conductor Type	Copper	Stator Iron Mass	4.25 kg
Permanent Magnet Type	Ferrite AC-12	Rotor Iron Mass	1.22 kg
Permanent Magnet Fraction	57.8%	Conductor Mass	2.21 kg
Permanent Magnet Depth	0.616 cm	Magnet Mass	0.448 kg
Permanent Mag. Rem. Flux Density	. 0.4 T	Mass	8.13 kg
Permanent Mag. Susceptibility	0.1	Stator Iron Cost	$14.9
Rotor tooth maximum depth	0.616 cm	Rotor Iron Cost	$4.28
Rotor tooth minimum depth	0.615 cm	Conductor Cost	$24.8
Rotor tooth span fraction	60.3 %	Magnet Cost	$2.51
Rotor tooth tapering fraction	99.8 %	Total Cost	$46.4
Stator Tooth Radius	7.87 cm	Weighted Total Loss	168 W
Shaft Radius	2 cm	A-Phase Winding Pattern (1st Pole)	[0 3 10 10 3 0]
Inert Radius	6.68 cm	Minimum Conductors Per Slot	13
Rotor Iron Radius	7.21 cm	Maximum Conductors Per Slot	13
Air Gap	0.5 mm	Packing Factor	50%
Slot Depth	1.62 cm		

TABLE 4.7
Design Number 200 Operating Point Performance Data

Speed Range	1000 rpm	2236 rpm	5000 rpm
Frequency Range	100 Hz	224 Hz	500 Hz
Q-Axis Voltages	50.0 V	104 V	217 V
D-Axis Voltages	-53.0 V	-65.0 V	-69.0 V
Peak Line-to-Line Voltages	126 V	213 V	395 V
Q-Axis Currents	19.5 A	10.6 A	5.23 A
D-Axis Currents	-7.42 A	-3.00 A	-2.46 A
Peak Line Currents	30.0 A	11.0 A	6.00 A
Current phase control angle	21 deg	15.2 deg	25.2 deg
Current Densities	6.05 A/mm^2 rms	3.19 A/mm^2 rms	1.68 A/mm^2 rms
Torque Range	18.0 Nm	8.10 Nm	3.72 Nm
Corrected Torque Range	17.8 Nm	7.97 Nm	3.56 Nm
Semiconductor Conduction Losses	79.8 W	42 W	22.1 W
Machine Resistive Losses	167 W	46.2 W	12.8 W
Machine Core Losses	19.0 W	30.6 W	82.6 W
Proximity Effect Losses	0.60 W	0.80 W	1.13 W
Skin Effect Losses	1.10 mW	1.50 mW	2.04 mW
Total Losses	266 W	120 W	119 W
Machine Efficiencies	91.0 %	96.0 %	95.1 %
Inverter Efficiencies	96.3 %	97.9 %	98.9 %
Machine plus Inverter Efficiencies	87.5 %	94.0 %	94.1 %
Stator Tooth Flux Dens. / Limit	90.3 %	50.7 %	45 %
Stator Backiron Flux Den. / Limit	52.5 %	42.8 %	35.2 %
Rotor Peak Tangential Flux Den. / Limit	99.5 %	81.0 %	66.7 %
Rotor Peak Radial Flux Den. / Limit	58.4 %	32.9 %	27.5 %
PM Demagnetization / Limit	43.7 %	30.9 %	25.0 %

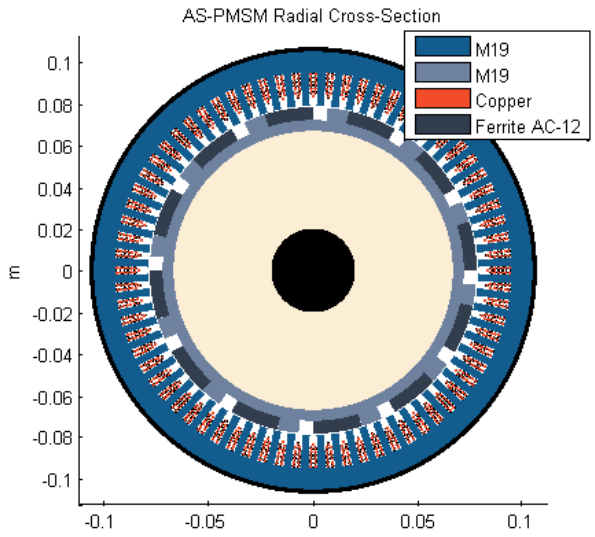

Fig. 4.19. Design number 200 cross section

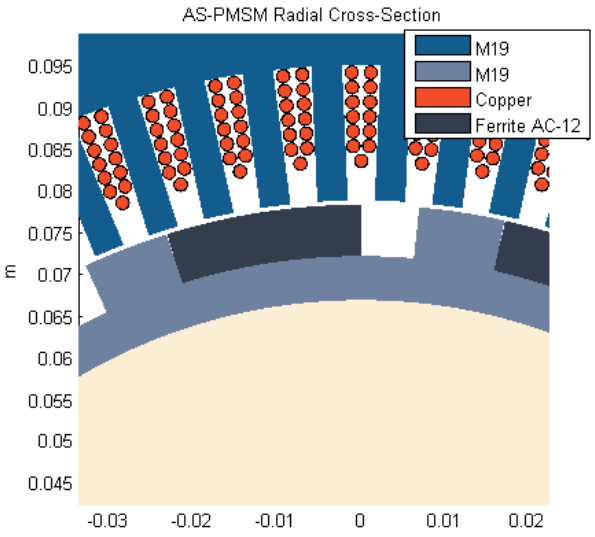

Fig. 4.20. Magnified section of design number 200

Various electrical and magnetical properties are plotted versus operating point in Figs. 4.21-4.28. Fig. 4.21 shows the *qd* currents and rms current at each operating point. Due to flux weakening, the *q*-axis current decreases as the rotor speed increases. Interestingly, *d*-axis current has a higher magnitude at lower speed than at high speed, which has to do with the production of saliency torque.

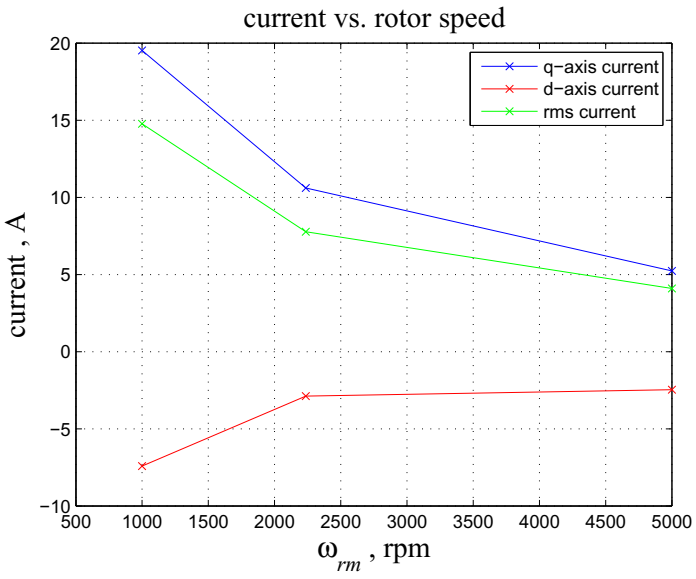

Fig. 4.21. AS-PMSM design number 200 *qd* and rms current versus rotor speed

The *qd* flux linkages versus rotor speed are shown in Fig. 4.22. The *q*-axis flux linkage sharply drops as speed increases due to the decrease in *q*-axis current.

The voltage versus rotor speed is displayed in Fig. 4.23. The rise in *q*-axis voltage is due to the increase in rotor speed. The peak line-to-line voltage at maximum speed is slightly below the limit that was imposed.

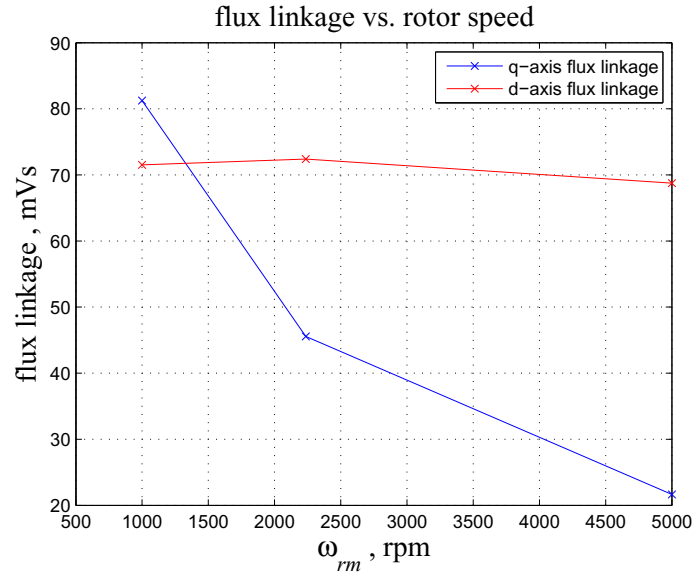

Fig. 4.22. AS-PMSM design number 200 *qd* flux linkages versus rotor speed

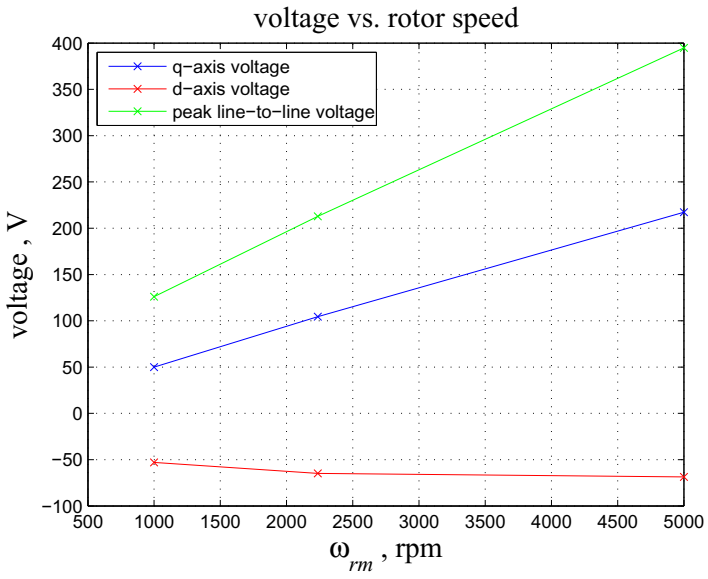

Fig. 4.23. AS-PMSM design number 200 *qd* and peak line-to-line voltages versus rotor speed

The loss profile versus rotor speed is shown in Fig. 4.24. Core loss increases with speed as expected. Machine dc conduction loss and switch conduction loss decrease as the speed increases mainly because of the decrease in rms current. AC losses; skin effect and proximity are negligible in this design, at least for the operating points modeled.

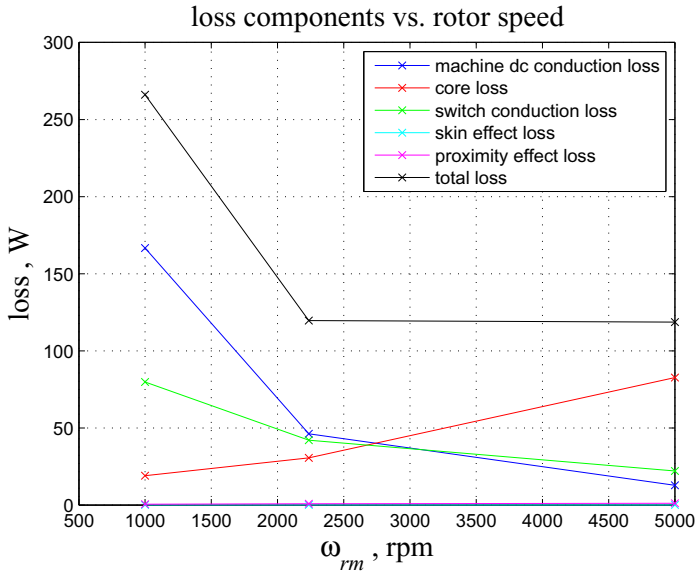

Fig. 4.24. AS-PMSM design number 200 losses versus rotor speed

The corrected torque and output power loss versus rotor speed are shown in Figs. 4.25 and 4.26 respectively. As observed in these figures, the output torque and power requirements have both been satisfied.

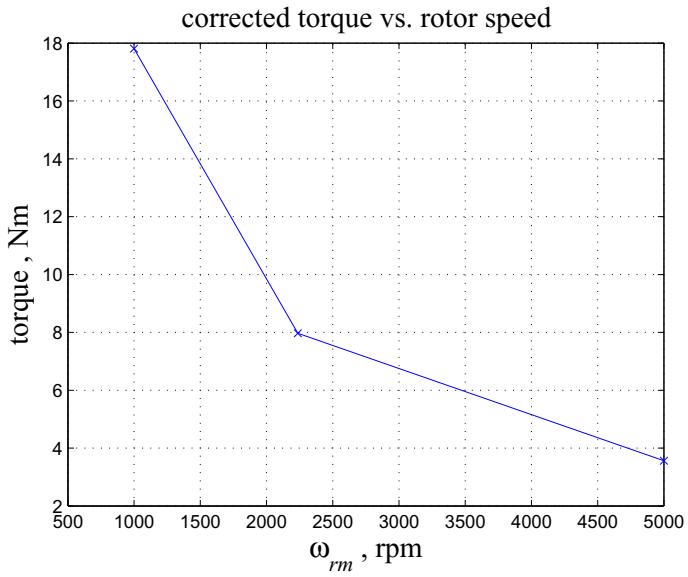

Fig. 4.25. AS-PMSM design number 200 corrected torque versus rotor speed

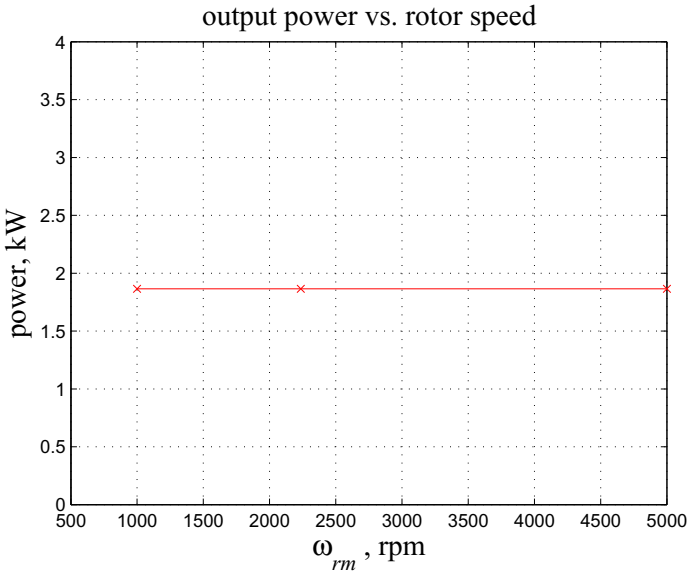

Fig. 4.26. AS-PMSM design number 200 output power versus rotor speed

The stator tooth spatial flux density over one magnetic pole is plotted in Fig. 4.27 for all operating points. Note that the analysis applied to find the air gap flux density starts from the edge of the permanent magnet as shown Fig. 3.3, which is located at $\phi_r \approx 42^o$. As can be seen, presence of the rotor tooth ($142^o < \phi_r < 192^o$) increases the magnitude of stator tooth flux density, which can be attributed to the decrease in air gap reluctance.

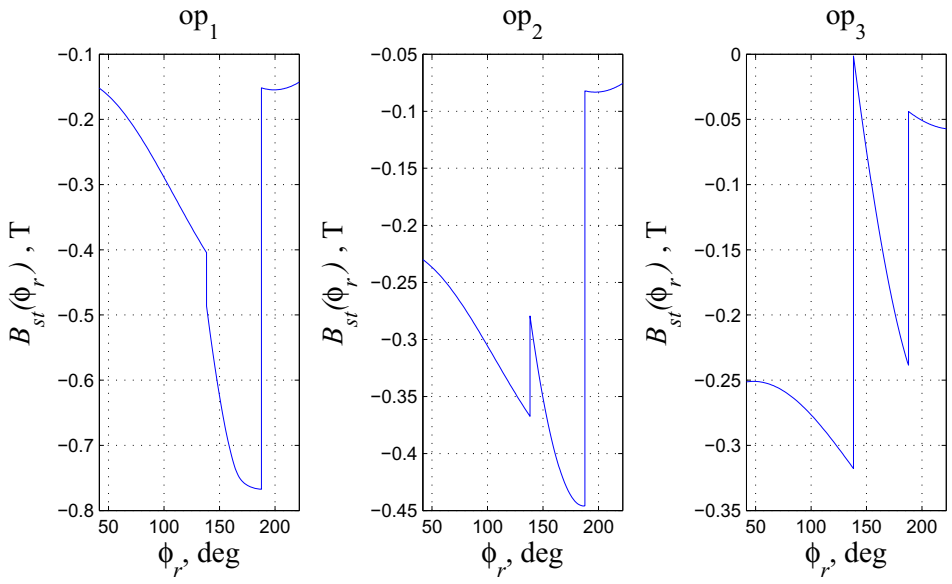

Fig. 4.27. Design number number 200 spatial stator tooth flux density over one magnetic pole for all three operating points

The temporal stator tooth and backiron flux densities versus rotor position for all operating points are shown in Fig. 4.28. The peak flux density in these waveforms has been successfully constrained under the limits imposed in Section 4.2. Also observed is the distorted shape of these waveforms, especially the tooth waveform. This is a result of the material discontinuity when transitioning from the permanent magnet to the rotor tooth.

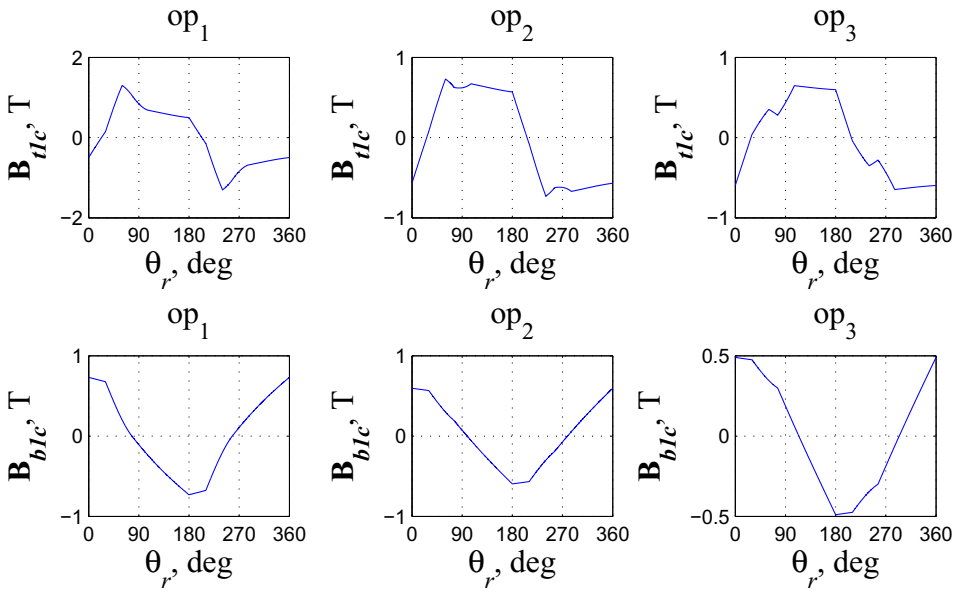

Fig. 4.28. Design number 200 stator tooth and backiron temporal flux densities versus rotor position for all three operating points

This concludes this chapter. In the next chapter, some of the results obtained by the analytical model are validated using 3D Finite Element Analysis (FEA). In particular, the electromagnetic torque and machine lumped model parameters obtained from the analytical model are compared to those obtained using a 3D FEA model.

5. FEA VALIDATION

Validation of the AS-PMSM design number 200, considered in Section 4.4, is conducted in this chapter using 3D Finite Element Analysis (FEA). The FEA software package ANSYS MAXWELL, version 16.0, is used. To increase confidence in the validation process, a SM-PMSM design is chosen from the Pareto-front Fig. 4.9 and validated using the FEA software. Section 5.1 briefly discusses the attributes of the FEA model. Section 5.2 validates the computed analytical torque against the FEA torque for both SM-PMSM and AS-PMSM selected designs. Finally, Section 5.3 validates the machine lumped model parameters for the SM-PSMM and AS-PMSM selected designs.

5.1 FEA Model

A picture of the selected SM-PMSM and AS-PMSM FEA models is shown in Figs. 5.1 and 5.2 respectively. The machines geometrical, electrical and magnetical properties are listed in Tables 5.1-5.4. It is important to point out that the steel type for the rotor and stator was M19 with non-linear *BH* characteristics.

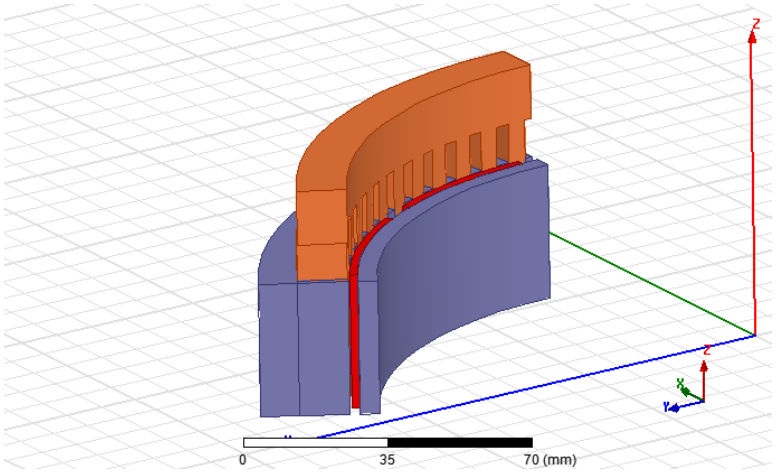

Fig. 5.1. SM-PMSM FEA Model

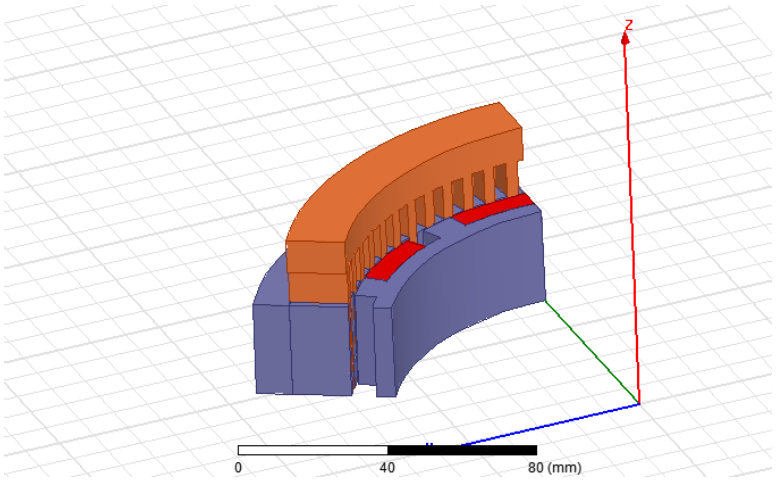

Fig. 5.2. AS-PMSM FEA Model

Note that due to symmetry, one pole pair is sufficient for simulation. In addition, the machine model can be further reduced by taking advantage of the axial symmetry along the *z*-axis, as shown in both figures. However, in calculations that require rotating the rotor of machine (quasi magneto-static), such as torque ripple calculations; all pole pairs of the machine are modeled but with the axial symmetry employed to reduce the computational time.

As discussed previously, a sinusoidaly distributed winding configuration is adopted. The sinusoidally distributed winding is implemented in the FEA model via a winding cylinder slotted through stator teeth. Excitation terminals were added into each slot with the axial excitation applied equal to

$$I_i = N_{as,i} i_{as} + N_{bs,i} i_{bs} + N_{cs,i} i_{cs} \tag{5.1}$$

where subscript i denotes the ith slot. Before proceeding, it should be noted that the FEA runs were based on energy convergence criteria. The target energy percentage error was set to be less than 5% in quasi magneto-static (Sections 5.2) and 1% in magneto-static (Section 5.3) simulations. The maximum number of mesh refinement passes set was equal to 10 for each quasi magneto-static study and 20 for each magneto-static study.

TABLE 5.1
Characteristics of SM-PMSM Design Used in FEA Validation

Outside Diameter	24.4 cm	Stator Backiron Depth	0.96 cm
Total Length	11.7 cm	Rotor Backiron Depth	0.47 cm
Active Length	6.90 cm	Fundamental Conductor Density	90 cond/rad
Number of Poles	12	3rd Harmonic Conductor Density	42%
Number of Slots	72	Conductor Diameter	1.83 mm
Stator Material Type	M19	Stator Iron Mass	5.33 kg
Rotor Material Type	M19	Rotor Iron Mass	1.45 kg
Conductor Type	Copper	Conductor Mass	2.86 kg
Permanent Magnet Type	Ferrite AC-12	Magnet Mass	0.33 kg
Permanent Magnet Fraction	81.8%	Mass	9.97 kg
Permanent Magnet Depth	0.19 cm	Stator Iron Cost	$18.7
Permanent Mag. Rem. Flux Density	0.4 T	Rotor Iron Cost	$5.08
Permanent Mag. Susceptibility	0.1	Conductor Cost	$32.0
Stator Tooth Radius	10.0 cm	Magnet Cost	$1.84
Shaft Radius	2 cm	Total Cost	$57.6
Inert Radius	9.28 cm	Weighted Total Loss	168 W
Rotor Iron Radius	9.75 cm	A-Phase Winding Pattern (1st Pole)	[0 3 10 10 3 0]
Air Gap	0.50 mm	Minimum Conductors Per Slot	13
Slot Depth	1.24 cm	Maximum Conductors Per Slot	13
Tooth Fraction	43.4 %	Packing Factor	50%
Tooth Base Width:	0.38 cm		

TABLE 5.2
Operating Point Performance Data of SM-PMSM Design Used in FEA Validation

Speed Range	1000 rpm	2236 rpm	5000 rpm
Frequency Range	100 Hz	224 Hz	500 Hz
Q-Axis Voltages	71.0 V	144 V	223 V
D-Axis Voltages	-45.1 V	-46.0 V	-49.7 V
Peak Line-to-Line Voltages	146 V	261 V	396 V
Q-Axis Currents	18.9 A	8.56 A	3.95 A
D-Axis Currents	-0.35 A	-1.35 A	-9.04 A
Peak Line Currents	18.9 A	8.66 A	10.0 A
Current phase control angle	1.10 deg	9.00 deg	66.4 deg
Current Densities	5.1 A/mm^2 rms	2.34 A/mm^2 rms	2.66 A/mm^2 rms
Torque Range	17.9 Nm	8.13 Nm	3.73 Nm
Corrected Torque Range	17.8 Nm	7.97 Nm	3.58 Nm
Semiconductor Conduction Losses	72.1 W	33.1 W	37.7 W
Machine Resistive Losses	155 W	32.6 W	42.3 W
Machine Core Losses	14.2 W	35.8 W	78.3 W
Proximity Effect Losses	0.36 W	0.38 W	2.46 W
Skin Effect Losses	1.10 mW	1.20 mW	7.70 mW
Total Losses	242 W	102 W	161 W
Machine Efficiencies	91.7 %	96.5 %	94.0 %
Inverter Efficiencies	96.6 %	98.3 %	98.1 %
Machine plus Inverter Efficiencies	88.5 %	94.8 %	92.2 %
Stator Tooth Flux Dens. / Limit	69.7 %	53.8 %	40.3 %
Stator Backiron Flux Den. / Limit	48.8 %	43.9 %	32.4 %
Rotor Peak Tangential Flux Den. / Limit	98.5 %	88.6 %	65.4 %
Rotor Peak Radial Flux Den. / Limit	33.9 %	25.8 %	20.6 %
PM Demagnetization / Limit	100 %	68.4 %	72.6 %

TABLE 5.3
Characteristics of AS-PMSM Design Used in FEA Validation

Outside Diameter	21 cm	Tooth Fraction	53.3 %
Total Length	9.43 cm	Tooth Base Width:	0.366 cm
Active Length	5.45 cm	Stator Backiron Depth	0.998 cm
Number of Poles	12	Rotor Backiron Depth	0.527 cm
Number of Slots	72	Fundamental Conductor Density	90 cond/rad
Stator Material Type	M19	3rd Harmonic Conductor Density	42%
Rotor Material Type	M19	Conductor Diameter	1.76 mm
Conductor Type	Copper	Stator Iron Mass	4.25 kg
Permanent Magnet Type	Ferrite AC-12	Rotor Iron Mass	1.22 kg
Permanent Magnet Fraction	57.8%	Conductor Mass	2.21 kg
Permanent Magnet Depth	0.616 cm	Magnet Mass	0.448 kg
Permanent Mag. Rem. Flux Density	. 0.4 T	Mass	8.13 kg
Permanent Mag. Susceptibility	0.1	Stator Iron Cost	$14.9
Rotor tooth maximum depth	0.616 cm	Rotor Iron Cost	$4.28
Rotor tooth minimum depth	0.615 cm	Conductor Cost	$24.8
Rotor tooth span fraction	60.3 %	Magnet Cost	$2.51
Rotor tooth tapering fraction	99.8 %	Total Cost	$46.4
Stator Tooth Radius	7.87 cm	Weighted Total Loss	168 W
Shaft Radius	2 cm	A-Phase Winding Pattern (1st Pole)	[0 3 10 10 3 0]
Inert Radius	6.68 cm	Minimum Conductors Per Slot	13
Rotor Iron Radius	7.21 cm	Maximum Conductors Per Slot	13
Air Gap	0.5 mm	Packing Factor	50%
Slot Depth	1.62 cm		

TABLE 5.4
Operating Point Performance Data of AS-PMSM Design Used in FEA Validation

Speed Range	1000 rpm	2236 rpm	5000 rpm
Frequency Range	100 Hz	224 Hz	500 Hz
Q-Axis Voltages	50.0 V	104 V	217 V
D-Axis Voltages	-53.0 V	-65.0 V	-69.0 V
Peak Line-to-Line Voltages	126 V	213 V	395 V
Q-Axis Currents	19.5 A	10.6 A	5.23 A
D-Axis Currents	-7.42 A	-3.00 A	-2.46 A
Peak Line Currents	30.0 A	11.0 A	6.00 A
Current phase control angle	21 deg	15.2 deg	25.2 deg
Current Densities	6.05 A/mm^2 rms	3.19 A/mm^2 rms	1.68 A/mm^2 rms
Torque Range	18.0 Nm	8.10 Nm	3.72 Nm
Corrected Torque Range	17.8 Nm	7.97 Nm	3.56 Nm
Semiconductor Conduction Losses	79.8 W	42 W	22.1 W
Machine Resistive Losses	167 W	46.2 W	12.8 W
Machine Core Losses	19.0 W	30.6 W	82.6 W
Proximity Effect Losses	0.60 W	0.80 W	1.13 W
Skin Effect Losses	1.10 mW	1.50 mW	2.04 mW
Total Losses	266 W	120 W	119 W
Machine Efficiencies	91.0 %	96.0 %	95.1 %
Inverter Efficiencies	96.3 %	97.9 %	98.9 %
Machine plus Inverter Efficiencies	87.5 %	94.0 %	94.1 %
Stator Tooth Flux Dens. / Limit	90.3 %	50.7 %	45 %
Stator Backiron Flux Den. / Limit	52.5 %	42.8 %	35.2 %
Rotor Peak Tangential Flux Den. / Limit	99.5 %	81.0 %	66.7 %
Rotor Peak Radial Flux Den. / Limit	58.4 %	32.9 %	27.5 %
PM Demagnetization / Limit	43.7 %	30.9 %	25.0 %

5.2 FEA Torque Results

The FEA torque is calculated over a rotor mechanical position spanning two stator teeth and slots with and increment of $1°$ (Note the span of a stator tooth and slot is equal to $360°/S_s$, which is equal to $5°$ for both the SM-PMSM and AS-PMSM machines considered in Tables 5.1 and 5.2, respectively). Figs. 5.3 and 5.4 display the 3-D FEA torque versus rotor position for the SM-PMSM and AS-PMSM machines at all three operating points.

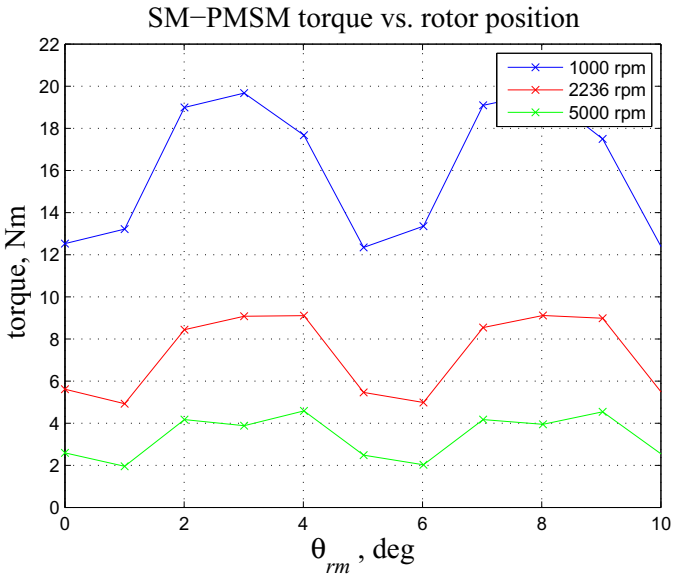

Fig. 5.3. SM-PMSM FEA torque versus rotor position

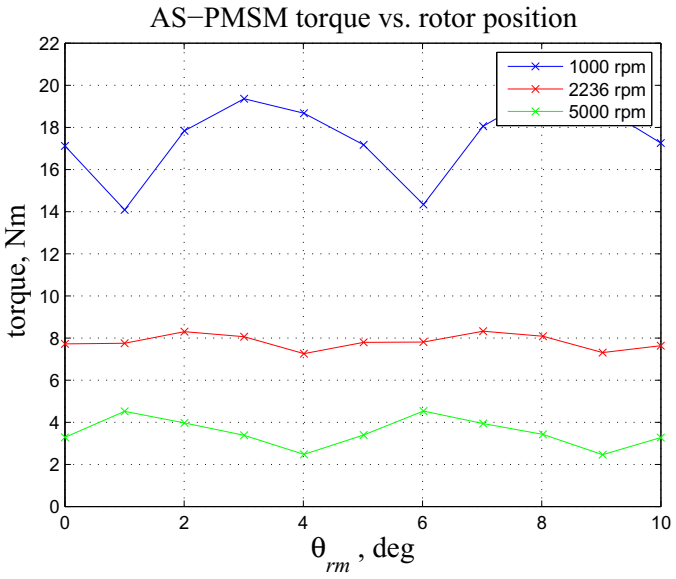

Fig. 5.4. AS-PMSM FEA torque versus rotor position

The average torque is computed and compared to the analytical model torque in Tables 5.5 and 5.6 respectively. A very close agreement is observed between the two models. Also shown is the percentage torque ripple. The percentage torque ripple for each operating point is calculated using

$$T_{e,ripple} = \frac{\left(T_{e,mx} - T_{e,mn}\right)}{T_{e,av}} 100 \tag{5.2}$$

where $T_{e,mx}$, $T_{e,mn}$ and $T_{e,av}$ are the maximum, minimum and average torque over rotor positions spanning an integer number of stator tooth and slot.

TABLE 5.5
SM-PMSM Analytical and FEA Torque

Rotor Speed (rpm)	Analytical Torque (Nm)	3-D FEA Torque (Nm)	% Error	FEA $T_{e,ripple}(\%)$
1000 rpm	17.9	16.0	10.3	46.4
2236 rpm	8.13	7.24	10.8	57.9
5000 rpm	3.73	3.35	10.2	78.6

TABLE 5.6
AS-PMSM Analytical and FEA Torque

Rotor Speed (rpm)	Analytical Torque (Nm)	3-D FEA Torque (Nm)	% Error	FEA $T_{e,ripple}(\%)$
1000 rpm	18.0	17.5	2.80	32.0
2236 rpm	8.10	7.82	3.46	13.6
5000 rpm	3.70	3.51	5.14	59.1

The no-load/cogging torque was calculated for both machines. The result is shown in Figs. 5.5 and 5.6.

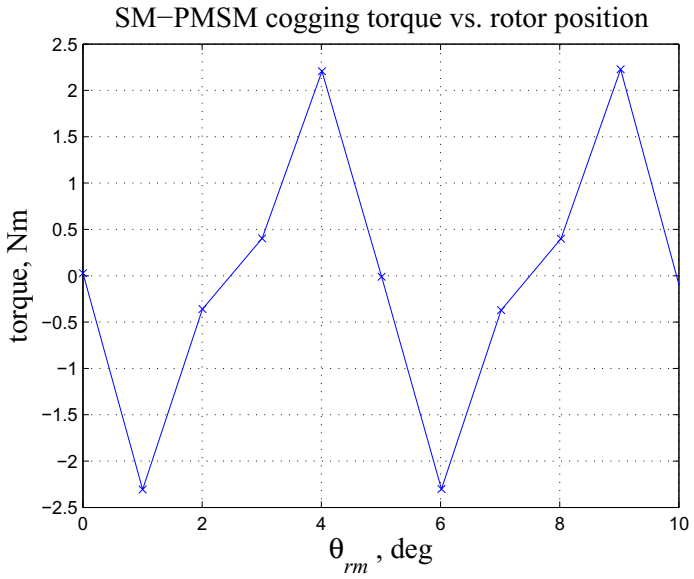

Fig. 5.5. SM-PMSM FEA cogging torque versus rotor position

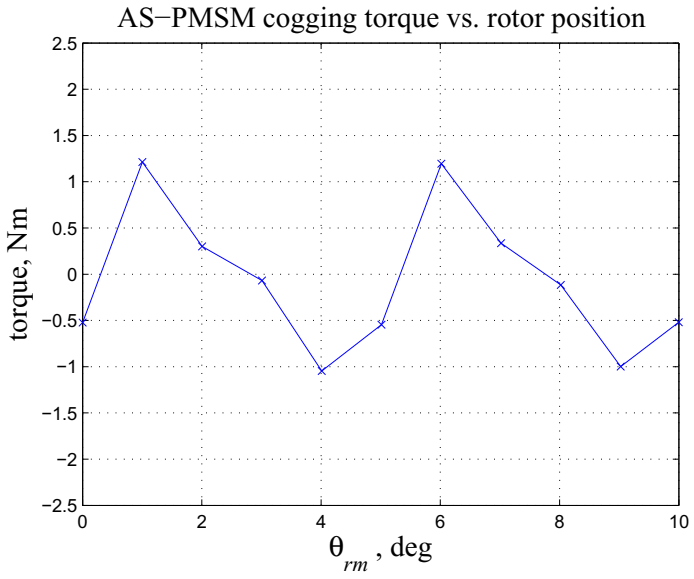

Fig. 5.6. AS-PMSM FEA cogging torque versus rotor position

5.3 Machine Lumped Model Parameters

The machine parameters in interest are L_q, L_d for the SM-PMSM and L_{qq}, L_{dd}, L_{qd} (described in Chapter 2). The permanent magnet flux linkage λ_m is also considered in this validation.

The machine lumped model parameters for the SM-PMSM calculated using the analytical model are shown in Table 5.7. These were calculated form the knowledge of the *qd* flux linkage and excitation currents. Note that since negligible saliency exist, $L_q = L_d$.

The machine lumped model parameters from the FEA model were obtained using the total energy of the system. It can be shown that for a SM-PMSM, the co-energy stored in the system with the magnet turned off (i.e.: $B_r = 0$ and $\chi = 0$) is equal to

$$\begin{aligned} \mathrm{W}_c(\theta_r) &= \frac{1}{2}(L_{ls} + L_{ms})\left[i_{as}^2 + i_{bs}^2 + i_{cs}^2\right] \\ &\quad -\frac{1}{2}L_{ms}\left[i_{as}i_{bs} + i_{as}i_{cs} + i_{bs}i_{cs}\right] \\ &\quad +\lambda_m\left[i_{as}\sin(\theta_r) + i_{bs}\sin\left(\theta_r - \frac{2\pi}{3}\right) + i_{cs}\sin\left(\theta_r + \frac{2\pi}{3}\right)\right] \end{aligned} \tag{5.3}$$

Setting $i_{as} = 1\text{A}, i_{bs} = -\frac{1}{2}\text{A}$ and $i_{cs} = -\frac{1}{2}\text{A}$ (i.e.: $i_{qs}^r = 1\text{A}$ and $i_{ds}^r = 0\text{A}$), the inductance is related to the energy by

$$L_q = L_d = \frac{4}{3}\text{W}_c\left(\theta_r\right) \tag{5.4}$$

where

$$L_q = L_d = L_{ls} + \frac{3}{2}L_{ms} \tag{5.5}$$

Hence, a magneto-static simulation with $\theta_r = 0$ and under the electric and magnetic settings described above was applied, and the energy calculated was used to calculate the *qd* inductances. These are shown in Table 5.7. Agreement between analytical and FEA calculated inductances can be seen.

TABLE 5.7
SM-PMSM *qd* Inductances

	Analytical	3-D FEA	% Error
L_q	3.65 mH	3.62 mH	0.8
L_d	3.65 mH	3.66 mH	-0.3

As was mentioned in Chapter 2, the flux linkage equation for the AS-PMSM can be written as

$$\begin{bmatrix}\lambda_{qs}^r \\ \lambda_{ds}^r\end{bmatrix} = \begin{bmatrix}L_{qq} & L_{qd} \\ L_{qd} & L_{dd}\end{bmatrix}\begin{bmatrix}i_{qs}^r \\ i_{ds}^r\end{bmatrix} + \lambda_m\begin{bmatrix}0 \\ 1\end{bmatrix} \tag{5.6}$$

where

$$L_{qq} = L_q\cos\left(\phi_{dm}\right)^2 + L_d\sin\left(\phi_{dm}\right)^2 \tag{5.7}$$

$$L_{dd} = L_q\sin\left(\phi_{dm}\right)^2 + L_d\cos\left(\phi_{dm}\right)^2 \tag{5.8}$$

$$L_{qd} = \left(L_q - L_d\right)\cos\left(\phi_{dm}\right)\sin\left(\phi_{dm}\right) \tag{5.9}$$

Using the *qd* input power equation, which is given as

$$P_{in} = \frac{3}{2}\left(\frac{d\lambda_{qs}^{r}}{dt} i_{qs}^{r} + \frac{d\lambda_{ds}^{r}}{dt} i_{ds}^{r} \right), \tag{5.10}$$

and applying an excitation ramping procedure with the magnet turned off, the co-energy of the system can be shown to be given by

$$\mathrm{W}_{c}\left(\theta_{r}\right) = \frac{3}{2}\left(\frac{L_{qq}\left(i_{qs}^{r}\right)^{2}}{2} + \frac{L_{dd}\left(i_{ds}^{r}\right)^{2}}{2} + L_{qd}\, i_{qs}^{r} i_{ds}^{r} \right) \tag{5.11}$$

The co-energy with the magnet turned off, (5.11), is calculated under three different excitation settings at $\theta_r = 0$: first with $i_{qs}^{r} = 1\,\mathrm{A}$, $i_{ds}^{r} = 0\,\mathrm{A}$, second with $i_{qs}^{r} = 0\,\mathrm{A}$, $i_{ds}^{r} = 1\,\mathrm{A}$ and finally with $i_{qs}^{r} = 1\,\mathrm{A}$, $i_{ds}^{r} = 1\,\mathrm{A}$. The energy calculated from each setting is then used to find L_{qq}, L_{qq} and L_{qd}. In order to have an equal comparison between the analytical and FEA model, the rotor in the FEA model should be aligned similarly to the alignment adopted in the analytical model. This means that the position of the first stator slot should at $\phi_{sm} = \pi / S_s$ and the *q*-axis of the machine aligned with the *a*-phase axis when $\theta_r = 0$.

The AS-PMSM analytical and FEA inductances are listed in Table 5.8. The analytical model inductances were calculated using the flux linkage equation (5.6). The *qd* flux linkages were calculated with $i_{qs}^{r} = 1\,\mathrm{A}$, $i_{ds}^{r} = 0\,\mathrm{A}$ and $i_{qs}^{r} = 0\,\mathrm{A}$, $i_{ds}^{r} = 1\,\mathrm{A}$ with permanent magnet turned off. The calculated flux linkages were then used to find the analytical L_{qq}, L_{qq} and L_{qd}.

TABLE 5.8
AS-PMSM *qd* Inductances

	Analytical	3-D FEA	% Error
L_{qq}	4.50 mH	4.96 mH	-10.2
L_{dd}	1.73 mH	2.02 mH	-16.6
L_{qd}	0.82 mH	0.75 mH	8.54

In order to calculate λ_m using the FEA model, the magnetic flux flowing through the stator teeth across one magnetic pole (i.e.: stator tooth 1 to S_s / P) was recorded as a function of rotor position in an open circuit test. The rotor was rotated from position

$\theta_{rm} = 0$ to $\theta_{rm} = 2\pi / P$. The stator teeth magnetic flux was then used to find the *abc* flux linkages using

$$\lambda_x(\theta_{rm}) = 2P\sum_{i=1}^{S_s/P}\left(\Phi_i(\theta_{rm})W_{x,i}\right) \tag{5.12}$$

where Φ_i is the magnetic flux through a cross section positioned at the middle of tooth *i* and $W_{x,i}$ is the discrete winding function for phase *x* in slot *i*. The summation in (5.12) is multiplied by *P* to account for the remaining magnetic poles in the machine and then multiplied by 2 take into consideration the *xy* symmetry applied. Note that the discrete winding function can be calculated using the method describe in [28].

The *abc* flux linkages found using (5.12) are then transformed into the *qd* frame of reference using the reference frame transformation given as

$$\begin{bmatrix}\lambda^r_{qs}(\theta_{rm})\\ \lambda^r_{ds}(\theta_{rm})\end{bmatrix} = \frac{2}{3}\begin{bmatrix}\cos\left(\frac{P}{2}\theta_{rm}\right) & \cos\left(\frac{P}{2}\theta_{rm}-\frac{2\pi}{3}\right) & \cos\left(\frac{P}{2}\theta_{rm}+\frac{2\pi}{3}\right)\\ \sin\left(\frac{P}{2}\theta_{rm}\right) & \sin\left(\frac{P}{2}\theta_{rm}-\frac{2\pi}{3}\right) & \sin\left(\frac{P}{2}\theta_{rm}+\frac{2\pi}{3}\right)\end{bmatrix}\begin{bmatrix}\lambda_{as}(\theta_{rm})\\ \lambda_{bs}(\theta_{rm})\\ \lambda_{cs}(\theta_{rm})\end{bmatrix} \tag{5.13}$$

The SM-PMSM *abc* flux linkages and *qd* flux linkages are shown in Figs 5.7 and 5.8 respectively. The average *qd*-flux linkages are shown in Table 5.9 along with the analytically calculated *qd*-flux linkages. The error between the FEA and analytical model is defined differently here using the equation

$$e = \frac{\sqrt{\left(\overline{\lambda}^r_{qs,f} - \lambda^r_{qs,a}\right)^2 + \left(\overline{\lambda}^r_{ds,f} - \lambda^r_{ds,a}\right)^2}}{\sqrt{\left(\lambda^r_{qs,f}\right)^2 + \left(\lambda^r_{ds,f}\right)^2}}100 \tag{5.14}$$

were the extra subscript '*f* ' denotes the FEA calculated flux linkage while subscript '*a*' denotes the analytical calculated flux linkage. The horizontal line above the FEA calculated flux linkage denotes the average value. Using (5.15), the error was calculated to be equal to 11.1 %.

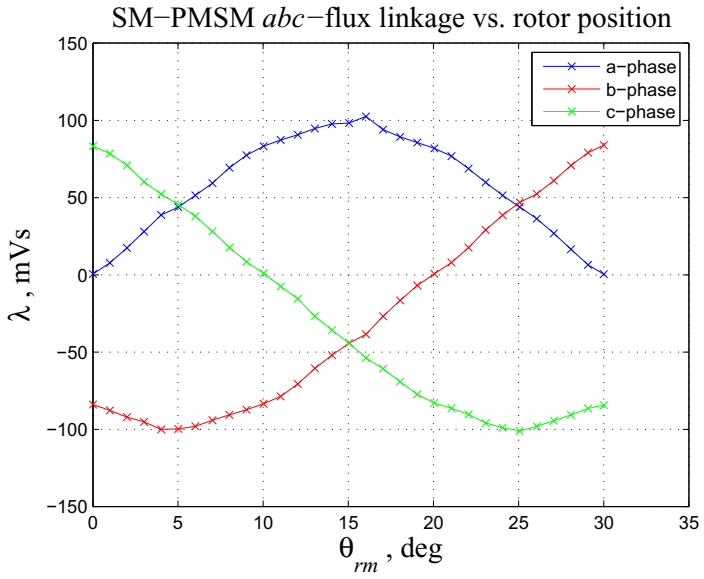

Fig. 5.7. SM-PMSM FEA *abc* flux linkages versus rotor position

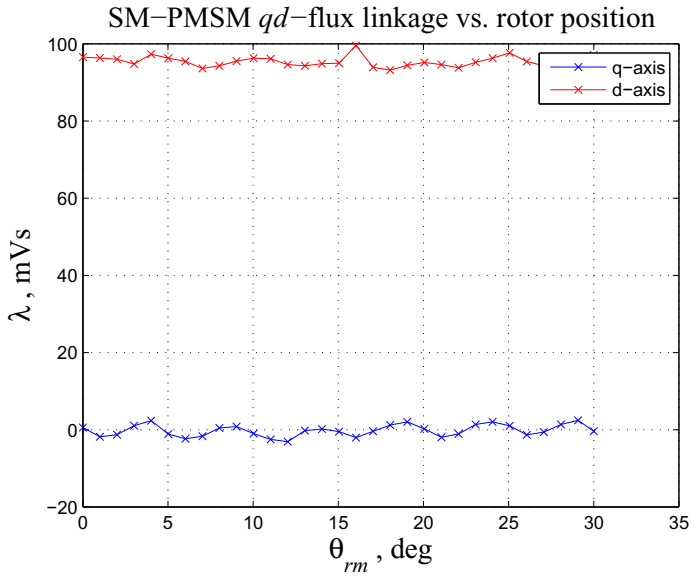

Fig. 5.8. SM-PMSM FEA *qd* flux linkages versus rotor position

TABLE 5.9
SM-PMSM Average *qd* Flux Linkages

	Analytical	3-D FEA
$\overline{\lambda}_{qs}^{r}$	0 mVs	-0.20 mVs
$\overline{\lambda}_{ds}^{r}$	106 mVs	95.4 mVs

Following the same approach, the *abc*- and *qd*-flux linkages for the AS-PMSM are calculated and shown in Figs 5.9 and 5.10. The average *qd* flux linkages from the FEA model and the analytical *qd* flux linkages are shown in Table 5.10.

A noteworthy *q*-axis flux linkage is present in the FEA model while nothing was predicted in the analytical model. The reason for this is leakage flux flowing at the permanent magnet and rotor tooth interface. This presence of the flux leakage shifts the *d*-axis from the center of the magnet and results in a non-zero average *q*-axis flux linkage. Therefore, to account for this effect, future work will include provisions to model flux leakage using the analytical model. Using (5.14), the error between the FEA and analytical models was calculated to be equal to 8.06 %.

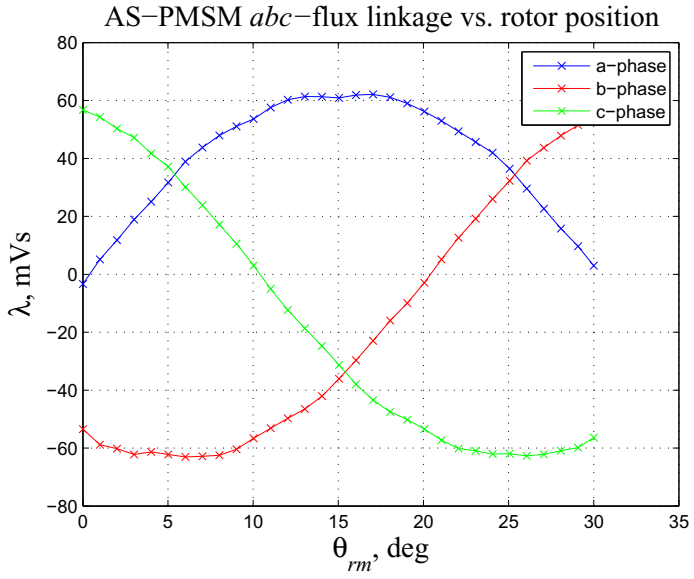

Fig. 5.9. AS-PMSM FEA *abc* flux linkages versus rotor position

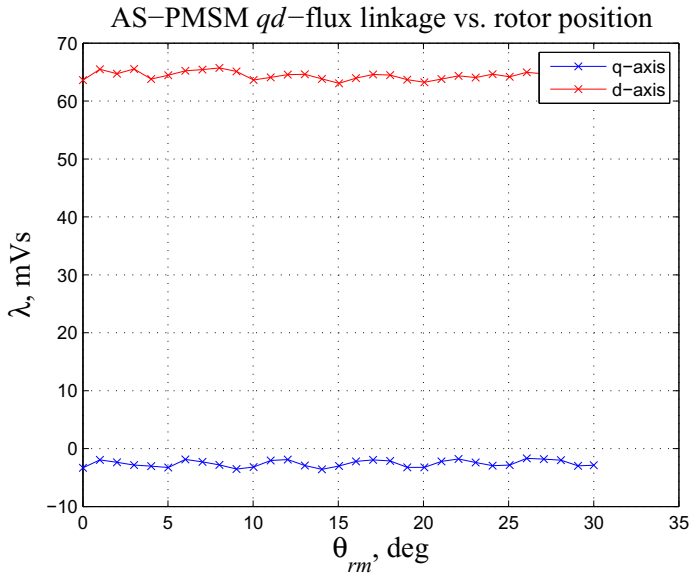

Fig. 5.10. AS-PMSM FEA *qd* flux linkages versus rotor position

TABLE 5.10
AS-PMSM Average *qd* Flux Linkages

	Analytical	3-D FEA
$\overline{\lambda}_{qs}^{r}$	0 mVs	-2.60 mVs
$\overline{\lambda}_{ds}^{r}$	69.0 mVs	64.4 mVs

In conclusion for this chapter, a good and acceptable agreement between the analytical model and 3-D FEA results were obtained. In the next chapter, a case study is considered. Therein, a traction motor for a heavy hybrid vehicle application is designed. An AS-PMSM and SM-PMSM are designed for the given application and then compared to find which architecture performs better.

6. HOOSIER HEAVY HYBRID VEHICLE CASE STUDY

In this chapter, a traction motor for a heavy hybrid electric bus is designed. Section 6.1 discusses the design specifications for this application. In Section 6.2, the procedure to select operating points that are incorporated into the machine design process is set forth. Section 6.3 includes a discussion on the design space and objective functions. Finally, Section 6.4 includes the results of the optimization and a discussion on the findings.

6.1 Hoosier Heavy Hybrid Electric Vehicle Project Description

The system considered is depicted in Fig. 6.1. Therein, a block diagram describing a parallel hybrid transit bus is shown..

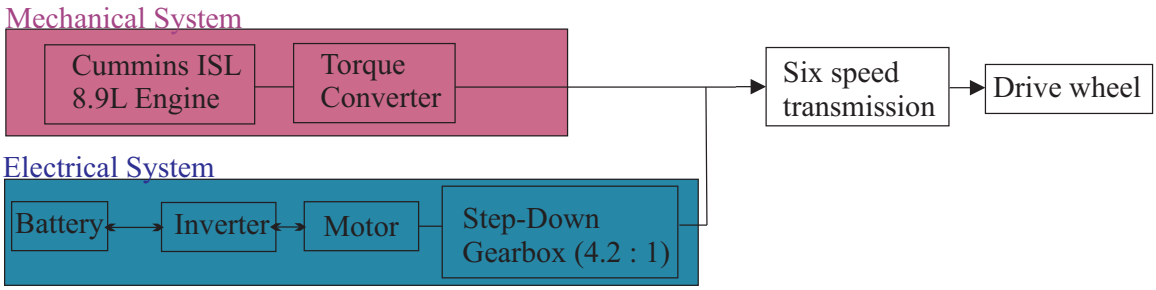

Fig. 6.1. Parallel hybrid transit bus system block diagram

The overall system can be divided into a mechanical and an electrical system that are connected in parallel to produce the torque needed to drive the vehicle. The engine is Cummins ISL 8.9L (6 cylinder) rated at 215 kW at 2000 rpm, maximum torque of 1200 Nm at 1300 rpm, and a maximum rotational speed of 2400 rpm. A continuous torque converter (a clutch that varies smoothly between off/on or on/off states) is used to engage and disengage the engine as needed.

The electrical system includes the electric motor which is connected to a battery/three phase inverter system. The battery is rated at 256 V. The electric motor is rated at a peak power of approximately 100 kW at 8498 rpm. The two way arrows

connecting the battery, inverter and motor are to indicate that bidirectional energy transfer is considered in this application. The motor is operated as a generator when regenerative braking is applied. A speed reduction gear box of 4.2 : 1 is connected to the motor output. The gearbox ensures that the output speed of the electric motor and the engine are matched, and thus their torque can be combined to feed the six speed transmission gearbox.

The goal of this chapter is to design an electric motor suitable for the given application. The procedure applied in Chapters 3 and 4 is applied herein for this purpose, were a SM-PMSM and an AS-PMSM are designed and compared to see which machine architecture better suits this application.

6.2 Operating Points Selection

Figs. 6.2 and 6.3 illustrate the required torque and speed time trajectories of the electric motor based on the Manhattan, NY drive cycle. These trajectories map into the torque versus speed curve shown in Fig 6.4. Note that negative torque indicates energy generation by means of regenerative braking. The generated energy is transferred and stored in the battery.

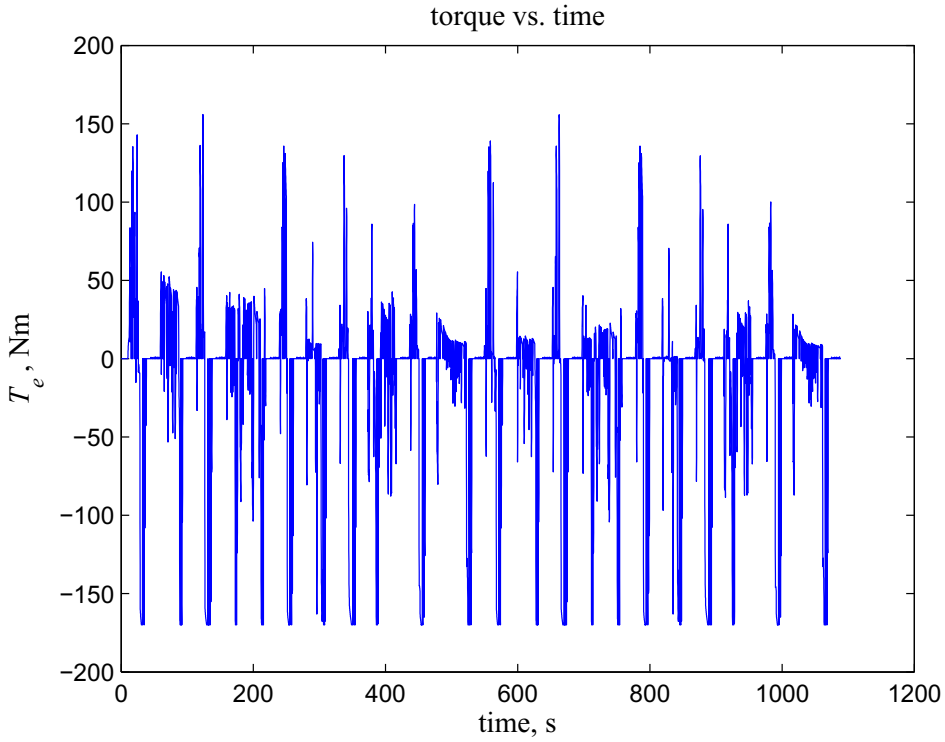

Fig. 6.2 Torque versus time trajectory

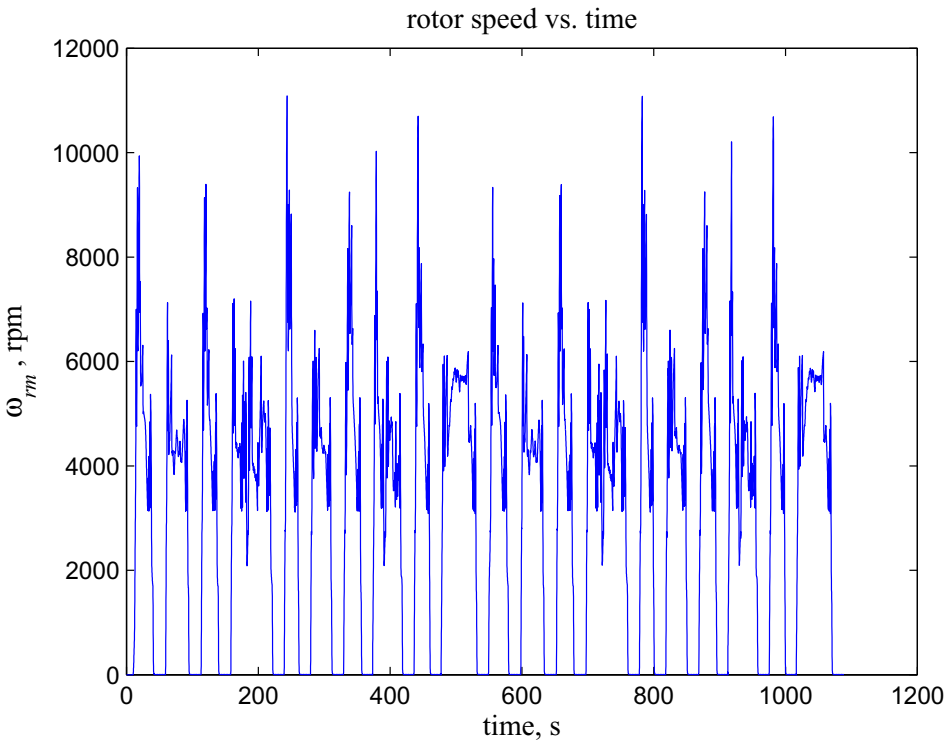

Fig. 6.3 Rotor speed versus time trajectory

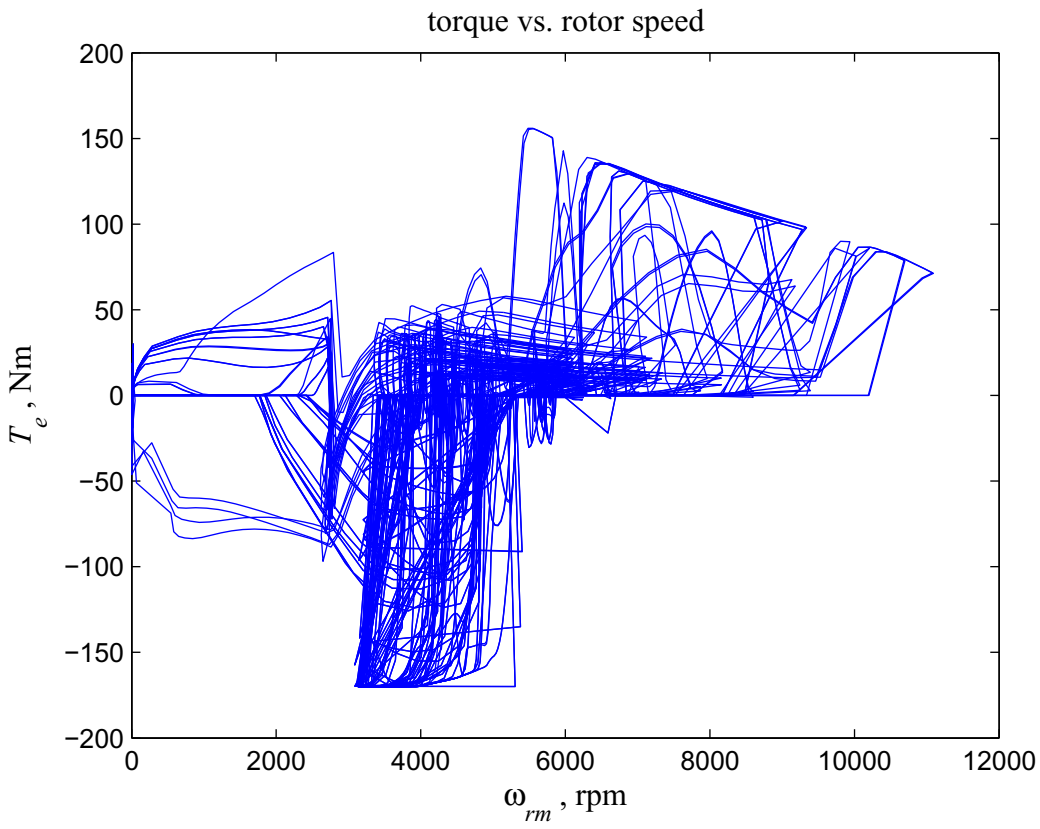

Fig. 6.4 Torque versus speed

To apply the machine design procedure described in Chapters 3 and 4, a finite number of torque and speed points that are representative of the overall torque and speed time trajectories need to be identified. The first step in the identification process is selecting points that are extrema in terms of their torque and speed magnitudes. Four of these points are selected by inspection, in addition to the 0 speed and torque point. These points are listed in Table 6.1.

TABLE 6.1
Pre-selected Operating Points

Operating point	Speed, rpm	Torque, Nm
1	0	0
2	5485	156
3	8066	114
4	11087	71.2
5	5307	-170

Point 1 was selected because the machine is essentially at rest during a significant portion of the drive cycle. Points 2, 4, and 5 were selected to make sure that the designed machine can operate at the maximum torque, maximum speed and minimum torque points seen in the time domain simulation. Point number 3 is an intermediate point between points 2 and 4.

Next, a single objective optimization problem is formulated to identify six additional operating points. The design space consists of the speed and torque points to be identified as given by vector $\boldsymbol{\theta}_o$

$$\boldsymbol{\theta}_o = [\omega_{rm,6} \ldots \omega_{rm,11} \ , \ T_{e,6} \ldots T_{e,11}] \tag{6.1}$$

The optimization's objective is to identify six additional speed and torque points so that the finite set of operating points best characterizes the infinite number of operating points which constitute the drive cycle trajectory. This requirement is mathematically described by

$$\boldsymbol{\theta}_o^* = \arg\min\left(\mathrm{e}\left(\boldsymbol{\theta}_o\right)\right) \tag{6.2}$$

where $\arg\min$ is a function that finds the points in $\boldsymbol{\theta}_o$ for which $\mathrm{e}\left(\boldsymbol{\theta}_o\right)$ attains its lowest value and where

$$\mathrm{e}\left(\boldsymbol{\theta}_o\right) = \int_0^T \min_{p \in \mathrm{P}} \left(\frac{\left|\omega_{rm}\left(t\right) - \omega_{rm,p}\right|}{\omega_{rm,b}} + \frac{\left|\mathrm{T}_e\left(t\right) - T_{e,p}\right|}{T_{e,b}} \right) dt \tag{6.3}$$

In (6.3), $\omega_{rm}\left(t\right)$ and $\mathrm{T}_e\left(t\right)$ denotes the rotor mechanical speed and torque at time t, $\omega_{rm,p}$ and $T_{e,p}$ denote the p^{th} speed and torque operating point to be identified out of a set of operating points $\mathrm{P} = [6, 7, .. 11]$, and $\omega_{rm,b}$ and $T_{e,b}$ are base quantities used to normalize (6.3). The base quantities are equal to the maximum absolute values of the speed and torque points from the time domain simulation. The error function is given as the integral of the minimum of speed and torque distances over P within one time cycle (total time elapsed in the given data in Figs 6.2 and 6.3. Since the optimization algorithm used (Genetic Algorithm, GA) maximizes its objective function, the fitness function is defined with the purpose of minimizing $\mathrm{e}\left(\boldsymbol{\theta}_o\right)$ as

$$f(\boldsymbol{\theta}_o) = \frac{1}{e(\boldsymbol{\theta}_o)} \tag{6.4}$$

The optimization was applied with a GA population and generation size both equal to 500. The resulting operating points from this optimization, in addition to the pre-selected points 2-5 in Table 6.1, are listed in Table 6.2.

Returning to the discussion on the reason for pre-selecting the [0,0] in Table 6.1, it was mainly included into the optimization in order to make sure that the optimization output points, points 6 through 11, do not contain any [0,0] torque-speed point, since there is no interest in modeling a [0,0] torque-speed when designing the electric machine. With the [0,0] torque-speed point omitted, a total of 10 points remain as seen in Table 6.2. These points are plotted in the in Fig. 6.5, along with the time domain torque versus speed trajectory.

To check if the identified points accurately represent the time series trajectories in Fig. 6.2 and 6.3, the torque and speed time trajectories are re-plotted using the 11 discrete points; 10 points in Table 6.2 and the [0,0] torque-speed point. These trajectories are shown in red in Figs 6.6 and 6.7 and are superimposed over the original torque and speed time trajectories. As can be seen, the points capture with an acceptable accuracy the original torque and speed time trajectories. Based on how frequent each point in Table 6.2 is repeated in Figs. 6.6 and 6.7, a weighting for each of the 11 points that sums to 1 is created. Next, the weight of each torque-speed point, except for the [0,0] point, is scaled down using the sum of the weighting of the 10 points, not including the [0,0] point. This gives the weighting that is shown in Table 6.2, and which sums to 1 (or 100 %).

TABLE 6.2
Hybrid Vehicle Design Operating Points

Point	Speed, rpm	Torque, Nm	Weight, (%)
1	3786	-169.1	17.6
2	4516	30.0	16.39
3	5750	8.51	15.93
4	4348	0.0005	11.07
5	1884	0.0012	9.98
6	5307	-170	9.88
7	4040	-67.1	8.48
8	8066	114	6.13
9	5485	156	3.99
10	11087	71.2	0.67

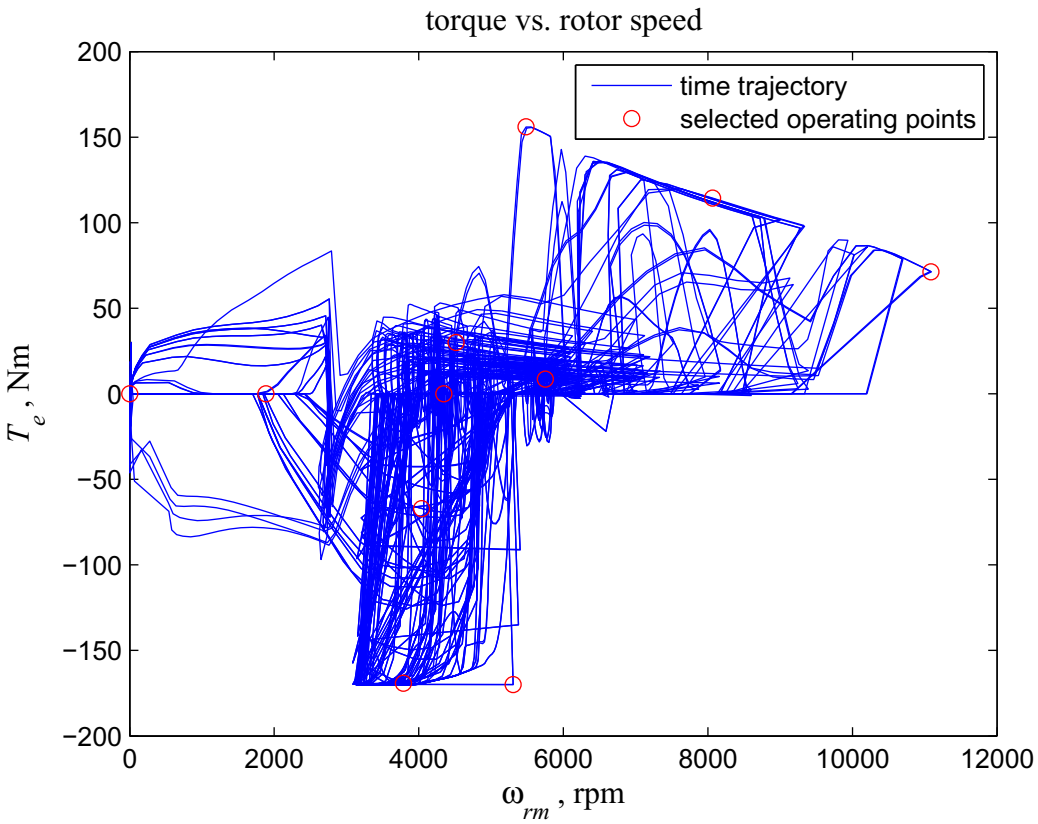

Fig. 6.5. Selected torque versus speed points

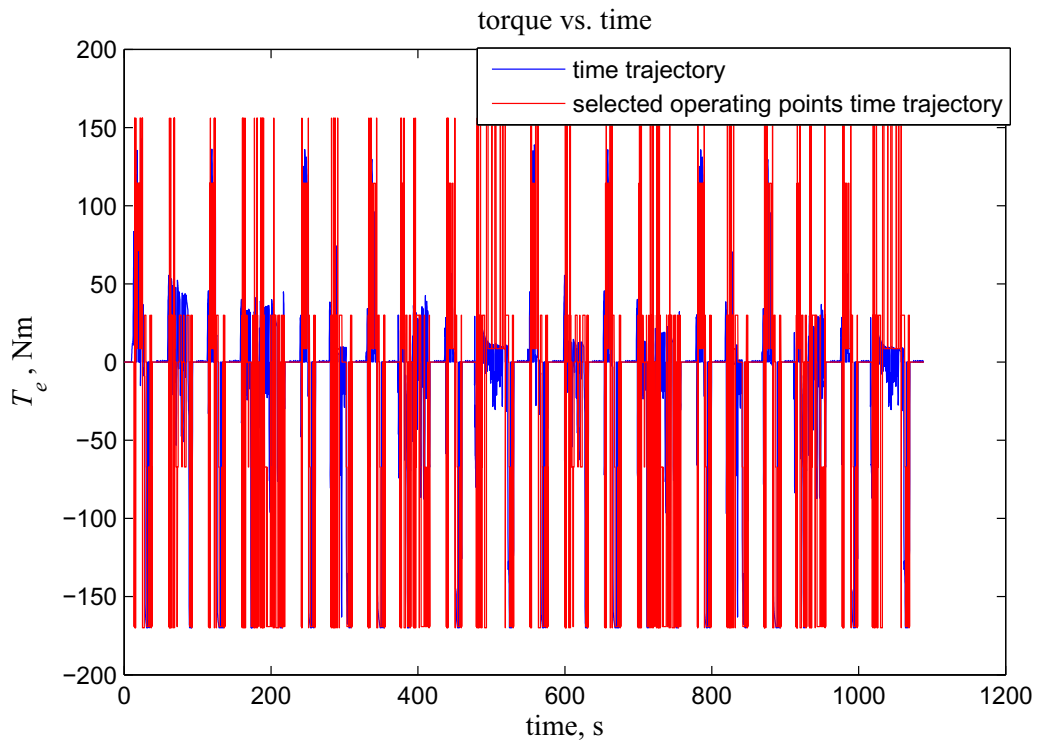

Fig. 6.6. Torque versus time trajectory

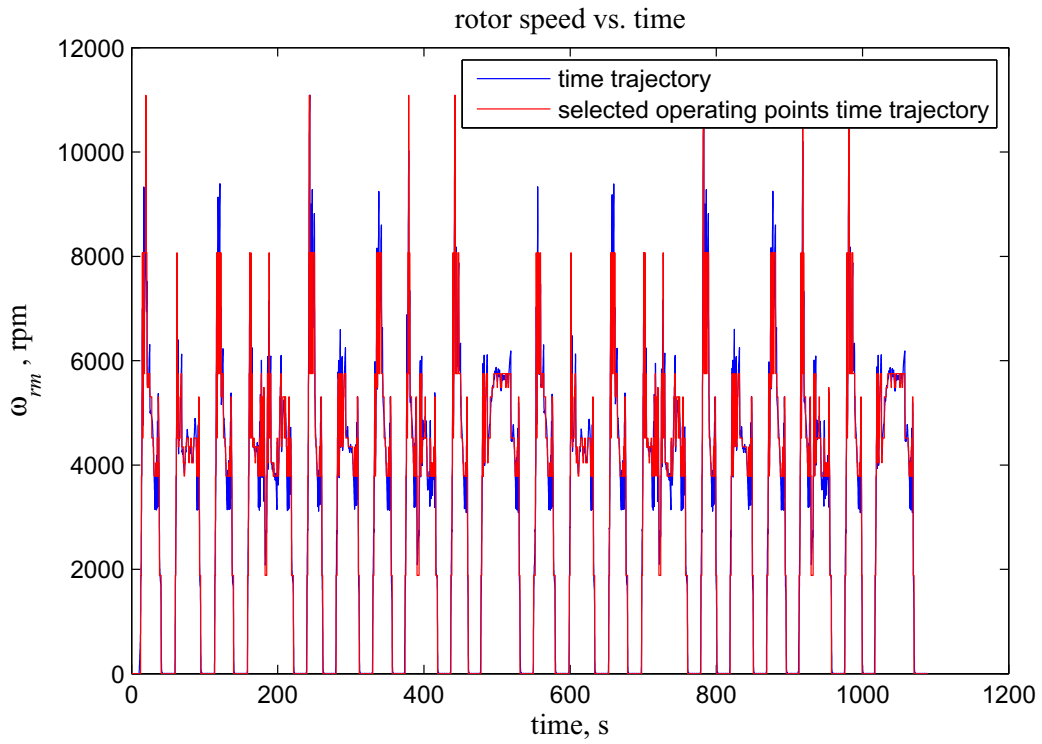

Fig. 6.7. Speed versus. time trajectory

6.3 Asymmetrical Design for a Generator

With a closer inspection into the design operating points in Table 6.2, it can be seen that the weighting is more favorable for points with negative torque instead of a positive torque. Thus, the machine is more often operated as a generator generator than a motor. Thus, to increase the chances of obtaining benefits from the asymmetrical structure, changes needs to be made to the structure AS-PMSM.

Considering that a negative torque flips the phase of the spatial MMF in the air gap of the machine, a method to favor generation is to position the rotor tooth on the opposite side of the magnet compared to the placement applied in Chapters 3 and 4 and shown in Figs 3.1 and 3.3. Note that the asymmetry applied in this work is not a rotational asymmetry; but an electromagnetic asymmetry that mainly depends on the spatial phase of the MMF waveform relative to the rotor.

6.4 Design Specifications, Design Space and Constraints

The design specifications, design space and design constraints for this case study are very similar to those discussed in Section 4.1 and 4.2. There are some changes however that were made.

With respect to the design specifications, instead of a 2 cm shaft radius r_{sh}, a 5 cm radius was set. Second the dc power supply voltage v_{dc} was reduced to 256 V. The maximum mass limit, M_{emmx}, was increased to 70 kg while instead of a maximum limit on loss, it was replaced with a maximum limit on cost of $400.

In order to avoid low conductor per slot count, the pole pairs of a winding were tied in parallel instead of a series connection. With this change, the *qd* voltages in (3.105) and (3.106) should be multiplied by $2/\mathrm{P}$. The *qd* current are in this case the currents flowing in one of the branches of the parallel winding. Therefore, the switch conduction loss (3.77) is adjusted by a multiplication factor of $P/2$.

With negative torque considered, constraint c_{16} in (4.20) is slightly changed to

$$c_{16} = \begin{cases} \mathrm{gtn}\left(T_{ec}, T_e^*\right) & T_e^* \geq 0 \\ \mathrm{ltn}\left(T_{ec}, T_e^*\right) & T_e^* < 0 \end{cases} \tag{6.5}$$

The equation used to calculate the corrected torque in (4.19) is still applicable for this case study. The design space is structured using the same design space parameters in (4.1) and (4.27). However, the upper and lower limit for most design parameters was changed. For the case of the AS-PMSM design space, the range for each parameter in this optimization is listed in Table 6.3. Note that ten pairs of *qd* currents are incorporated into the design space to account for each of the ten operating points. The range on these current was defined by considering the torque and speed magnitudes at each operating point in the order listed in Table 6.2.

Except for parameters α_{rt}, g_{rt}^{*}, and α_{tap}, the design space for the SM-PMSM is defined similarly. The design objectives and fitness function are defined similarly to what is presented in Section 4.2. The next section presents the results of the design optimization.

TABLE 6.3
Hybrid Vehicle Design AS-PMSM Design Parameters Range

Parameter	Min.	Max.	Encoding	Units	Parameter	Min.	Max.	Encoding	Units
s_t	1	1	Int	N/A	$i^r_{ds,1}$	-700	50	Lin	A
r_t	1	1	Int	N/A	$i^r_{qs,2}$	10^{-5}	300	Lin	A
c_t	1	1	Int	N/A	$i^r_{ds,2}$	-700	0	Lin	A
m_t	1	7	Int	N/A	$i^r_{qs,3}$	10^{-5}	300	Log	A
P_p	1	3	Int	N/A	$i^r_{ds,3}$	-700	0	Lin	A
d_i	0.1	20	Log	cm	$i^r_{qs,4}$	10^{-5}	50	Log	A
d_{rb}	0.1	4	Log	cm	$i^r_{ds,4}$	-50	0	Lin	A
d_m	0.1	4	Log	cm	$i^r_{qs,5}$	10^{-5}	50	Log	A
g	0.5	4	Log	mm	$i^r_{ds,5}$	-50	0	Lin	A
d_{tb}	0.1	4	Log	cm	$i^r_{qs,6}$	-700	0	Log	A
α_t	0.3	0.95	Lin	N/A	$i^r_{ds,6}$	-700	50	Lin	A
d_{sb}	0.1	5	Log	cm	$i^r_{qs,7}$	-700	0	Log	A
α_{pm}	0.4	0.95	Lin	N/A	$i^r_{ds,7}$	-700	50	Lin	A
l	1	20	Log	cm	$i^r_{qs,8}$	10^{-5}	700	Log	A
N^*_{s1}	10	1000	Log	cond./rad	$i^r_{ds,8}$	-700	50	Lin	A
α^*_3	0.1	0.7	Lin	N/A	$i^r_{qs,9}$	10^{-5}	700	Log	A
α_{rt}	0.1	1	Log	N/A	$i^r_{ds,9}$	-700	50	Lin	A
g^*_{rt}	0.5	20	Log	mm	$i^r_{qs,10}$	10^{-5}	700	Log	A
α_{tap}	1	1	Lin	N/A	$i^r_{ds,10}$	-700	50	Lin	A
$i^r_{qs,1}$	-700	0	Lin	A					

6.5 Optimization Results

The multi-objective optimization was initiated six times for the SM-PMSM and six times for the AS-PMSM. These GA population and generation size for each run is listed in Table 6.4. Runs 1-3 had population and generation size of 4000, while runs 4-6 had a population and generation equal to 5000.

TABLE 6.4
Hybrid Vehicle Design Convergence Studies

Run Number	GA Population	GA Generation
1	4000	4000
2	4000	4000
3	4000	4000
4	5000	5000
5	5000	5000
6	5000	5000

The Pareto-optimal front for each SM-PMSM and AS-PMSM run is shown in Figs. 6.8 and 6.9, respectively. As can be seen, full convergence was not obtained in these runs. This is attributed to the large design space which includes 39 degrees of freedom.

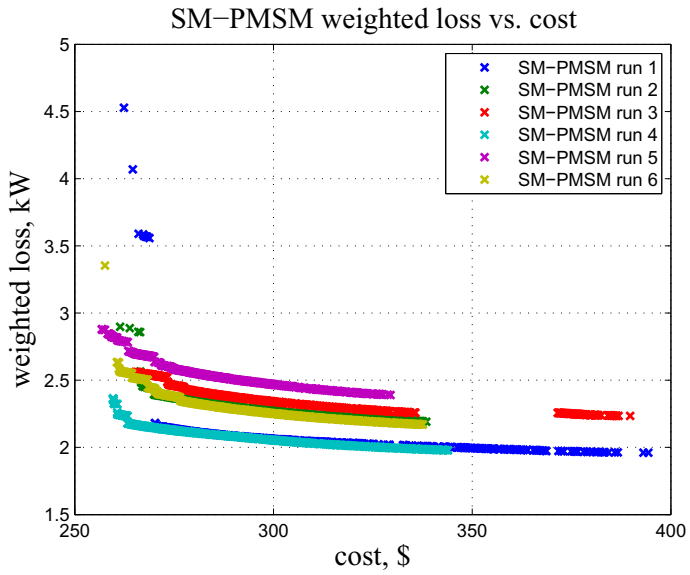

Fig. 6.8. Hybrid Vehicle Design SM-PMSM Pareto-optimal fronts

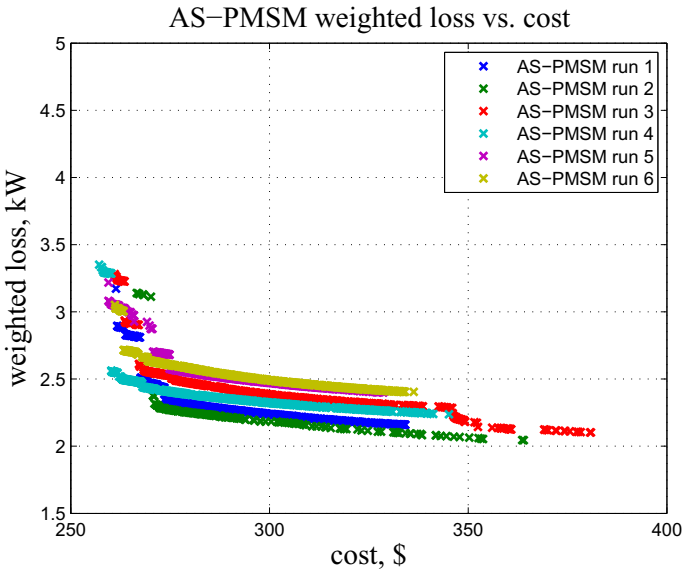

Fig. 6.9. Hybrid Vehicle Design AS-PMSM Pareto-optimal fronts

The best Pareto-optimal front from the SM-PMSM and AS-PMSM runs are compared together in Fig. 6.10. It is seen that the SM-PMSM slightly outperforms the AS-PMSM. It is believed that this is due to failure of convergence of the optimization; most AS-PMSM Pareto-optimal front designs in Fig. 6.10 are in fact symmetrical machines with no/negligible rotor tooth. The principle reason for this result is that the given requirements include positive and negative torque of almost the same magnitude. Thus, an asymmetrical design improves the performance for either motoring or generation mode, but this occurs at the expense of degrading the performance in the opposite mode. This as a result makes a symmetrical PMSM design ore favorable for the given design specifications.

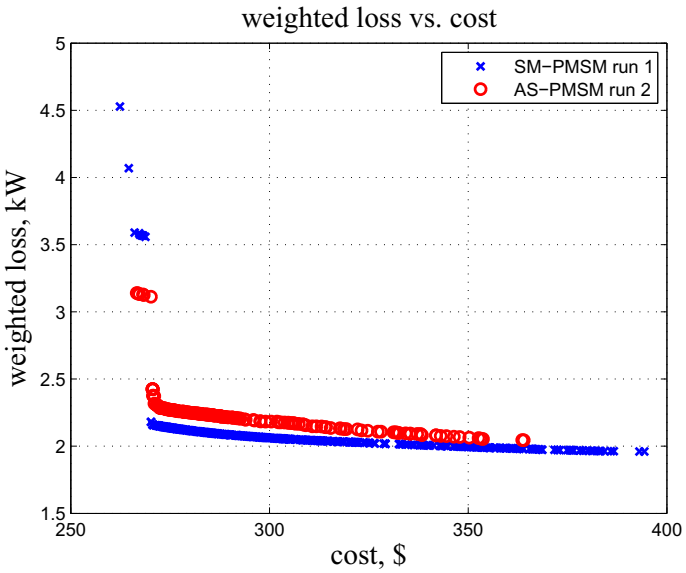

Fig. 6.10. Hybrid Vehicle Design SM-PMSM versus AS-PMSM Pareto-optimal front

The gene distribution plot from the AS-PMSM optimization, run 2, is shown in Figs 6.11. Gene number 5, which is the pole pair number, is chosen at its maximum limit of 3. Having a high pole pair number reduces the flux density magnitude in the rotor and stator steel, which is mainly advantageous to the peak flux density constraints. However, at the speeds considered, the required converter switching frequency becomes problematic, and therefore, to limit those losses, the maximum pole pair number was set to 3. The rotor tooth span and air gap parameters, genes 17 and 18 appear to have not converged to specific value. This can considered as an indication about the conclusion made previously that the asymmetrical machine for the given torque and speed trajectories is not favorable.

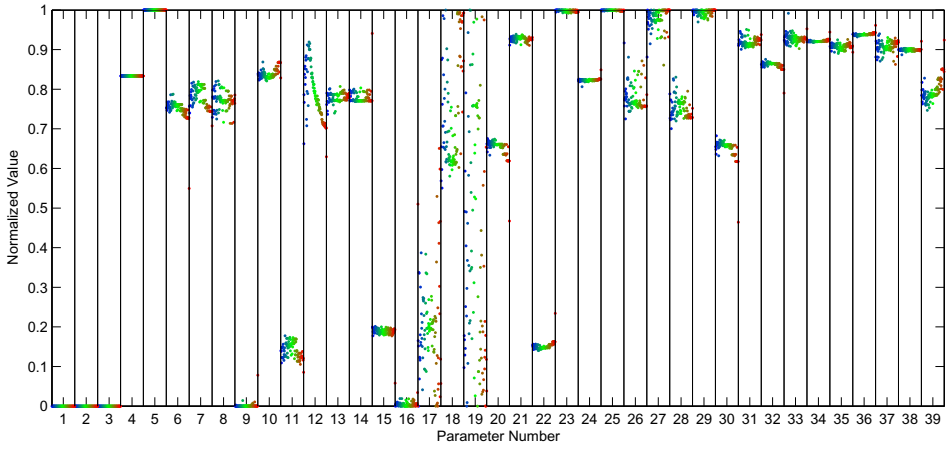

Fig. 6.11. Hybrid Vehicle Design AS-PMSM gene distribution plot

A machine from the AS-PMSM Pareto-optimal front was chosen for a closer inspection. The machine's properties are listed in Table 6.4. The cross section of the machine is shown in Figs. 6.12 and 6.13.

TABLE 6.4
Hybrid Vehicle Design AS-PMSM Pareto-optimal front design number 135

Outside Diameter	36 cm	Tooth Fraction	38.0 %
Total Length	19.5 cm	Tooth Base Width:	0.91 cm
Active Length	11 cm	Stator Backiron Depth	2.40 cm
Number of Poles	6	Rotor Backiron Depth	1.73 cm
Number of Slots	36	Fundamental Conductor Density	24.0 cond/rad
Stator Material Type	M19	3rd Harmonic Conductor Density	0.0 %
Rotor Material Type	M19	Conductor Diameter	5.4 mm
Conductor Type	Copper	Stator Iron Mass	26.2 kg
Permanent Magnet Type	Ferrite AC-12	Rotor Iron Mass	9.9 kg
Permanent Magnet Fraction	83.0 %	Conductor Mass	13.2 kg
Permanent Magnet Depth	1.52 cm	Magnet Mass	5.45 kg
Permanent Mag. Rem. Flux Density	0.4 T	Mass	55.0 kg
Permanent Mag. Susceptibility	0.1	Stator Iron Cost	$91.6
Rotor tooth maximum depth	0.11 cm	Rotor Iron Cost	$34.6
Rotor tooth minimum depth	0.11 cm	Conductor Cost	$148
Rotor tooth span fraction	15.0 %	Magnet Cost	$30.5
Rotor tooth tapering fraction	100 %	Total Cost	$305
Stator Tooth Radius	14.0 cm	Weighted Total Loss	2.2 kW
Shaft Radius	5.00 cm	A-Phase Winding Pattern (1st Pole)	[1 3 4 4 3 1]
Inert Radius	10.5 cm	Minimum Conductors Per Slot	8
Rotor Iron Radius	12.2 cm	Maximum Conductors Per Slot	8
Air Gap	0.5 mm	Packing Factor	50%
Slot Depth	2.18 cm		

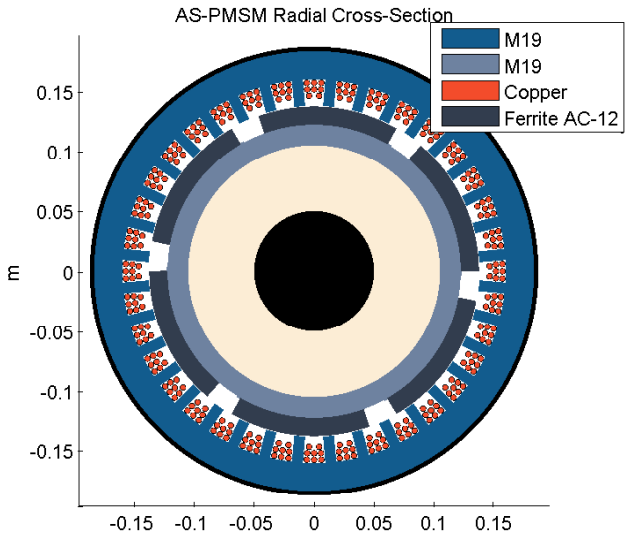

Fig. 6.12. Hybrid Vehicle Design vehicle AS-PMSM design number 135 cross section

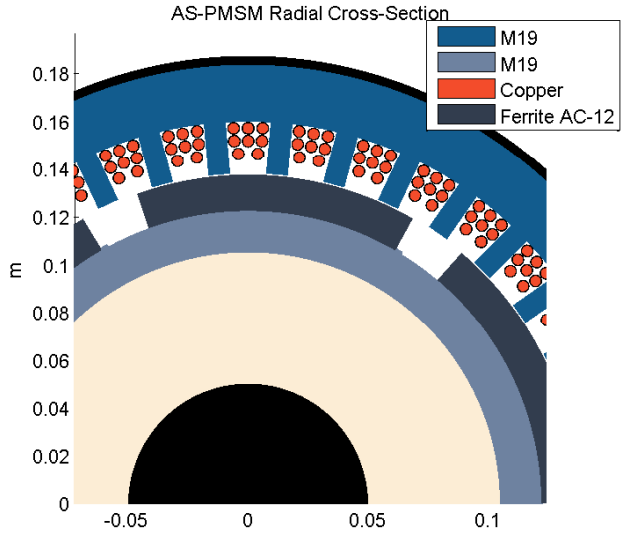

Fig. 6.13. Magnified section of design number 135

A number of characteristics that depend on the operating point are shown Table 6.5. The operating point order is as was listed in Table 6.2. The loss breakdown figure shows that the biggest loss components are switch and dc conduction losses. At high speeds and low torque, core loss dominates the machine loss. Considering the efficiency of the machine, at most operating points it is above 95%.

TABLE 6.5
Hybrid Vehicle Design AS-PMSM Pareto-optimal front design number 135 operating point characteristics

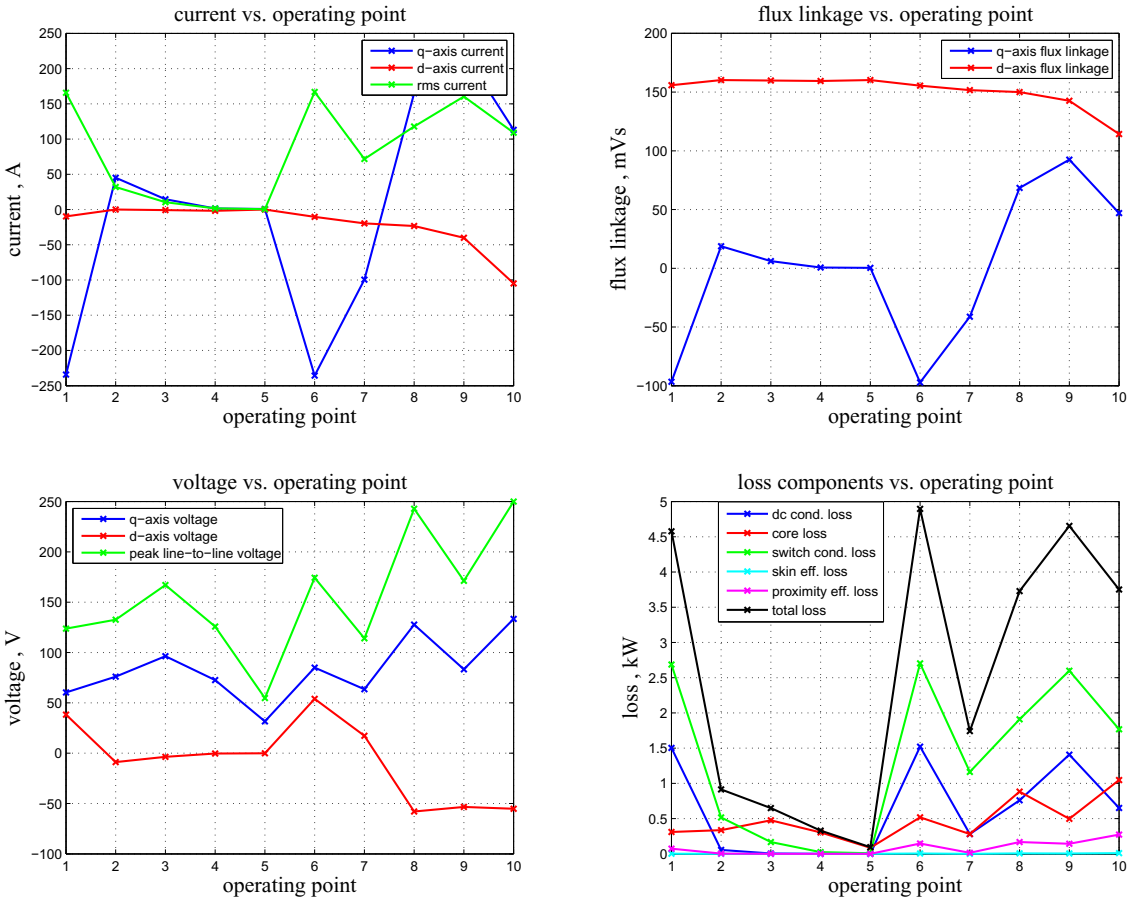

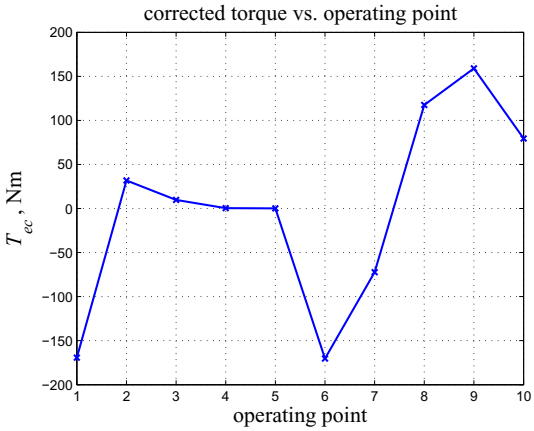
corrected torque vs. operating point
T_{ec}, Nm
operating point

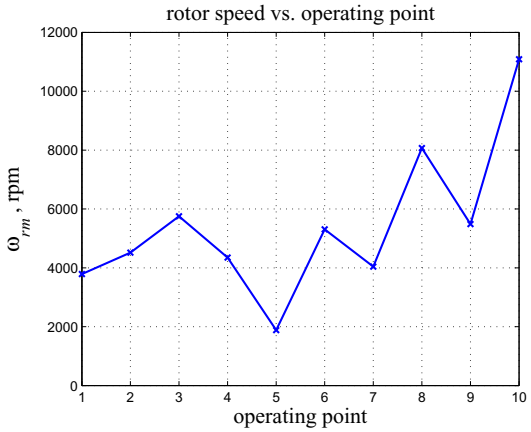
rotor speed vs. operating point
ω_{rm}, rpm
operating point

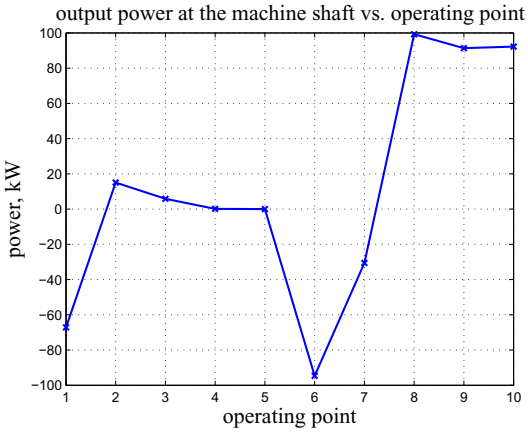
output power at the machine shaft vs. operating point
power, kW
operating point

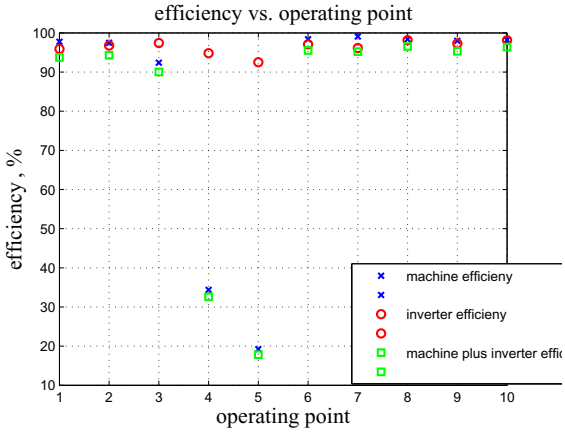
efficiency vs. operating point
efficiency, %
machine efficieny
inverter efficieny
machine plus inverter effi
operating point

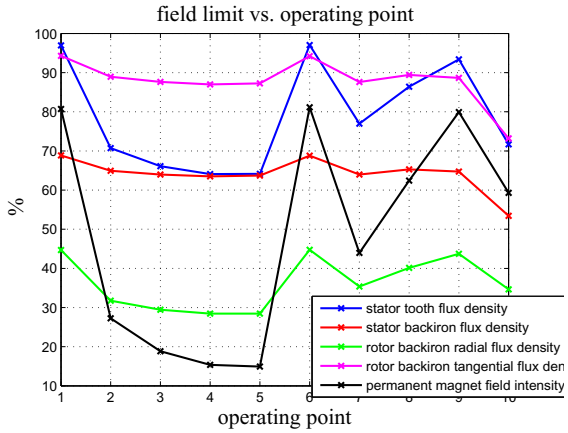
field limit vs. operating point
%
stator tooth flux density
stator backiron flux density
rotor backiron radial flux density
rotor backiron tangential flux den
permanent magnet field intensity
operating point

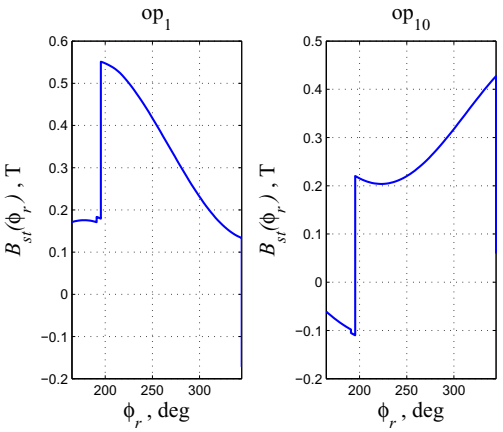
op1
op10
$B_{st}(\phi_r)$, T
ϕ_r, deg

7. CONCLUSION AND FUTURE WORK

The objective of the work in this thesis was to introduce a new permanent magnet synchronous machine structure that has an improved torque density performance compared to nominal surface mount permanent magnet machines and that can be used in wide Constant Power Speed Range (CPSR) applications. A detailed analysis of the machine was applied, followed by a multi-objective optimization design of the machine. Results obtained showed that the asymmetrical permanent magnet machine outperformed the symmetrical permanent magnet machine in cost and loss metrics in an asymmetric constant-power variable-speed application. The analytical design results were confirmed using 3-D Finite Element Analysis simulation. An acceptable agreement in results was obtained.

The proposed machine structure was designed for a parallel heavy hybrid electric vehicle. It was concluded that the AS-PMSM brings no benefits compared to a SM-PMSM in this application. The principle reason for this result is that the given application was not uni-directional; both motoring and generation by means of regenerative braking were considered, with comparable torque levels in both modes. As a result, a symmetrical turned out to be more favorable for this application.

Future work includes adding permanent magnet-rotor tooth leakage effect into the analytical model. This will improve the correlation between the analytical model and the 3D FEA results. Other areas recommended for the future work include the incorporation of thermal and mechanical analysis into the design. Finally, inclusion of the switching losses in the loss analysis should be pursued.

LIST OF REFERENCES

LIST OF REFERENCES

[1] El-Refaie, A.; Nold, R.; Haran, K.; Shah, M.; Weeber, K.; Huh, K.; Alexander, J.; Stephens, C.; Galioto, S., "Testing of advanced permanent magnet machines for a wide range of applications," *Electrical Machines (ICEM), 2012 XXth International Conference on* , vol., no., pp.1860,1867, 2-5 Sept. 2012

[2] Bazzi, A.M., "Electric machines and energy storage technologies in EVs and HEVs for over a century," *Electric Machines & Drives Conference (IEMDC), 2013 IEEE International* , vol., no., pp.212,219, 12-15 May 2013

[3] Chau, K.T.; Chan, C.C., "Emerging Energy-Efficient Technologies for Hybrid Electric Vehicles," *Proceedings of the IEEE* , vol.95, no.4, pp.821,835, April 2007

[4] Harianto, C.A.; Sudhoff, S.D., "A Rotationally Asymmetric Reluctance Machine With Improved Torque Density," *Energy Conversion, IEEE Transactions on* , vol.28, no.1, pp.62,75, March 2013

[5] Dongyun Lu; Kar, N.C., "A review of flux-weakening control in permanent magnet synchronous machines," *Vehicle Power and Propulsion Conference (VPPC), 2010 IEEE* , vol., no., pp.1,6, 1-3 Sept. 2010

[6] Pellegrino, G.; Armando, E.; Guglielmi, P., "Direct Flux Field-Oriented Control of IPM Drives With Variable DC Link in the Field-Weakening Region," *Industry Applications, IEEE Transactions on* , vol.45, no.5, pp.1619,1627, Sept.-oct. 2009

[7] Uddin, M.N.; Azizur Rahman, M., "High-Speed Control of IPMSM Drives Using Improved Fuzzy Logic Algorithms," *Industrial Electronics, IEEE Transactions on* , vol.54, no.1, pp.190,199, Feb. 2007

[8] Sudhoff, S.D.; Corzine, K. A.; Hegner, H.J., "A flux-weakening strategy for current-regulated surface-mounted permanent-magnet machine drives," *Energy Conversion, IEEE Transactions on* , vol.10, no.3, pp.431,437, Sep 1995

[9] Gi-Young Choi; Mu-Shin Kwak; Tae-Suk Kwon; Seung-Ki Sul, "Novel Flux-Weakening Control of an IPMSM for Quasi Six-Step Operation," *Industry Applications Conference, 2007. 42nd IAS Annual Meeting. Conference Record of the 2007 IEEE* , vol., no., pp.1315,1321, 23-27 Sept. 2007

[10] Bon-Ho Bae; Patel, N.; Schulz, S.; Seung-Ki Sul, "New field weakening technique for high saliency interior permanent magnet motor," *Industry Applications Conference, 2003. 38th IAS Annual Meeting. Conference Record of the* , vol.2, no., pp.898,905 vol.2, 12-16 Oct. 2003

[11] Jiunn-Jiang Chen; Kan-Ping Chin, "Minimum copper loss flux-weakening control of surface mounted permanent magnet synchronous motors," *Power Electronics, IEEE Transactions on* , vol.18, no.4, pp.929,936, July 2003

[12] Gallegos-Lopez, G.; Gunawan, F.S.; Walters, J.E., "Optimum torque control of permanent-magnet AC Machines in the field-weakened region," *Industry Applications, IEEE Transactions on* , vol.41, no.4, pp.1020,1028, July-Aug. 2005

[13] Azizur Rahman, M.; Vilathgamuwa, D.M.; Uddin, M.N.; King-Jet Tseng, "Nonlinear control of interior permanent-magnet synchronous motor," *Industry Applications, IEEE Transactions on* , vol.39, no.2, pp.408,416, Mar/Apr 2003

[14] Shi, J.-L.; Liu, T. -H; Yang, S.-H., "Nonlinear-controller design for an interior-permanent-magnet synchronous motor including field-weakening operation," *Electric Power Applications, IET* , vol.1, no.1, pp.119,126, January 2007

[15] Schiferl, R.F.; Lipo, T.A., "Power capability of salient pole permanent magnet synchronous motors in variable speed drive applications," *Industry Applications, IEEE Transactions on* , vol.26, no.1, pp.115,123, Jan/Feb 1990

[16] Longya Xu; Ye, L.; Li Zhen; El-Antably, A., "A new design concept of permanent magnet machine for flux weakening operation," *Industry Applications, IEEE Transactions on* , vol.31, no.2, pp.373,378, Mar/Apr 1995

[17] Kamiya, M., "Development Of Traction Drive Motors For The Toyota Hybrid System," *IEEJ Transactions on Industry Applications*, 2006

[18] Barcaro, M.; Bianchi, N.; Magnussen, F., "Permanent-Magnet Optimization in Permanent-Magnet-Assisted Synchronous Reluctance Motor for a Wide Constant-Power Speed Range," *Industrial Electronics, IEEE Transactions on* , vol.59, no.6, pp.2495,2502, June 2012

[19] Krizan, J. “Population Based Design of Permanent Magnet Synchronous Machine Drive Systems” PhD Thesis, Purdue University, West Lafayette, IN, May 2012

[20] Chau, K.T.; Wei Cui; Jiang, J.Z.; Zheng Wang, "Design of permanent magnet brushless motors with asymmetric air gap for electric vehicles," *Journal of Applied Physics* , vol.99, no.8, pp.08R322,08R322-3, Apr 2006

[21] Iepure, L.I.; Tutelea, L.; Boldea, I., "FEM analysis and control of a tapered airgap single phase PMSM," *Optimization of Electrical and Electronic Equipment, 2008. OPTIM 2008. 11th International Conference on* , vol., no., pp.241,248, 22-24 May 2008

[22] Vollmer, U.; Schafer, U.; "At An All Operating Points Highly Efficient PMSM For HEV" *The World Electric Vehicle Journal* , vol. 2, issue 4, 2008

[23] EL-Refaie, A.M.; Jahns, T.M., "Optimal flux weakening in surface PM machines using fractional-slot concentrated windings," *Industry Applications, IEEE Transactions on* , vol.41, no.3, pp.790,800, May-June 2005

[24] EL-Refaie, A.M.; Jahns, T.M.; McCleer, P.J.; McKeever, J.W., "Experimental verification of optimal flux weakening in surface PM Machines using concentrated windings," *Industry Applications, IEEE Transactions on* , vol.42, no.2, pp.443,453, March-April 2006

[25] Jannot, X.; Vannier, J. -C; Marchand, C.; Gabsi, M.; Saint-Michel, J.; Sadarnac, D., "Multiphysic Modeling of a High-Speed Interior Permanent-Magnet Synchronous Machine for a Multiobjective Optimal Design," *Energy Conversion, IEEE Transactions on* , vol.26, no.2, pp.457,467, June 2011

[26] Cassimere, B.N.; Sudhoff, S.D., "Population-Based Design of Surface-Mounted Permanent-Magnet Synchronous Machines," *Energy Conversion, IEEE Transactions on* , vol.24, no.2, pp.338,346, June 2009

[27] Sonoda, S.; Takahashi, Y.; Kawagishi, K.; Nishida, N.; Wakao, S., "Application of Stepwise Multiple Regression to Design Optimization of Electric Machine," *Magnetics, IEEE Transactions on* , vol.43, no.4, pp.1609,1612, April 2007

[28]Sudhoff, S. “Power Magnetic Devices: A Multi-Objective Design Approach,” Wiley-IEEE Press, February 2014

[29]Yao Duan; Ionel, D.M., "A Review of Recent Developments in Electrical Machine Design Optimization Methods With a Permanent-Magnet Synchronous Motor Benchmark Study," *Industry Applications, IEEE Transactions on* , vol.49, no.3, pp.1268,1275, May-June 2013

[30] Reddy, P.B.; EL-Refaie, A.M.; Kum-Kang Huh; Tangudu, J.K.; Jahns, T.M., "Comparison of Interior and Surface PM Machines Equipped With Fractional-Slot Concentrated Windings for Hybrid Traction Applications," *Energy Conversion, IEEE Transactions on* , vol.27, no.3, pp.593,602, Sept. 2012

[31] *"Genetic Optimization System Engineering Tool (GOSET) for Use With MATLAB"* ver. 2.4, School of Electrical and Computer Engineering, Purdue University, West Lafayette, IN, with United States Naval Academy, Annapolis, MD, 2005 [Online]. Available: https://engineering.purdue.edu/ECE/Research/Areas/PEDS/go_system_engineering_toolbox

[32] EL-Refaie, A.M., "Fractional-Slot Concentrated-Windings Synchronous Permanent Magnet Machines: Opportunities and Challenges," *Industrial Electronics, IEEE Transactions on* , vol.57, no.1, pp.107,121, Jan. 2010

[33] Reinert, J.; Brockmeyer, A.; De Doncker, R.W.A.A.; , "Calculation of losses in ferro- and ferrimagnetic materials based on the modified Steinmetz equation", *IEEE Transactions on Industry Applications*, vol.37, no.4, pp.1055-1061, Jul/Aug 2001

[34] Morimoto, S.; Kawamoto, K.; Sanada, M.; Takeda, Y., "Sensorless control strategy for salient-pole PMSM based on extended EMF in rotating reference frame," *Industry Applications, IEEE Transactions on* , vol.38, no.4, pp.1054,1061, Jul/Aug 2002

[35] Shane, G.M.; Sudhoff, S.D., "Refinements in Anhysteretic Characterization and Permeability Modeling," *Magnetics, IEEE Transactions on* , vol.46, no.11, pp.3834,3843, Nov. 2010

[36] Alsawalhi, J.Y.; Sudhoff, S.D., "Saturable Thermally-Representative Steinmetz-Based Loss Models," *Magnetics, IEEE Transactions on* , vol.49, no.11, pp.5438,5445, Nov. 2013

[37] Laldin, O.; Sudhoff, S.D.; Pekarek, S.D., "An Analytical Design Model for Hybrid Salient-Pole Machines," *Electric Machines & Drives Conference (IEMDC), 2013 IEEE International* , vol., no., pp.686,693, 12-15 May 2013

[38] *"Thermal Equivalent Circuit Toolbox"* ver. 2.0, School of Electrical and Computer Engineering, Purdue University, West Lafayette, IN Available: https://engineering.purdue.edu/ECE/Research/Areas/PEDS/go_system_engineering_toolbox

[39] Winzer, P.; Doppelbauer, M., "Theoretical Analysis of Synchronous Machines with Displaced Reluctance Axis" *International Conference on Electrical Machines (ICEM),* May 2014

[40] Benecki, W. "A Producer's and Buyer's Perspective: The Permanent Magnet Outlook" *Magnetics 2008 Conference*, 15-16 May 2008

APPENDICES

A. STEEL MATERIAL PROPERTIES

Table A.1
Steel Material Properties

Parameter number	Steel type	ρ, (kg/m^3)	c, (\$/kg)	$B_{lim,1}$, (T)	$B_{lim,2}$, (T)
1	M19	7402	3.5	1.39	1.44
2	M36	7018	3.5	1.34	1.37
3	M43	7291	3.5	1.39	1.50
4	M47	7585	3.5	1.49	1.67

B. PERMANENT MAGNET MATERIAL PROPERTIES

Table B.1
Permanent Magnet Material Properties

Parameter number	Permanent magnet type	ρ, (kg/m^3)	c, ($/kg)	B_r, (T)	χ_m	H_{ci}, (kA/m)
1	NdFeB N35	7500	130.57	1.19	0.09	-867
2	NdFeB N50	7500	130.57	1.43	0.36	-836
3	NdFeB Plastic	5700	130.57	0.66	0.24	-577
4	SmCo R20	8400	126.5	0.9	0.02	-2400
5	SmCo R32	8300	126.5	1.15	0.1	-1350
6	Ferrite AC-12	4900	5.59	0.4	0.1	-318
7	AlNiCo 8H	7250	44	0.74	1.5	-151

C. CONDUCTOR MATERIAL PROPERTIES

Table C.1
Conductor Material Properties

Parameter number	Conductor type	ρ, (kg/m^3)	c, (\$/kg)	σ_c, (S/m)	J_{lim}, (A/m^2)
1	Copper	8890	11.2	5.96×10^7	7.6×10^6
2	Aluminum	2705	11.54	3.77×10^7	6.6×10^6

D. MODIFIED STEINMETZ EQUATION PARAMETERS

Table D.1
Modified Steinmetz Equation Loss Density Parameters

Steel type	α	β	k_h, (J/m^3)	k_e, (Js/m^3)
M19	1.34	1.82	50.69	0.027
M36	1.34	1.80	64.1	0.04
M43	1.28	1.75	85.0	0.04
M47	1.25	1.68	149.0	0.26

VITA

VITA

Jamal Alsawalhi received the B.S., M.S. and PhD degrees in electrical engineering from Purdue University in 2009, 2011, and 2014, respectively. His research interests include design and analysis of electric machines and drives, magnetic material characterization and evolutionary optimization computing.